INVESTIGATIONS ON DIELECTRIC RESONATOR ANTENNAS FOR ULTRA-WIDE BAND APPLICATIONS

A Thesis

Submitted in fulfilment of the requirement for the award of the degree

of

DOCTOR OF PHILOSOPHY

in

Electronics and Communication Engineering

Submitted by

Sachin Kumar Yadav

Reg. No. 901606031

Under the Supervision of

Dr. Amanpreet Kaur
Assistant Professor
TIET, Patiala (Punjab), India

Dr. Rajesh Khanna
Professor
TIET, Patiala (Punjab), India

THAPAR INSTITUTE
OF ENGINEERING & TECHNOLOGY
(Deemed to be University)

Electronics and Communication Engineering Department

Thapar Institute of Engineering and Technology, Patiala-147004

February 2022

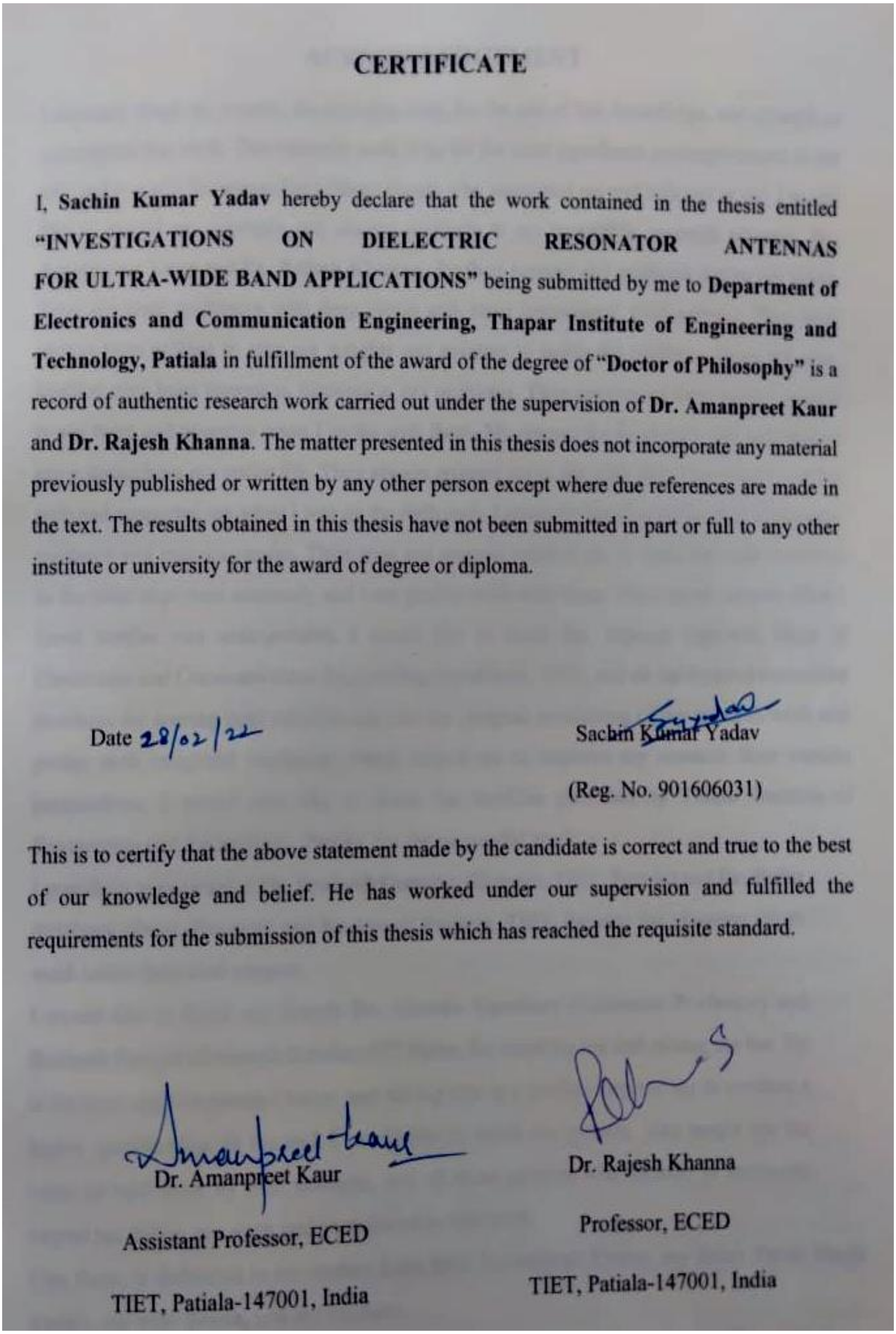

CERTIFICATE

I, **Sachin Kumar Yadav** hereby declare that the work contained in the thesis entitled **"INVESTIGATIONS ON DIELECTRIC RESONATOR ANTENNAS FOR ULTRA-WIDE BAND APPLICATIONS"** being submitted by me to **Department of Electronics and Communication Engineering, Thapar Institute of Engineering and Technology, Patiala** in fulfillment of the award of the degree of **"Doctor of Philosophy"** is a record of authentic research work carried out under the supervision of **Dr. Amanpreet Kaur** and **Dr. Rajesh Khanna**. The matter presented in this thesis does not incorporate any material previously published or written by any other person except where due references are made in the text. The results obtained in this thesis have not been submitted in part or full to any other institute or university for the award of degree or diploma.

Date 28/02/22

Sachin Kumar Yadav

(Reg. No. 901606031)

This is to certify that the above statement made by the candidate is correct and true to the best of our knowledge and belief. He has worked under our supervision and fulfilled the requirements for the submission of this thesis which has reached the requisite standard.

Dr. Amanpreet Kaur
Assistant Professor, ECED
TIET, Patiala-147001, India

Dr. Rajesh Khanna
Professor, ECED
TIET, Patiala-147001, India

ACKNOWLEDGEMENT

I sincerely thank my creator, the almighty God, for the gift of life, knowledge, and strength to accomplish this work. This research work is by far the most significant accomplishment in my life, and it would be impossible without people who supported me and believed in me. I would like to extend my gratitude and sincere gratitude to my honorable, research advisors, **Dr. Amanpreet Kaur** and **Dr. Rajesh Khanna**, for their support and guidance during my study. They are great professors with deep vision and, most importantly, kind persons. They have always been willing to give me insights and pointers to tackle the problems along the way, keeping very keen interest in listening to my problems. They are always there when I needed to see them and attentive when I spoke with them. My respect for them grew and will always grow throughout my entire life. They always pointed me in the right direction when I lost the path and supported me when I was on the right path. I sincerely thank them for their exemplary guidance and encouragement. Their trust and support inspired me to make the right decisions in the most important moments, and I am glad to work with them. Their moral support when I faced hurdles was unforgettable. I would like to thank **Dr. Alpana Agarwal**, Head of Electronics and Communication Engineering department, TIET, and all the doctoral committee members for sparing their valuable time for the progress monitoring of my research work and giving such insightful comments which helped me to improve my research from various perspectives. I would also like to thank the facilities provided by Thapar Institute of Engineering and Technology, Patiala, for the successful work.

I gratefully acknowledge **Dr. Prakash Gopalan** (Director, TIET, Patiala) and **Dr. Rafat Siddique** (Dean, Research and Sponsored Projects, TIET, Patiala) for allowing me to work under their kind support.

I would like to thank my friends **Dr. Gaurav Varshney (Assistant Professor)** and **Ratnesh Ranjan** (Research Scholar) NIT Patna, for inspiring me and raising the bar. He is the most capable person I know, and having him as a brother inspired me to conduct a higher qualification. In the end, I would like to thank my parents, who taught me the value of hard work by their example, and all those persons who directly or indirectly helped me during my work and contributed to this work.

This thesis is dedicated to my mother **Late Smt. Gyanshree Yadav**, my father **Fateh Singh Yadav**, my wife **Beena,** and my brothers.

Sachin Kumar Yadav

TIET, Patiala (Punjab), India

ABSTRACT

As the recent trending wireless systems are trending upward, UWB technology heralds a new age for wireless communication systems. It has a high data rate while consuming low power. Communication is becoming a part of the everyday living of individuals. As such, to accomplish efficient and proper wireless communication, compact and effective radiators are required. Undoubtedly, one of the effective radiators is a dielectric resonator antenna (DRA). The DRA is economical and has attractive highlights such as simple planning, basic construction strategies, and adaptability in the structure to meet the required frequencies. DRAs are superior and preferred replacements with printed antennas and microstrip patch antennas due to their high radiation efficiency, high data transfer capability, and adaptability of polarization.

This thesis recommends wide bandwidth and wide axial ratio bandwidth in a rectangular DRA (RDRA). With miniaturized DRA, some techniques such as air-spaced within dielectric resonator structure, perturbation theory, defective ground structure, stacking, segmenting, and merging modes of bandwidth improvement achieve the ultra-wideband operations. It also includes UWB DRA with multiple-input multiple-output (MIMO) configuration.

In objective 2, an air-spaced DRA is designed, simulated, and fabricated for UWB operations. This antenna consists of a rectangular dielectric resonator, microstrip feedline, and modified ground plane. A cylindrical-shaped structure is extracted from a solid rectangular DR to improve the antenna's gain and impedance bandwidth. The present work demonstrates gain enhancement by increasing the diameter of the air-gap within the solid structure of the RDR. A defective ground structure (DGS) is used to improve the antenna's impedance bandwidth in order to achieve UWB operation. The proposed antenna has a 104.09% impedance bandwidth (3.28 to 10.4 GHz) with a peak gain of 7.2 dB at 7.8 GHz.

OM-shaped DRA and Stacked Asymmetric DRA are two designs presented by Objective 3. First design, dielectric resonator (DR) modified to an ‘OM’ shape for UWB (3.1 to 11.3GHz) operations to support high data rate multimedia applications for 4G/5G communications. It has overall antenna dimensions of 50 × 40 × 4.87 mm^3. DRA is excited by a P-type transformer fed that offers an input impedance of 50 Ω. A conformal strip is attached between the feedline and the OM-shaped DR to improve DRA impedance matching. This ‘OM’ shaped DR structure excites the TE_{111} mode at 4.9 GHz, and two higher-order modes as TE_{211}, and TE_{221}, at 7.2 and 8.35 GHz, respectively. The proposed DRA has an impedance bandwidth of 8.2 GHz from 3.1

to 11.3 GHz with a peak gain of 7.68 dB at 10.5 GHz. the proposed DRA exhibits an elliptically polarized behavior with axial ratio bandwidth of 5.1GHz (≤ 10dB) from 6 to 11.1 GHz. A compact circularly polarised asymmetric-stacked DRA for UWB operations is developed in the second design, which is excited by a transformer-type feedline. The proposed DRA consists of two rectangular ceramic blocks with the same permittivity (ε_{DR} = 9.8) but differing in height and width of DR, and an F-shaped metal strip added to the partial ground, which achieves the widen axial ratio bandwidth. The proposed antenna is supported fundamental and third-order modes as $TE_{\delta 11}$ and $TE_{\delta 13}$ at 9.1 and 11.28 GHz, respectively. The proposed antenna covers 6.4 to 12.4 GHz (impedance bandwidth of 63.8 %) with a peak gain of 6.01 dBi at 11.5 GHz and AR bandwidth (≤ 3 dB) is reported 63.8% (6.4 to 12.4 GHz.

Objective 4 has proposed two MIMO DRA designs as rack-shaped DRA and cross-strip based DRA. In the first design, a rack-shaped two radiator element MIMO DRA is proposed for ultra-wideband applications. Two rectangular-shaped radiator elements are used to implement the proposed MIMO antenna structure, which are further transformed into rack-shaped dielectric resonators (DRs). An inverted T-shaped metallic strip is placed between two radiators to achieve the impedance bandwidth of 101.87 % (3.54 to 10.89 GHz) with isolation of 15.6 dB. Second design has better impedance bandwidth and isolation as compare to design 1. The cross-metallic strip based RDRA consists of two RDR, Inverted T- shaped metallic strip, scissor-shaped defected ground structure, cross-shaped metallic parasitic strips, and ground stub. Which provides an impedance bandwidth of 104.6 %, covering frequency from 3.3 to 10.8 GHz with isolation of 20 dB. The MIMO diversity parameters are implemented within the limit in both proposed design.

LIST OF PUBLICATIONS

P1. S. K. Yadav, A. Kaur, and R. Khanna, "Cylindrical air spaced high gain dielectric resonator antenna for ultra-wideband applications," *Sādhanā – Academy Proceedings in Engineering Sciences*, 2020. (IF: 1.214) DOI: https://doi.org/10.1007/s12046-020-01409-y

P2. S. K. Yadav, A. Kaur, and R. Khanna, "An Ultra-Wideband 'OM' Shaped DRA with a Defected Ground Structure and Dual Polarization Properties for 4G / 5G Wireless Communications." *The International Journal of* RF and Microwave Computer-Aided Engineering, 2020. (IF: 1.97) DOI: https://doi.org/10.1002/mmce.22327

P3. S. K. Yadav, A. Kaur, and R. Khanna, "Compact Rack Shaped MIMO Dielectric Resonator Antenna with improved Axial Ratio for UWB Applications" *Wireless personal communication journal*,2020. (IF: 2.017) DOI: https://doi.org/10.1007/s11277-020-07887-x

P4. S. K. Yadav, A. Kaur, and R. Khanna, "Compact cross-shaped parasitic strip based MIMO Dielectric Resonator Antenna for UWB Applications" *Frequenz,* 2021. (IF: 0.74) DOI: https://doi.org/10.1515/freq-2020-0027

P5. S. K. Yadav, A. Kaur, and R. Khanna, "Broadband circularly polarized dielectric resonator antenna for UWB applications," *Sādhanā – Academy Proceedings in Engineering Sciences*, 2022. (IF: 1.214)

P6. S. K. Yadav, A. Kaur, and R. Khanna, "A Comprehensive Survey of Ultra-Wideband Dielectric Resonator Antenna" *Microwave Journal*, 2022. (IF: 0.34)

OTHER PUBLICATIONS

1. S. K. Yadav, A. Kaur, and R. Khanna, "A Stacked Hollow Low-Profile Dielectric Resonator Antenna with Wide Bandwidth and Enhanced Gain." Proceedings of *International Conference on Applications of Computing, Automation and Wireless Systems (*MARC 2018), Delhi, India, *in Electrical Engineering, Springer,* Singapore, 2019, 1047-1054. DOI: https://doi.org/10.1007/978-981-13-6772-4_91

2. S. K. Yadav, A. Kaur, and R. Khanna, "Aperture coupled rectangular dielectric resonator antenna for multi band applications." In Proceedings of *International Conference on Innovations in Cyber-Physical Systems (ICICPS 2020),* Delhi, India, 22-23 OCTOBER, 2020, *Lecture Notes in Electrical Engineering, Springer,* Singapore. DOI: https://doi.org/10.1007/978-981-16-4149-7_73

3. S. K. Yadav, A. Kaur, and R. Khanna, "Compact circularly polarized asymmetrical shaped

DRA for UWB applications" In Proceedings of the *International Conference on Recent Trends in Communication and Electronics (ICCE-2020)*, Ghaziabad, India, 28-29 November 2020 (1st ed.). *CRC Press,* 440-443. DOI: https://doi.org/10.1201/9781003193838

4. S. K. Yadav, A. Kaur, and R. Khanna, "High gain MIMO Dielectric Resonator Antenna for UWB Applications" In Proceedings of the International Conference on Recent Trends in Communication and Electronics (ICCE-2020), Ghaziabad, India, 28-29 November 2020 (1st ed.). *CRC Press,* 444-447. DOI: https://doi.org/10.1201/9781003193838

LIST OF ABBREVIATIONS

1D	One Dimensional
2D	Two Dimensional
3D	Three Dimensional
1G	First-Generation
2G	Second-Generation
PCS	Personal Communication System
LAN	Local Area Network
3G	Third-Generation
WAN	Wide Area Network
4G	Fourth-Generation
IP	Internet Protocol
LTE	Long Term Evolution
GSM	Global System for Mobile Communications
UMTS	Universal Mobile Telecommunications System
CDMA	Code Divison Multiple Access
5G	Fifth-Generation
wwww	World Wide Wireless Web
IoT	Internet of Things
AMPS	Advanced Mobile Phone System
NMT	Nordic Mobile Telephone
TACS	Total Access Communication System
FDMA	Frequency Division Multiple Access
PSTN	Public Switched Telephone Network
TDMA	Time Division Multiple Access
WCDMA	Wideband Code Division Multiple Access
FCC	Federal Communications Commission
ITU-R	International Telecommunication Union-Radio
RADAR	Radio Detection and Ranging
MPA	Microstrip Patch Antennas
DR	Dielectric Resonator
DRA	Dielectric Resonator Antenna

DRAs	Dielectric Resonator Antennas
RDRA	Rectangular Dielectric Resonator Antenna
CDRA	Cylindrical Dielectric Resonator Antenna
MIC	Microwave Integrated Circuit
LCR	Inductor-Capacitor-Resistor
HE	Hybrid Electric
HEM	Hybrid Electric Magnetic
TE	Transverse Electric
TEM	Transverse Electromagnetic
TM	Transverse Magnetic
UWB	Ultra-Wide Band
VNA	Vector Network Analyzer
WiMAX	Worldwide Interoperability for Microwave Access
WLAN	Wireless Local Area Network
AP	Access Point
ECC	Envelope Correletion Coefficient
CCL	Channel Capacity Loss
EP	Elliptical Polarization
CP	Circular Polarization
CPW	Coplanar Waveguide
CSRR	Complementary Split Ring Resonator
CST MWS	Computer Simulation Technology Microwave Studio
DG	Diversity Gain
DGS	Defected Ground Structure
ECC	Envelope Correlation Coefficient
EM	Electromagnetic
FSS	Frequency Selective Surface
IEEE	Institute of Electrical and Electronics Engineering
IoT	Internet of Things
LHCP	Left Hand Circular Polarization
PAN	Personal Area Network
QM	Quasi-Mode

Q	Quality Factor
QWT	Quarter Wave Transformer
PCB	Printed Circuit Board
RHCP	Right Hand Circular Polarization
dB	decibel
OFDM	Orthogonal Frequency-Division multiplexing
DAA	Detect and Avoid
MICs	Ministry of Internal Affairs & Communications
IDA	Infocomm Development Authority
ETRI	Electronics and Telecommunications Research Institute
ECC	Electronic Communications Committee
SRP	Spherical Ring Patch
DRR	Dielectric Ring Resonator
CoDRR	Conical Dielectric Ring Resonator
SCRDRA	Stacked Conical Ring DRA
CSRDRA	Cylindrical Stepped Ring DRA
NB	Narrowband
HDRA	Hybrid DRA
VSWR	Voltage Standing Wave Ratio
MSMDRA	Mushroom-shaped Monopole DRA
LPI	Low Permittivity Insert
FR4	Flame Retardant 4
S-DRA	Super-shaped DRA
LCDRA	laterally fixed cylindrical DRA
DG	Diversity Gain
MEG	Mean Effective Gain
CAGRDRA	Cylindrical Air-Gap RDRA
AR	Axial Ratio
GD	Group Delay
MPS	Metallic Parasitic Strip
Al_2O_3	Aluminium Oxide

LIST OF SYMBOLS

Symbol	Description
ε_{DR}	Electrical Permittivity of Dielectric Resonator
ε_r	Relative Permittivity
μ	Permeability
ε_0	Free space permittivity
ω	Angular Frequency
σ_s	Conductivity
J_s	Current Density
E	Electric field Intensity
H	Magnetic Field Intensity
D	Electric Displacement
k (k_x, k_y, k_z)	Wave Propagation Number
f_0	Resonant Frequency
tan δ	Loss Tangent
B	Static Magnetic Field
χ	Susceptibility
ε_{reff}	Effective Dielectric Constant
ρ_e	Envelope Correlation Coefficient
λo	Free Space Wavelength
π	Pi
S_{mn} (S_{11}, S_{12}…….)	Scaterring parameters (S-parameters)
Q	Quality factor
ε	Absolute Permittivity
v	Speed of Light
V	Volume

LIST OF FIGURES

LIST OF TABLES

TABLE OF CONTENTS

CHAPTER 1

INTRODUCTION

1. Introduction

1.1 History of Wireless Communication

Wireless communication is a rapidly rising technology in which information is exchanged between two points without direct contact. The demand for the mobile wireless communication industry is increasing as their products, such as mobiles, are now considered as a necessity of life. It is common practice among cellular telephone producers and service providers to categorize wireless communication systems into numerous generations. First-generation (1G) systems are voice-oriented analog cellular and cordless telephones. Second generation (2G) wireless networks are voice-oriented digital cellular and personal communication system (PCS) and data-oriented wireless wide-area network (WAN) and local area network (LAN). Third generation (3G) networks integrate cellular and PCS voice services with various packet-switched data services into a single unified network. In parallel with appropriate 3G standardization activities, broadband local and ad-hoc networks developed their standards and attracted much attention. The fourth-generation (4G) is a complete internet protocol (IP)-based network system. It introduced the Long Term Evolution (LTE) standard, which supports only packet switching and an entire IP network. Global System for Mobile Communications (GSM), Universal Mobile Telecommunications System (UMTS), and Code-Division Multiple Access (CDMA) voices called in 2000 required significant changes in the infrastructure supplied by service providers, so after adopting LTE with circuit-switched, carriers will have to re-engineer their voice call networks. The fifth generation (5G) is the next generation for commercial cellular networks, significantly increasing Internet connectivity speed. One of the primary benefits of enhanced connectivity is plugging the Internet of Things (IoT) into an underlying selling point of 5G, which will have the highest connectivity speed to allow seamless integration of large-scale devices [1][2]. Table 1.1 mentions the detailed features of different generation networks and the core networks available for each generation.

1.2 Role of UWB Technology in Current Communication Scenario

The usage of Ultra Wide Band (UWB) wireless technology in the present wireless communication environment has clearly reported tremendous expansion. It is used as a radio pulse and

Table 1.1: Comparison between 1G-5G

Generations	**Start/Development**	**Technology**	**Frequency**	**Bandwidth**	**Access System**	**Core Network**
1G	1970/1984	AMPS, NMT, TACS	30KHz	2-24 kbps	FDMA	PSTN
2G	1980/1999	GSM	1.8 GHz	14.4-64 kbps	TDMA/ CDMA	PSTN
3G	1990/2002	WCDMA	1.6-2 GHz	2Mbps	CDMA	Packet Network
4G	2000/2010	LTE, WiMax	2-8 GHz	2000 Mbps – 1 Gbps	CDMA	Internet
5G	2010/till date	4G + wwww, MIMO	3-30 GHz	1 Gbps & higher	OFDM	Internet

unconventional for transmitting data over an extensive bandwidth range greater than 500 MHz. It is a technique to achieve high data rates with the intake of low power.

The US Federal Communications Commission (FCC) has granted authorization to use unlicensed frequency bands from 3.1 to 10.6 GHz for UWB communications [3]. A comparison of UWB globally is shown in Table 2.

The International Telecommunication Union-Radio (ITU-R) communication explained the UWB as a transmitting mode that the bandwidth range of the transmitted signal is more than 500 MHz, suggesting that the fractional bandwidth is more than 20 % in the entire transmission media [4]. As shown in Figure 1.1, the UWB power is assumed to be a small value and very close to the noise floor, which reduces its blocking and detection by intruders [5]. Currently, UWB technology has been improved for many benefits and use in future wireless applications. It has different applications in remote communication systems, detecting and monitoring systems, positioning and tracking systems (military and sports), RADAR, bio-imaging systems, etc.

Table 1.2: Ultra wideband global standards

Country	America, Canada	Japan	Singapore	Korea	Europe
Frequency Band Limit	Unlicensed Band from 3.1 – 10.6 GHz	.4-4.8 GHz Restricted 7.25–10.25GHz unlicensed band	6–9GHz ; 3.4–4.2GHz Restricted	3.1–4.8GHz Restricted; 7.2–10.2GHz	3.1–4.8GHz Restricted 6–8.5GHz
Regulation Authority	FCC	MICs	IDA	ETRI	ECC

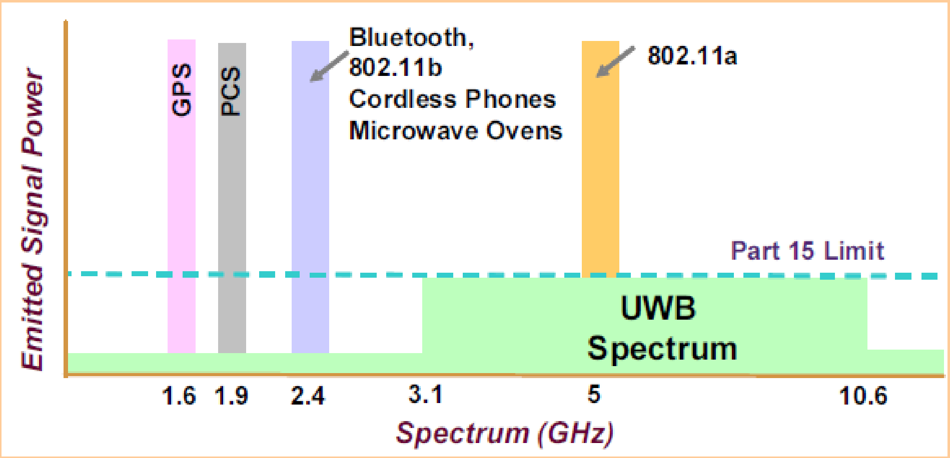

Figure 1.1: Allocation of spectrum for UWB Application [3]

UWB communication system compares with the traditional narrow system as time and frequency domain behavior, shown in Figure 1.2. UWB communication systems are attracting the researcher's attention because of the following:

- The data speed rate is extremely high in UWB communication up to 500 Mbps, low transmission power consumption for signal processing, and the highest versatility.
- UWB is an advanced technique to deploy less path loss and better immunity to multipath propagation.

- The UWB signal has lower susceptibility for the multipath interference to transfer the information with ultra-short duration waveforms.
- The transceiver structure is very simple because of the absence of the carrier, and it is easily available at a low cost.

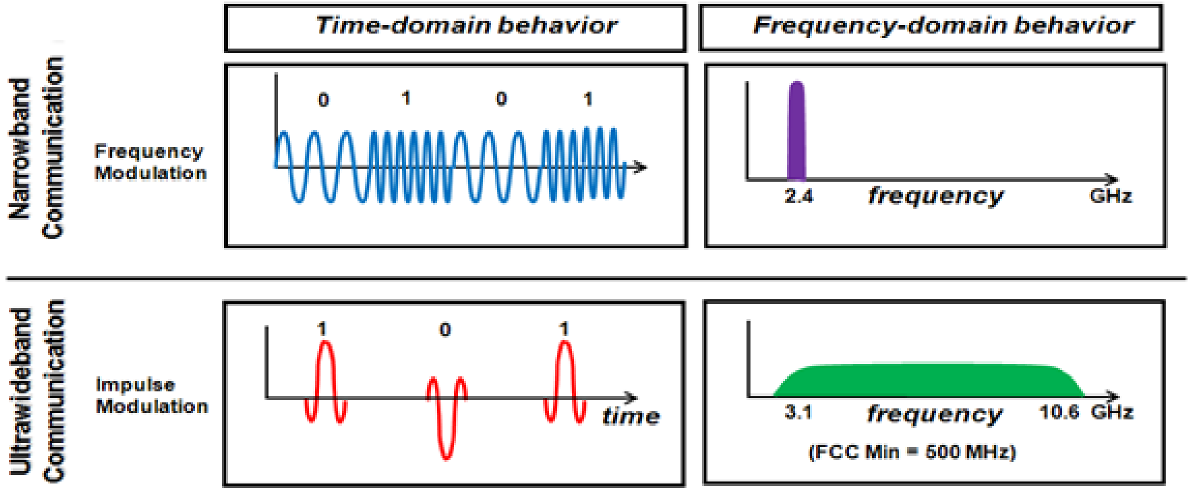

Figure 1.2: Comparative Analysis of Narrow-Band and Ultra-wideband Technologies

The main applications of UWB technology are permitted in codeless communications, intercommunications, military, short-range applications, imaging of radar, and localization systems. Some other applications are given below:

- Smart Car Access
- Secure Building Access
- Smart Retail
- Asset Tracking
- Sports & Fitness Tracking
- Wearable Health Sensors Medical Radars
- Indoor Navigation
- Smart Home
- Warehouse Positioning

1.3 Challenges in UWB Communication Systems

However, UWB communication systems have some significant challenges, as mentioned

- Generally, the transmission power level of the UWB is dependent on the existence of the UWB device and the other wireless system.

- The main challenge in the UWB system is the design of antennas.
- Due to the power limit set by FCC, the high data rate is available only in short range (<10 m).
- Another problem is associated with the ultra-short duration of the UWB pulse, which will lead to a higher number of resolvable multipath components at the receiver. As in a commonly received UWB signal, there are several delays. The scaled replicas of transmission pulses are present as each of these resolvable pulses will go through the separate channel fading. Thus this will make the multipath capture problem a significant issue in the UWB system design.
- The military used the UWB radio, whereby the multiuser transmission and high multiuser capacity was not significant issue. But this is the major issue when we use UWB systems in commercial applications like high-speed wireless home communications etc. Thus, we need effective coding and modulation schemes to improve the UWB multiuser capacity and increase system performance.

An antenna that can excite a UWB operation is a crucial component of UWB communication systems.

1.4 Antennas for UWB Communications

The antenna provides a conventional structure between radiating and receiving electromagnetic (EM) waves [6]. It is necessary to realize that the antenna radiates the energy from time-varying currents. An antenna converts bound circuit fields into the propagation of EM waves and mutually collects power by passing EM waves. Maxwell's equations predict that any time-varying electric or magnetic field produces the opposite field and produces an EM wave [7]. Antennas are usually fabricated of conductors, and such different materials are used for planning. Fix antennas are used for commercial purposes and security applications. It is a kind of transducer that converts electrical energy into electromagnetic and vice-versa. In 1921, Marconi gave the idea that signals can be transmitted in free space using a radiating device called an antenna. Since then, a number of advancements have been reported in the field of antennas [8]**.** The antenna is a key element of the wireless communication system. Several antennas have been developed to make wireless communication systems more efficient, like wire, aperture, reflector, microstrip patch antenna (MPA), and dielectric resonator antennas (DRAs) [6]. Today UWB antennas have attracted a great deal of attention in industries and academia for applications in wireless transmission systems [9] [10]. A UWB antenna can be used to replace many narrowband antennas. In 1898, Oliver Lodge first presented the concept of the UWB antenna design, and after that, several UWB antennas were developed. Aspects such as manufacturing cost and complexity of processes became essential considerations in the design of these antennas. In the current wireless communication era, MPA and DRAs are preferred for achieving the UWB range. Both antennas as single element or in array environment are capable of many wireless applications. However, metal and dielectric losses are usually associated with most MPA when printed on dielectric substrates [11]. On the other hand, there is no metal loss for DRAs. Therefore, they have the inborn advantage of high radiation efficiency at high frequencies [12].

1.5 Dielectric Resonator Antennas

1.5.1 Dielectric Resonators and Antennas

Resonators are significant segments in microwave communication systems. They work as frequency-determining components in filters, oscillators, amplifiers, tuners, etc. A resonator is 'resonating' at a particular frequency when the EM energy is stored inside the resonator like an inductor-capacitor-resistor (LCR) circuit. Recent advances in communication systems have increased transmitter and receiver channels in a particular geographical area. Therefore, one must choose the microwave and millimeter frequency range to prevent interferences due to the channels. The global satellite system, now in operation, uses microwaves to transmit meteorological data, telemetry, and international telephone and television channels. The allocated frequencies and noise limit the acceptable range of operation. The progress in integrated circuit technology led to the miniaturization of components used in microwave communication circuits. But recent progress in electronic ceramics technology has proved that temperature stable, high Q resonators for almost all microwave integrated circuit (MIC) applications can be utilized. Some ceramic materials, known as dielectric resonators (DRs) [13], are beneficial for application in the range of microwaves, millimeters, and high frequencies. DR has a high dielectric constant (ε_r), high-quality factor (Q), and small temperature coefficient of resonance (t_r) at microwave frequency [14]. Tools employing DRs are easy to use, low cost, small size, lightweight, and high efficiency. The versatility and adaptability of DRs have made them essential components for filters, oscillators, etc., in modem microwave integrated circuit (MIC) applications [15]. Therefore, recent advances in cellular radio systems, satellite TV, military radar, etc., have increased the demand for DR. In materials technology, in particular, electronic ceramic technology has received much attention from scientists, who are researching new materials to meet the needs of communication explosion. The resonant cavity in DR depends on a dielectric structure whose relative permeability (ε_r) is considerably greater than 9. Under this high ε_r of DR can limit EM waves through multiple total internal reflections at the dielectric air interface. If the DR is resonating at a frequency(f_0), then the maximum wavelength that is related to the relative permittivity (ε_r) of the material. The wavelength of the resonance can be represented as $\lambda = {}^{c}/_{f_0}$ for a cavity operating at the same frequency, where c is the velocity of the electromagnetic wave in free space. If v is the velocity of the EM wave in the medium, it can be written that

$$\frac{c}{v} = \frac{f_0 \lambda}{f_0 \lambda_d} = \frac{\sqrt{\mu \varepsilon_0 \varepsilon_r}}{\sqrt{\mu \varepsilon_0}}$$

$$\frac{\lambda}{\lambda_d} = \sqrt{\varepsilon_r}$$

where λ_d is the wavelength of EM wave in the dielectric [16]. The above equation shows that the fundamental wavelength in the air for the same frequency is $\sqrt{\varepsilon_r}$ times that in the dielectric. Thus to obtain a fundamental resonance at a specific frequency, if a DR of ε_r=100 is used, its size will be 1/10 of a cavity resonator operating at the same frequency. A resonant wavelength (λ_d) inside the DR is η times smaller than the corresponding free-space wavelength (λ_0) and where η is the refractive index, that is, inside a cavity (η = 1). Since η is approximately $\sqrt{\varepsilon_r}$ **,** the size of a DR is considerably smaller than that of an empty cavity operating at the same frequency. The size of a resonator can be further reduced by using coaxial $\left({}^{\lambda}/_{4}\right)$ Resonators, which have space between the inner and outer conductors filled with dielectric materials. In this case, the wavelength is related to the length by the equation

$$L = \frac{\lambda_0}{4} \frac{1}{\sqrt{\varepsilon_r}}$$

Where L is the length of DRA.

1.5.2 Characteristics and Advantages of DRA

The main characteristics and advantages of DRAs are high power capability, high radiation efficiency, compact in size, wide bandwidth, ease of excitation, less conductive loss, etc.[17]. Some properties and advantages of DRAs are given below:

- The dimension of DRA is proportional to λ_0/ε_r , where ε_r is the dielectric constant of the material.

- The absence of surface waves and minimal conductor loss is associated with DRA. By selecting low-loss dielectric materials, high radiation efficiency and directivity can be achieved. This is an attractive feature for designing millimeter-wave antennas, where losses can be more significant in metal-built antennas.
- The physical size and operating bandwidth can be varied over a wide range by selecting different dielectric constant materials.
- Each mode of DRA has its own unique intrinsic and associated external field distribution similar to a small electric or magnetic dipole, which can produce either broad or unidirectional radiation patterns.
- Several feeding mechanisms (including probes, slots, microstrip, and coplanar waveguide lines) can be used effectively in DRA, making them responsible for integration with various existing technologies.

1.5.3 Operating Principle of DRA

There are three types of boundary conditions that can be utilized to describe the working principle of the DRA. The three media are the electric wall, magnetic wall, and dielectric interface (Pozar, 2005).

1. In the case of an electric wall, Maxwell's equations can be written as

$$\hat{n}.D = \rho_s$$

$$\hat{n}.B = 0$$

$$\hat{n} \times E = 0$$

$$\hat{n} \times H = J_s$$

2. In the case of a magnetic wall boundary condition, the tangential components of the magnetic field are absorbed by the magnetic surface.

$$\hat{n}.D = 0$$

$$\hat{n}.B = 0$$

$$\hat{n} \times E = -M_s$$

$$\hat{n} \times H = 0$$

3. The dielectric interface can be considered as the coupled region where the fields are coupled from one dielectric medium to another dielectric medium.

$$\hat{n}.D_1 = \hat{n}.D_2$$

$$\hat{n}.B_1 = \hat{n}.B_2$$

$$\hat{n} \times E_1 = \hat{n} \times E_2$$

$$\hat{n} \times H_1 = \hat{n} \times H_2$$

In the case of DRA, the radiator is made of ceramic or an insulator, so we cannot apply the boundary conditions of the electrical wall. Another approach is to assume the boundary condition of the magnetic wall around the DR, which the researchers initially adopted. The problem with the magnetic wall boundary condition is that the tangent component of the magnetic field is the only source of energy transfer from the DR to the free space that becomes zero. As a result, the boundary condition of the magnetic wall cannot be applied to outer surface of the DR. The only boundary condition that can be imposed with the operation of DR is the coupled field boundary condition. Electromagnetic radiation is caused by oscillations of electrons, which causes acceleration and de-acceleration. The DRA operation is based on the phenomenon of how the DR radiates when the excitation is applied. It is found that DR should be radiated in free space [18]. It considers the periodic solution of Maxwell's equations of DR placed in free space. He explained the concept by assuming that the DR is placed in a spherical coordinate system. The origin is on or near the DR with the system's coordinates designated as r, θ and ϕ.

The resonator is of finite dimensions, and a sphere around it can be considered as the radius of R. Using the concept of vector wave equations in a spherical coordinate system, the field can be viewed as a fundamental set of solutions applied outside the sphere. For these fundamental sets of solutions, the sum of squares of their coefficients is supposed to be proportional to their power. This implies that zero power means all the coefficients of the solutions have vanished. Using the principle of analytical continuity, the field outside the resonator must vanish identically in the free space or just outside the resonator. Using the boundary condition on the outer surface of the DR implies that the tangential component of electric field intensity (E) and normal component of electric displacement (D) must be continuous. Therefore, the field should simply disappear outside the resonator since the dielectric constant is finite. This means that non-radiative regions are zero everywhere. The wave equation is of second-order in time derivative, and it is essential to be considered. But by the nature of electromagnetic waves, the field cannot disappear outside the resonator if oscillations are present. The area can be located outside the resonator by the current distribution due to the movement of ions inside the DR. This causes radiation to occur due to oscillations outside the DR and hence it radiates.

When DRA is excited, the radio waves fed within the DR and bounce back and forth within the resonant walls resulting in standing waves rising. These standing waves store energy in the form of electric field components **E** and magnetic field components **H**. Due to the accelerating current, the time-varying field radiates into the free space of the DRA. Due to the fringing effect, the magnetic field leaks into the environment through the walls of DRA in free space.

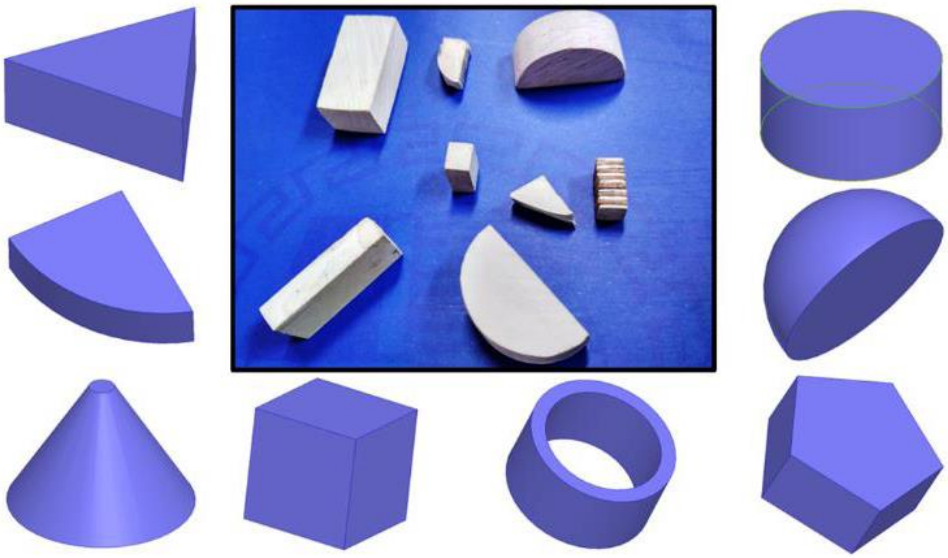

Figure 1.3: Different shapes used for DRA [10][15]

The foremost common shapes of DRAs are cylindrical, rectangular, and hemispherical, shown in Figure 1.3. These are three shapes and their corresponding field mode configurations. The input excitation cavity volume and boundary conditions affect the DRA resonance mode excitation. At resonance, standing waves are formed depending on the given characteristics. Because of the translucent walls, standing waves are transformed into traveling waves (boundary conditions). Magnetic energy is always equal to electric energy, i.e., resonant modes can be excited as Transverse electric (TE) [19], transverse magnetic (TM), transverse electromagnetic (TEM), hybrid electric (HE), and hybrid electromagnetic (HEM) modes are all terms used to describe. DRA has the ability to stimulate first or higher-order modes like (TE_{111} ……… TE_{lmn}) (TM_{111} ……… TM_{lmn}) [10]. They can be used for achieving the UWB range by using the mode merging concept.

1.5.4 Parameters of DRA

Various parameters play an essential role in the study of DRAs. These parameters include dielectric constant, Q-factor and resonant modes, etc. All these parameters are discussed in detail as follows.

1.5.4.1 Dielectric Constant

The dielectric constant is defined as "the ratio of the amount of electrical energy stored inside the material when an external voltage is applied to that of the energy stored in a vacuum." It is denoted as ϵ_r. The dielectric constant of a material concentrates on the electrostatic lines of flux under the given conditions. The dielectric material supports the E-field when the energy is minimized as heat energy. The net electric flux density (D) can be expressed mathematically:

$$D = \varepsilon_0 E + P$$

$$P = \varepsilon_0 \, \chi E$$

$$D = \varepsilon_0 (1 + \chi) E$$

Where 'P' is net polarization, χ is the electric susceptibility, and E is electric field intensity. It is mathematically expressed as follows:

$$\varepsilon_r = 1 + \chi$$

$$D = \varepsilon_0 \varepsilon_r E$$

$$\varepsilon_r = \varepsilon_r' - j\varepsilon_r''$$

Where ε_r' is the dielectric constant and loss tangent is formulated by $\tan\delta = \left(\frac{\varepsilon_r''}{\varepsilon_r'}\right)$ is called or dissipation factor of the dielectric.

Dielectric polarization occurs when the electromagnetic field passes through the dielectric material. It defines the dielectric property of the DR. DR consists of the permanent electric dipoles, which are randomly oriented. These randomly oriented dipoles align themselves in the direction of the field. This whole phenomenon is called polarization of the dielectrics.

1.5.4.2 Quality Factor

The Q-factor of the DRA can calculate by using equation

$$Q = \frac{\omega W_s}{P_{rad}}$$

Where, W_s is the energy stored and, P_{rad} is radiated power.

The value of multiple losses and electrical energy dissipation due to losses from various activities such as radiation, conduction, dielectric, surface wave, and non-linear processes is represented by the Q-factor of the antenna. The total Quality factor (Q_t) is given below:

$$\frac{1}{Q_t} = \frac{1}{Q_{rad}} + \frac{1}{Q_c} + \frac{1}{Q_d} + \frac{1}{Q_{sc}}$$

Where Q_t, Q_{rad}, Q_c, Q_d, and Q_{sc} are Q-factors due to radiation, conduction dielectric and surface wave losses, respectively.

1.5.4.3 Impedance Bandwidth

The impedance bandwidth illustrates the bandwidth over which DRA radiates or receives energy appropriately. Impedance Bandwidth of antenna can be defined in the following three categories: Narrowband covers a small range of the order of a percent in the area of bandwidth operating frequency.

$$BW = \frac{f_h - f_l}{f_c} \times 100$$

Where, f_h= higher frequency

f_l =lower frequency

f_c = center or resonant frequency

Wideband or Broadband - These antennas cover frequencies of an octave or two range.

$$BW = \frac{f_h}{f_l} \times 100$$

Ultra-wide Band- Impedance Bandwidth is defined as 10dB reflection coefficient or SWR within the frequency band. The bandwidth in the form of Q-factor and VSWR can be defined as given below:

$$BW = \frac{VSWR - 1}{Q\sqrt{VSWR}}$$

$$Impedance\ BW = \frac{f_h - f_l}{\sqrt{f_l f_h}} \times 100$$

VSWR can also be present in the form of reflection coefficient i.e. $|\Gamma|$ as given below:

$$VSWR = \frac{1 + |\Gamma|}{1 - |\Gamma|}$$

1.5.4.4 Input Impedance

Mainly three types of impedance are studied for antennas as given below:

(i) Terminal impedance for antenna

(ii) Characteristic impedance for transmission line

(iii) Wave impedance for waveguide or dielectric.

Input Impedance has usually described the ratio of voltage to current at interconnections where the transmission line is coupled with an antenna. Absolute energy coupling is possible when the transmission line impedance is approximately the same as the antenna's impedance and has no reactive element. Normally antenna is designed so that its impedance is fixed around 50 ohms and matched with the coaxial cable.

1.5.4.5 Radiation Pattern

The radiation pattern of an antenna is the mathematical representation and graphical depiction of far-field radiation of an antenna. It represents a graphical spatial variation of electric or magnetic fields along a constant radius. The radiation pattern is studied in terms of power flux density, radiation intensity, and field strength. It provides information about the power radiated by DRA in the direction of the far-field region. Polar and the 3-D radiation pattern are shown in Figure 1.4.

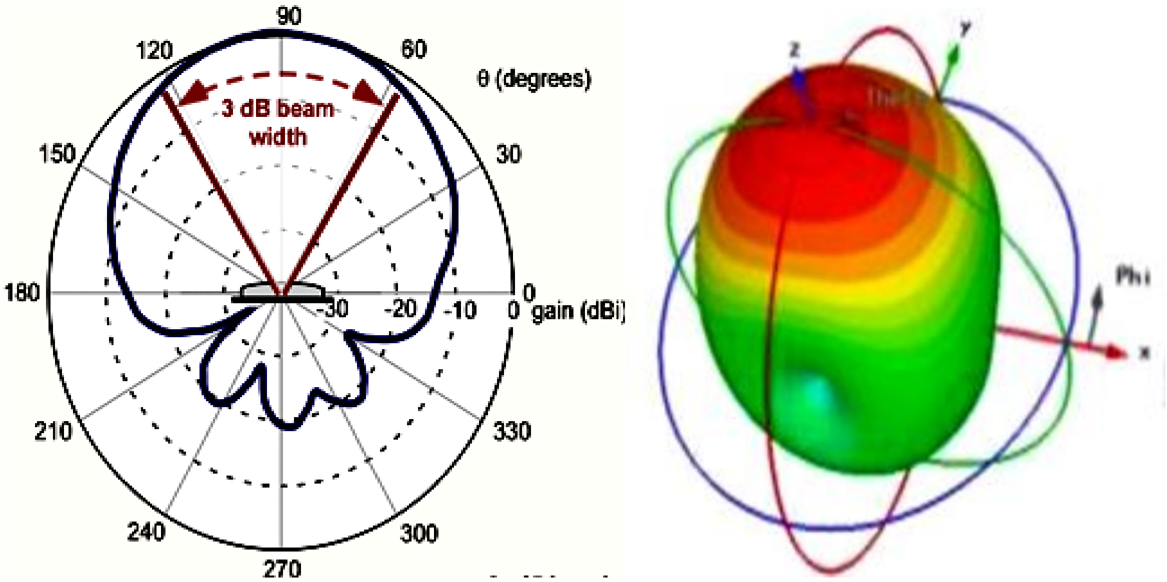

a b

Figure 1.4: Radiation pattern: a. Polar plot, b. 3-D plot

1.5.4.6 Polarization

Polarization of antenna is a point of reference of an electric field in the direction of maximum electric field strength. Usually, the plane that encloses electric and magnetic fields is called the plane of polarization that is always orthogonal to wave propagation. The preferred polarization of a wave is known as co-polarization, and orthogonal radiation is known as cross-polarization.

The polarization of transmitting and receiving antennas is essentially matched for maximum gain of systems. The selection of polarization such as Linear, Elliptical [20], and Circular [21]–[23] is also crucial for proper signal propagation.

1.5.4.7 Directivity and Gain

The Gain (G) and Directivity (D) of an antenna are closely related. The gain of an antenna is a ratio of radiation strength in a particular direction and radiation strength equally distributed in all directions. Gain expresses how much power is transmitted in the direction of peak radiation for an isotropic source. The radiation focusing capability of antennas is determined by the Directivity (D). Since directivity depends on the shape of the directive pattern, any power loss in an existing antenna system is not considered. Directivity describes the competence to guide power in a particular direction in comparison to other directions. Directivity is the ratio of maximum power density, i.e., Pmax and Average power density in the whole sphere:

$$D = \frac{P_{max}}{\frac{1}{4\pi}\int_{\theta=0}^{\pi}\int_{\emptyset=0}^{\pi} P(\theta,\emptyset)\sin\theta \;\, d\theta \; d\emptyset}$$

$$Directivity = 10\log_{10} D \text{ (dBi)}$$

1.5.4.8 Radiation Efficiency (η)

Radiation efficiency describes how efficiently the antenna transmits and receives RF signals. The ratio of the radiated power and the input power received from the antenna is called the radiation efficiency. Radiation efficiency is formulated in the term of Directivity (D) and Gain (G) as given below:

$$\eta = \frac{G}{D}$$

1.5.5 DRAs Excitation Techniques

The different feeding techniques that are used to feed DRAs include the following: the conducting probe; aperture coupling; coplanar waveguide; and microstrip feedline. The feed dimensions of tapping are the factors used to control impedance matching of the antenna with feedline [15] [24].

1.5.5.1 Coaxial Feeding Mechanism

The probe excitation requires drilling a hole in the ground to insert the probe connected to the DR, as shown in Figure 1.5. Probe dimensions are factors that control impedance matching. High permittivity DRAs can also be efficiently stimulated by placing the conductor probes near the outer surface.

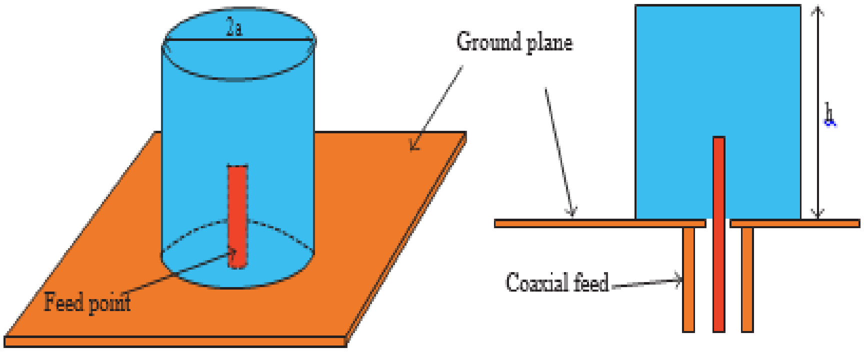

Figure 1.5: DRA using coaxial fed [15]

1.5.5.2 Aperture Coupled Feeding Mechanism

The most famous feeding techniques for DRA mentioned in the literature is using slot or aperture on the ground plane. The feed line of antenna is printed on bottom of the substrate and depicted in Figure 1.6. Figure 1.6 shows the 3D view of DRA. A DR is placed on metallic ground plane and excited by a feedline through a coupling slot.

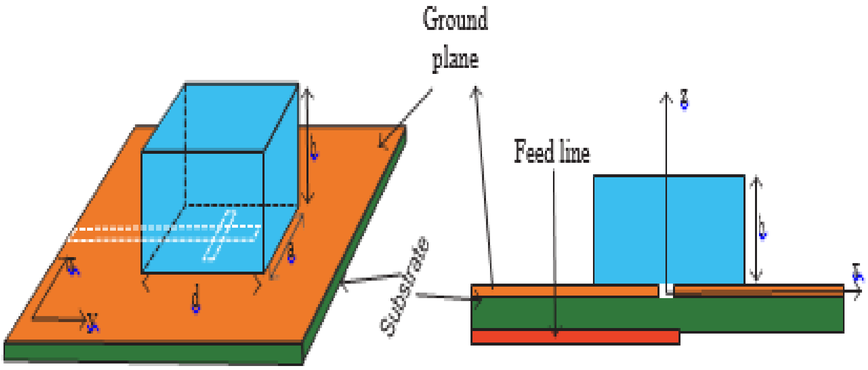

Figure 1.6: DRA using aperture coupled fed [15]

1.5.5.3 Microstrip Transmission Line Feeding Technique

In this feeding technique, a conducting strip is directly attached to the edge of the DR, as shown in Figure 1.7. The conducting strip is smaller in width as compared to length. Such feed arrangement has the advantage that it can be etched on the same substrate to provide a planar structure.

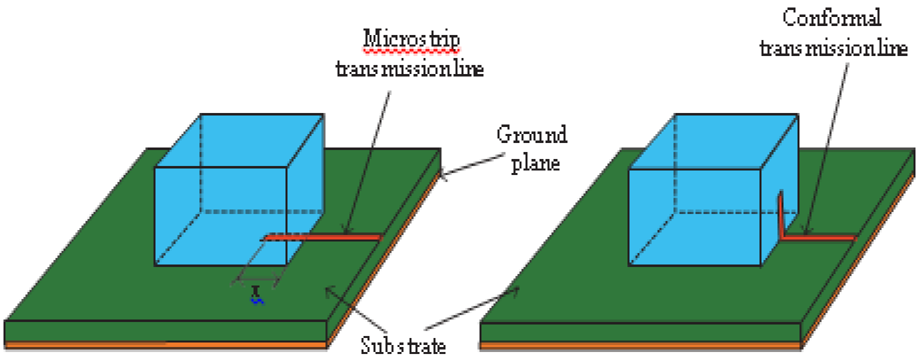

Figure 1.7: DRA using Microstrip fed with conformal transmission line [15]

1.5.5.4 Coplanar Feeding

As shown in Figure 1.8, coplanar waveguide (CPW) fed is circular loop with inductive and capacitive slots. To improve DRA performance, the coupling slot beneath the dielectric resonator can be modified, which is the main advantage of CPW excitation.

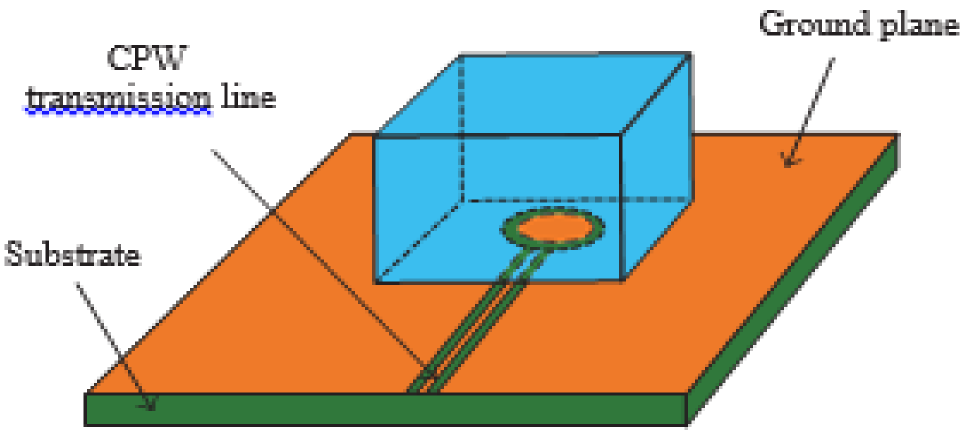

Figure 1.8: DRA using CPW fed [15]

DRA supports good data rates for services requiring high data rates such as 5G wireless communication. UWB technology has received more attention in current wireless communication. Compared to MSA, the conventional DRAs provide 10-20% more bandwidth, which cannot cover the UWB range, so some techniques are implemented to increase the performance parameter of DRA to achieve UWB range, and the next section discusses some DRA performance parameters for enhancing the characteristics.

1.5.6 Performance parameters of DRA for UWB applications

To support high data rates, good channel bandwidth, better efficiency, and gain with the DRAs, some techniques have been reported to enhance the performance of these parameters like impedance bandwidth, AR bandwidth, gain, and radiation pattern. A detailed study to improve these various parameters are reported in various review articles [14], [22], [25], [26].

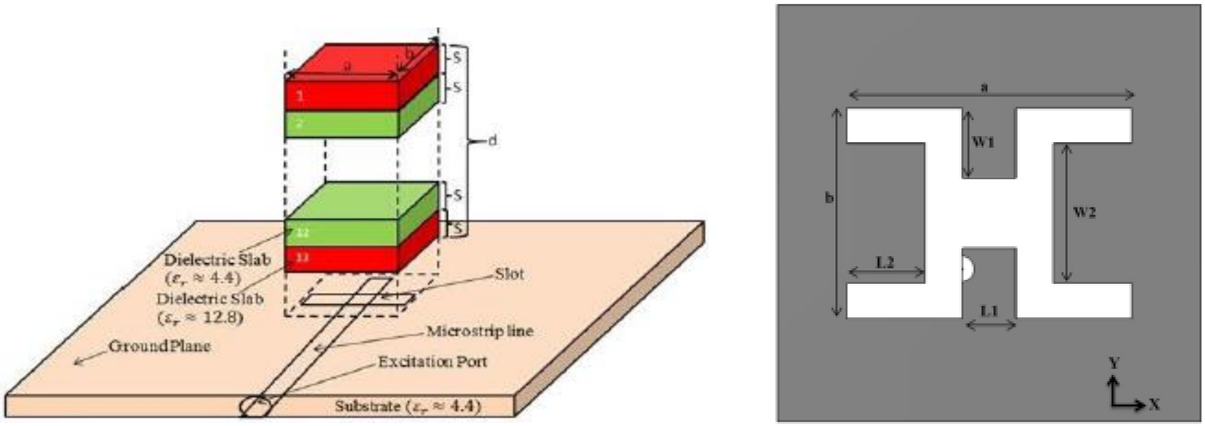

a [14] [24]

b [27]

Figure 1.9: a. Stacking of DRA, b. Perturbed DRA

Multi-input, multi-output (MIMO), is a technique for increasing the capacity of a radio link by employing multiple transmitting and receiving antennas to take advantage of multipath propagation. Over the past several decades, MIMO has become a more popular RF/microwave communications technology, notable examples include short- and long-distance communications for high data rate applications [28].

1.5.6.1 Bandwidth enhancement techniques of DRA

Although DRA provides a broader bandwidth than MPA, we need to develop some methods to enhance DRA bandwidth. The methods have been reported in existing literature previously. The bandwidth of DRA can be increased utilizing a variety of methods, including stacking and perturbing approaches [27], [29]. After that, the concept of insertion of air gap between the ground plane and inside the DR was reported to enhance the bandwidth [30], [31]. The impedance bandwidth of the DRA can also be improved by creating an air-space within the DR structure. In this research, the effect of the aspect ratio of DR on the antenna bandwidth has also been reported. This suggests that because to DR's high aspect ratio, a large number of modes are kept close together. The bandwidth of the DRA increases due to the merging of adjacent modes. Generally, an aspect ratio of more than one is considered the high aspect ratio of the DR. Recently, a study was carried out to enhance the bandwidth using dielectric slabs specifically, as shown in Figure 1.9. This work defines how the bandwidth of DRA can be controlled by adjusting the modes generated inside the DR. A simple concept to enhance DRA bandwidth is that it excites a large number of nearby modes, which enhances the performance of DRA. The conical structure was also reported to utilize the concept of bandwidth enhancement [32].

1.5.6.2 Gain enhancement techniques of DRA

There are different techniques for gain enhancement that researchers have reported. One of the studies was reported elaborating that introducing higher-order modes inside DR results in the enhancement of Gain [33]. The Gain of DRA is also improved by stacking the DR elements [34] [35]. Researchers reported the stacking DRA elements for the gain enhancement [36]–[38]. Recently, we carried out a technique to enhance the gain and bandwidth by using the hybrid patch and DRA [35]. Here a slotted microstrip patch is used to feed the DR. DR was loaded to the rectangular patch to enhance the Gain [36]. Some-time perturbation concepts of DRs are used to enhance gain or directivity characteristics.

Therefore DRA has several advantages over MSA, such as controlling metal and surface wave losses, and 10-20% widen band of operation has motivated us to carry out research work in the field of UWB DRAs for 5G applications. The thesis outline is as presented below.

1.6 Motivation

In the extensive literature survey carried out above, it is observed that the current wireless communication system requires DRAs that have optimum size, provide good impedance bandwidth, AR bandwidth, gain, and radiation efficiency. Additionally, it is observed that MIMO UWB DRAs are preferred choice in the 4G / 5G communication systems as they can provide better bandwidth and better diversity with EP/CP characteristics to overcome the loss in signal and to improve the strength in 5G communication systems.

The available research gaps in the area of DRAs are outlined in the next section that helps in define the objective of the proposed doctoral research work.

1.7 Research Gaps

DRA can be used for narrowband, wideband, UWB, millimeter, and high-frequency applications. The literature survey has been done in the field of UWB DRA and arrays of UWB DRAs, which provide an excellent bandwidth for high data rate applications that support multimedia series.
However, some of the research gaps found during the literature survey of DRAs are listed below.

1. High gain DRA have been reported with very complex structures. Work can be done to get good benefits from DRA with simple structures in UWB applications.

2. There is not much work reported in the literature on using hollow or stacked and segmented DRAs with the same or different dielectric constants for UWB operations.
3. Many DRAs are available for wideband/UWB applications, but UWB DRAs with elliptical or circular polarization is an open area of research.
4. MIMO DRA arrays can be designed with good isolation properties between the antenna elements. UWB MIMO DRA is an open area of research.

1.8 Research Objectives

Based upon the research gaps listed in the section, a few research objectives are proposed for the current doctoral research work as below:

1. To study Dielectric Resonator Antennas, their geometries, operation, and mathematical analysis for UWB applications.
2. To design, simulate, fabricate and test, super shaped UWB DRA for future wireless applications.
3. To design, simulate, fabricate and test an elliptically or circularly polarized UWB Dielectric Resonator Antenna.
4. To design, simulate, fabricate and test a DRA array for multiple-input multiple-output (MIMO) applications.

1.9 Research Contribution

According to the research objectives, the main contribution of this thesis is to employ the UWB DRA with high or constant gain. This thesis focuses on key aspects of DRAs, to design UWB DRA as EP / CP, MIMO with compact in size. The main contributions of the objective-based research work are summarized and discussed in chapters 3-6.

1.10 Thesis Outline

The thesis aims to detail some typical UWB DRA configurations for the future wireless communication system. It is organized into six chapters, with a summary of each chapter given below:

Chapter 1: Introduction

The UWB technology is discussed in this chapter, along with its different benefits, characteristics, and applications. The chapter mentions the details on the usage of DRAs for UWB operation characteristics. In addition, possible solutions to the problems faced by the UWB DRA and the organization of the thesis are presented.

Chapter 2: Literature Survey

This chapter is organized into subsections and offers an in-depth study of the relevant literature. The first part shows the introduction. The second part includes the literature survey, which is further divided into some subparts. The third part includes motivation. The fourth part consists of the research gaps, and the fifth Part of chapter 2 consists of the objectives of the doctoral research work.

Chapter 3: Cylindrical Air-spaced Dielectric Resonator Antenna

This chapter presents a new geometry air-spaced DRA that is proposed to enhance the gain and impedance bandwidth of the proposed antenna. A cylindrical-shaped structure is removed from a rectangular DR. The DR is excited by a quarter-wave transformer type fed printed on top of the substrate and the bottom layer of the substrate has a partial ground plane with a rectangular-shaped DGS. The impedance bandwidth of the proposed DRA is 104.09% (3.28-10.4 GHz).

Chapter 4: Elliptically and circularly polarized Dielectric Resonator Antenna for UWB Operation

This chapter presents the design of EP/CP DRA with UWB characteristics, which is divided into two parts as first and second design. The first design discusses an elliptically polarized 'OM' shaped DRA, excited by an inverted P-shaped feedline and rectangular-shaped DGS cut from the infinite ground. The performance of the proposed antenna is compared without perturbed DRA. The second design discusses a CP asymmetrical-shaped DRA with the modified ground. This DRA consists of two ceramic blocks, segmented with similar permittivity material and excited by a transformer-type microstrip feedline with 50 Ω.

Chapter 5: MIMO Dielectric Resonator Antennas for UWB Operation

This chapter presents the two design of MIMO DRA for UWB operations. In the first design, a two radiator-based MIMO UWB rack-shaped DRA. Two rectangular-shaped radiator elements are used to create the proposed MIMO antenna design, which is then turned into a rack-shaped DR. An inverted T- shaped metallic strip and DGS is used to achieve the UWB operations. In the second design, a cross-shaped metallic parasitic strips based MIMO DRA excited by QWT microstrip feedline, designed, simulated, and fabricated. Inverted T- shaped metallic strip, scissor-shaped DGS, and ground stub to improve the impedance bandwidth, and to enhance the isolation using ground stub and cross-shaped metallic strips within the UWB operations.

Chapter 6: Conclusion and Future Work

Finally, the conclusion of the research work performed in this thesis is summarized. It also draws the achievement of the designed UWB DRA, and its possible future scope is documented in this last chapter of the thesis.

CHAPTER 2

LITERATURE SURVEY

This chapter presents the literature survey done in context to UWB DRAs. An extensive literature survey in this regard led to identifying research gaps and the definition of the objective for the proposed doctoral research work. The chapter is ordered into six distinct sections. Section 2.1 discusses the history of DRAs. Section 2.2 discusses the literature review on UWB DRAs, and it has subsections; 2.2.1 to 2.2.10. Sections 2.3 to 2.6 discuss the motivation, research gaps, research objectives, and research contribution in context to the proposed doctoral work.

2.1 History of DRAs

It was reported that a dielectric material of a specific shape could serve as a resonator for high-frequency oscillations, known as Dielectric Resonator (DR) [18]. The analysis revealed that the DR must radiate in an open environment (free space). The concept of resonant frequencies and the mode of oscillations was also stated in this study. The possibility of building a much smaller antenna using DR has also been explored [39]. A rigorous asymptotic theory for evaluating modes in a specific size DR was presented, along with the nature of the irradiated field [40]. The first experimental study on a cylindrical DR cavity was reported in 1983 [41]. A rectangular DRA was also analyzed and presented in 1983[42]. Later in 1984, a hemispherical DRA was implemented. The cylindrical DRA with the study of radiation characteristics and new applications was proposed in [43]. A half-split DR is used for the antenna application when placed on a metallic plane [44]. Later, the slot coupling method was used in half split DR, where the slot was used to define the fields that leak inside the DR structure to determine the modes [45]. Until then, research was carried out with new DR shapes with exciting appropriate feeding techniques. The radiation field, resonant mode, and field distribution inside the DR structure are all important factors to consider while building a DRA. Many research works have been done on the study of resonant modes and field distributions inside DR. These modes define the field pattern of the DRA. The resonant mode of the dielectric resonator was reported along with the characteristic equations of the current mode [46]. This research work investigated the existence of modes experimentally. In [47], Several resonant modes inside an open dielectric resonator were described, along with calculating their characteristics. The generation of modes in a cylindrical dielectric waveguide near and far from the cut-off frequency was reported [48]. Transverse and hybrid modes, as well as mode characteristics, were studied and analyzed.

In order to find out research gaps in the reported literature on UWB DRAs, the next section presents the available literature survey to same.

2.2 Literature Review on UWB DRAs

This section presents a literature survey on UWB DRAs. DRAs can effectively achieve the UWB range, and many researchers have worked in this area. Some of the reported work has been classified into different techniques for obtaining the UWB.

2.2.1 UWB DRA based on thin monopole

M. Lapierre *et al.* 2005 [49] designed a monopole-loaded single annular ring DRA with the same axial reference for UWB applications. The cylindrical DR is mounted on a finite ground plane, excited by a coaxial feedline combined with a quarter-wave monopole. The prototype antenna1 covered a frequency range of 6.3 to 16.2 GHz, and had a permittivity of 10 and a height of 10 mm. The prototype antenna2 covered the frequency range of 4.2 to 10.1 GHz, and had a high permittivity of 20 and height of 15 mm.

Y.F Ruan *et al.* 2006 [50] described a double ring concentric annular DRA. When monopole height was 6.8 mm, and both rings took different electrical permittivity (36, 4) with heights of 7 mm and 10mm, respectively, the antenna covered wide impedance bandwidth (5 to 5.9 GHz). Further, both annular rings offer similar electrical permittivity (20) with heights of 7 mm and 10mm, respectively. This antenna covered frequencies from 3 to 11.2 GHz when the height of the monopole was 22 mm. Monopole and concentric annular ring structures with different parameters achieved the UWB range.

Saswati Ghosh *et al.* (2008) [51] designed a hybrid antenna for UWB performance. This antenna had the concentric annular ring DRA with T- shaped thin monopole excited by a coaxial feedline. This monopole-based technique shifted the resonance to the lower end and adjusted the length along the loaded arm to improve the impedance bandwidth. This antenna covered the UWB range with 10 dB impedance bandwidth of 110% (4 to 15 GHz).

I. Zivkovic (2012) [52] described a DRA loaded with wire monopole to achieve UWB operations. The monopole consisted of a coaxial feedline with a 9 mm long wire on a 60 × 60 mm^2 ground plane and a 3.5 mm internal conductor with 50Ω input impedance. The introduction of dielectric (s2850 epoxy dielectric) loading made it possible to tune the antenna with an omnidirectional radiation pattern. It observed that the antenna reported three frequency bands from 6.8 to 9.04 GHz, 21.44 to 27.08 GHz, and 36.3 to 40 GHz, respectively.

Mahmoud Niroo-Jazi *et al.* (2012) [53] presented a novel DRA for UWB operations with band-rejection characteristics. The antenna structure considered was a monopole DR. Further, a spherical ring patch (SRP) formed on a grounded substrate. To manage the stop-band position and increase radiation performance, the SRP has a monopole built into the structure. The radiation efficiency of the antenna outside the stop band was more than 92.25%. It could be seen that a low cross-polarization level of less than -12 dB was reported within the entire frequency band.

Debatosh Guha *et al.* (2012) [54] investigated hybrid monopole DRA with improved UWB characteristics. Simply hemispherical and conical shapes were implemented as a dielectric ring resonator (DRR) with a monopole to enhance the impedance bandwidth. Using a conical DRR (CoDRR) of the same dielectric material, this antenna was compared to an earlier version, with a 25% larger impedance bandwidth while maintaining similar gain and radiation properties. These two antennas reported the frequency range from 4-16 GHz and 5.6-22.4 with a gain of 2–4 dBi.

M. Abedian *et al.* (2012) [55] designed a new compact two-segmented DRA (TSDRA) for UWB applications. This antenna involved a thin wire monopole filled with two DRAs with different dielectric constants and a compact overall antenna size of 18 × 36 × 11 mm^3. Through a modified TSDR excited by a U-shaped microstrip feedline, appropriate radiation characteristics were obtained. It provided a UWB range with high radiation efficiency. The TSDRA reported an impedance bandwidth of 110% from 3.09 to 11.5 GHz (simulated) and 3.14 to 10.9 GHz (measured).

Cengiz Ozzaim *et al.* (2014) [56] presented a stacked conical ring DRA (SCRDRA) stimulated by an axially symmetric coaxial monopole. The SCRDRA considers two cases: case 1, the two cones end upwards, and in case 2, the top cone was inverted to form a "sand-glass" shaped DRA. The proposed SCRDRA gives a fractional bandwidth of 138% from 2 to 16 GHz along with a monopole radiation pattern, and the gain of the antenna was reported as 4 dBi. Monopole antenna with 30 mm of height was given an impedance bandwidth of 143% and covered 2 to 12 GHz.

Seyyed H. Seyyedhatami *et al.* (2014) [57] presented a compact DRA for UWB applications. This antenna consisted of a truncated ground, modified transformer type monopole-based microstrip feedline for excited RDR, and a parasitic element was used underneath the DR layer.

The DR was mounted on the FR4 substrate with a size of 15×20×5.8 mm^3. The impedance bandwidth of the antenna was reported 153% (3.7 to 28 GHz) with peak gain of 6.05 dBi.

Ali A. Al-Azza *et al.* (2018) [58] developed a conical and cylindrical DRA stacked to each other and fixed vertically to achieve the UWB range. Vertically stacked annular conical CDRA was excited by a coax feedline having a cylindrical monopole. Comparative analysis of the antenna compared to other DRAs reported an impedance bandwidth of 148.6% (5.1 - 34.6 GHz) and a peak gain of 7.14 dBi.

Zhiwei Song *et al.* (2019) [59] investigated low-profile triangular DRA with printed planar monopole characteristics. The dimension of the prototype was 17.6 × 33.6 × 1.52 mm^3. The proposed stacked triangular DRA was excited by a CPW feed between two DR layers stacked with a rectangular patch. This patch-based DRA covered 3.2 to 10.96 GHz and 3.2 to 11.35 GHz with an impedance bandwidth of 109.6% and 112%. The antenna had shown low cross-polarization level and high radiation efficiency.

2.2.2 Air-gap based DRAs for UWB operation

T.A. Denidni *et al.* (2009) [60] introduced a new rectangular DRA (RDRA) for UWB applications. The RDRA was excited directly through a coaxial feed with a bevel-shaped patch and provided an air gap. The RDR was mounted on the ground with a size of 75×90 mm^2, and DR was made of Rogers TMM 10i with a size of 27.2×12.6×19.1 mm^3. The Q-factor and effective permittivity were reduced using air-gap between DR and metallic layer, and the bevel-shaped feed provided mode transition. The peak radiation efficiency of the antenna was 90%, and impedance bandwidth was 120% (2.6 to 11 GHz).

T. A. Denidni *et al.* (2010) [61] presented a new Z-shaped DRA for UWB applications. This antenna consisted of a Z-shaped DR, excited by a bevel-shaped patch coaxial feed, and an air gap was provided between the DR and ground plane. The Z-shaped DR was placed in the center on the metallic ground with 75 × 90 mm^2. The antenna's effective dielectric constant and Q-factors were reduced by providing an air gap and bevel-shaped feed. So widen bandwidth and impedance matching was achieved with an impedance bandwidth of 121% (2.5 to 10.3 GHz).

Yong Feng Wang *et al.* (2014) [62] presented RDRA for UWB and narrowband (NB). The UWB characteristic was achieved by port 1, where a bevel patch-based coaxial fed and air gap was provided between the ground and the RDR. Two identical short-circuited metal strips were introduced to achieve narrowband and provided good isolation between the two ports. These antennas were reported in two frequency bands from 2.4 to 12 GHz and 2.3 to 4.5 GHz, respectively. The isolation of antenna was improved by short-circuited metallic strips, and more than 10 dB isolation across the operating band was found, except 2 to 4 GHz band, where the peak gain value was 6 dB at 2.5 GHz.

2.2.3 Patch-based DRA for UWB

M. Aoutoul *et al.* (2009) [63] investigated a compact rectangular DRA (RDRA). This antenna was a low-profile RDR ($\varepsilon_r = 3, 10.2$) having the dimension of 10 ×10× 2.5 mm^3 placed on Rogers RT Duroid 3010 substrate (30 ×45×1.27 mm^3), with the dimension of truncated ground was 30× 25 mm^2. A metallic layer of 3.9375 × 3.9375 ×1.2 mm^3 was fixed beneath the DRA to improve the bandwidth (31%, 6.86 to 9.41 GHz) and impedance matching characteristics. An impedance bandwidth of 46% (6.9 to 11 GHz) was achieved by using a stepped slot in the ground plane.

Zi-bin Weng *et al.* (2010) [64] introduced a new CDRA excited by a CPW feed with a crescent patch-based antenna for UWB applications. This antenna consisted of a compact circular-shaped DR, a crescent-shaped patch using CPW feed, and a modified ground plane. The DR was placed on a substrate (60 × 60 mm^2) and chosen a relative permittivity of 35. The electromagnetic coupling was reported between the feeding patch and the DR. The DR was found to have well-matched bands that existed with fundamental mode (TE_{111}) characteristics at 1.9 GHz and some higher-order modes found at 6 and 9 GHz frequencies. This antenna covered a frequency range from 1.6 to 15 GHz.

T.A. Denidni *et al.* (2011) [65] introduced UWB DRA, excited by a CPW fed with a bevel-inspired patch. The DRA was placed on a Rogers's substrate (height of 1.64 mm and 24 × 15 × 6 mm^3). The antenna had two structure configurations with or without DR. When the structure was without DR, the antenna operated from 5.7 to 10 GHz, and it had a DR; then, the lower band shifted to 2.4 GHz and showed a better impedance matching. The optimized bandwidth of the antenna was obtained from 2.72 to 10.2 GHz. Using the CPW feed, this antenna achieved 49.4%, which was higher than the conventional feed. The optimal height of DR was achieved at 6 mm, and the length of DR was varied between 10 to 11 mm. Finally, it was observed that the proposed antenna was reported two notch bands from 3.35 to 3.8 GHz and 5.1 to 6.1 GHz and covered the frequency range from 3.1 to 10.6 GHz.

Yong-Feng Wang *et al.* (2013) [66] discussed a UWB planar monopole patch-based CDRA. This prototype was placed on a Rogers RO4350B substrate (thickness of 0.762 mm). This antenna was excited by the CPW feed, and another feed was used to excite DR by a slot that provided an NB. The measured results covered the frequency band from 3.05 - 11 GHz. In addition, both ports presented the same polarization and greater than 10 dB isolation within the operating range.

Idris messaoudene *et al.* (2016) [67] designed a solid RDRA to operate a range from 5.45 to 10.5 GHz, and this range was achieved by using the modified ground. The range of antenna was improved from 4 to 10.8 GHz by using a modified U-shaped DRA. Further, a metallic element was inserted inside the U-shaped DRA to improve the impedance bandwidth and cover frequency from 2.65 to 10.9 GHz with a peak gain of 6.2dB.

2.2.4 Inserted DRAs for UWB operation

Kenny Seungwoo Ryu *et al.* (2010) [68] presented a novel portable DRA and designed a narrow pulse sensor for breast cancer detection. The antenna provided broad radiation by a solid RDR mounted on the edge of a vertical ground plane. The total size of DRA was 18.3 × 14 × 5.08 mm^3, having a permittivity of 10.2, and placed on RT6002 substrate. A wide impedance bandwidth was obtained by a modified RDR shape, consisting of two dielectric fragments and converted into A-shape DRA. This antenna provided an impedance bandwidth of 84%, and the DR has two cuts and is fixed on the vertical ground plane. It was fitted to the edge, covering an impedance bandwidth of 93% (3.5 to 9.6 GHz).

Kenny Seungwoo Ryu *et al.* (2011) [69] presented a printed monopole-based DRA for UWB operations. The total size of the antenna was 15 × 33 × 5.08 mm^3. The inserted U-shaped DR was excited by a monopole-based CPW feed placed on the substrate. Three structures were followed: inserted DRA excited by microstrip feedline, planar DRA excited by CPW feed, and planar DRA excited by microstrip feedline. This antenna reported 10 dB bandwidth of 115% in the case of CPW and 109 % in the microstrip feedline. This antenna covered the frequency range from 3 to 11.5 GHz (simulated) and from 3.2 to 10.8 GHz (measured).

2.2.5 UWB DRA with band-rejection characteristics

Abas Sabouni *et al.* (2012) [70] designed an A-shaped DRA for UWB applications. This radiator element was excited by a transformer-type feedline and placed on the top of the substrate with a partial ground. Shorted stubs produced the notch features, and parasitic elements were attached to the feedline. Two notches were created within the UWB range. When two U-shaped parasitic elements were used with a length of 8.96 and 10.65 along the width of 1mm, this DRA reported a band from 3.5 to 10.5 GHz. The peak gain of the antenna was 5.46 dB except for a notch.

M. Abedian *et al.* (2013) [71] described a novel compact L-shaped DRA with a stopband characteristic for UWB applications. This antenna was made of printed monopole loaded with DR; it was placed on the substrate. An L-shaped parasitic strip was connected with the ground to achieve the notch characteristics. This antenna provided a wide impedance bandwidth of 120% (3.05 to 12.1 GHz) with a band rejection at $f_{notch} = 5.8$ GHz with 5.71 to 6.32 GHz. Using a modified metal sheet and fixed it under the DR. L-shaped strips and metallic sheets were used to improve impedance bandwidth and reported a gain of 4 dBi.

Yong Feng Wang *et al.* (2014) [72] presented a UWB RDRA with band notch characteristics. Two symmetric short circuit strips etched slots in the feeding patch are introduced to form a band-notched, and RDR hanged center on the metallic copper ground. The result demonstrated that both methods could form a notched band with appropriate positions using two symmetric strips attached in the opposite direction to the DR. The measured result showed that the DRA achieved UWB range from 3.6 to 12 GHz with a notched band from 5.1 to 6.0 GHz.

M. Abedian *et al.* (2015) [73] discussed dual band-notched DRA for UWB applications. The total antenna size was $12\times30\times6$ mm^3. This antenna was implemented with an arrangement of inserted DR excited by a U-shaped microstrip feedline. A stub was attached to a hollow center, an inverted T-shaped parasitic strip was fixed on the substrate, and a slot was cut in the ground to improve the bandwidth. This antenna provided an impedance bandwidth of 122% (3.03 to 12.52 GHz), with two-band rejection characteristics from 3.22 to 4.06 GHz and 4.84 to 5.96 GHz. As width varies from 0.8 to 1.4 mm, the notched frequency shifted down. The proposed antenna covered the frequency range from 3.45 to 10.9 GHz with an impedance bandwidth of 103.83%.

Upali Aparajita Dash *et al.* (2018) [74] presented a conical-shaped DRA with the size of $60 \times 60 \times 10$ mm^3. A circular patch having a cross-slot was printed on the top of the substrate, and a modified ground plane was used to obtain the UWB characteristics. In addition, the inverted conical DR was mounted on cross slot patches to achieve a high gain and wide impedance bandwidth of 152% (1.7 to 13.5 GHz). Notches were created from 3.0 to 3.75 GHz (Wi-Max) and 5.2 to 5.6 GHz (WLAN) to prevent interferences within the communication band. The measured gain of the antenna reported as 6 dBi except for two notches.

2.2.6 Stacked- segmented-composite DRA for UWB operation

Yuehe Ge *et al.* (2011) [75] designed an RDRA for UWB operations. Two half-size DRAs were presented with infinite PEC walls. Stacking with low and high permittivity was kept each other and placed on the infinite ground to achieve broad impedance bandwidth. The volume of DR was reduced by using a finite conducting wall fixed on the side of the DR layer. The impedance bandwidth of DRA was 110%.

Elham Erfani *et al.* (2016) [76] developed a hybrid DRA (HDRA) for UWB applications. The HDRA operated with three matching techniques such as step matching, composite dielectric, and dielectric shaping. These techniques were used for proper radiation performance. The dimensions of the groundsheet were 150 × 150 × 0.56 mm^3. Comparative bandwidth analysis of Antenna 1 and Antenna 2 was reported 158 % & 161%, respectively. The frequency range of Antenna 1 was 1.86 to 16.6 GHz, and Antenna 2 covered a frequency range from 1.67 to 15.63 GHz. The final antenna was achieved an impedance bandwidth up to 164% (VSWR < 2.5).

Poonam Kshirsagar *et al.* (2017) [77] described a two-segmented RDRA with a combination of half-sized RDRA composed with ε_r= 4.3 and ε_r= 9.2. A rectangular DGS was extracted from the infinite ground. The DGS position was observed at 0 °, 30 °, and 45 °. This antenna covered frequency from 2.9 to 11.6 GHz (120%) at an angle of 45 °. As the height of the patch increased, the bandwidth increased significantly. This antenna was reported to have a peak gain of 7.2 dBi and radiation efficiency of 95%.

Debatosh Guha *et al.* (2017) [78] explored a three-segment composite DRR. This DRR was adjusted with a vertical monopole. The proposed mushroom-shaped monopole DRA (MSMDRA) covered the UWB range and had a maximum group delay of 1.6 ns at 20 and 25 GHz. This antenna was achieved with an impedance bandwidth of 137 % (4.8 to 24.8 GHz) with a peak gain of 6.2 dBi.

Mian Shahzad Iqbal *et al*. (2018) [79] presented RDRA with dimensions of 12 × 8 × 15 mm^3 and an infinite ground plane (40 × 40 mm^2). The low permittivity insert (LPI) block was placed on the ground, and DR was fixed on the top of the LPI layer. Further, the antenna's performance was improved and provided an air gap (tetrahedron shaped) in DR to decrease the effective permittivity and vice versa to improve the performance of the proposed antenna. This antenna covered the frequency range from 3.11 to 11.6 GHz with an impedance bandwidth of 115%. It was found that the total power radiated in the upper hemisphere was approximately 90%, with significant > 10% power radiated in the lower hemisphere. The overall spectral efficiency of the antenna was increased to 52%.

Kedar Trivedi *et al.* (2018) [80] designed a triangular prism-shaped DRA for UWB applications. In this work, a low permittivity dielectric resonator material was sandwiched between two high permittivity DR materials to enhance bandwidth. The DRA was mounted on a square ground plane (L =140 mm) and excited by a coaxial feedline. The impedance bandwidth was achieved up to 120.9 %, which covered a range from 3.3 to 13.4 GHz.

Anand Sharma *et al.* (2018) [81] discussed a composite (alumina, Teflon) based DRA with the partial ground for UWB applications. The overall study was about unbalanced dumbbell-shaped CDRA & was due to the absence of metallic loss in CDRA. The optimal ground plane length was observed at 14.5 mm. The proposed antenna was operated from 3.23 to 10.98 GHz. The fidelity factor analyzed 86 % & 79 % for side-by-side & face-to-face arrangements. The average gain and radiation efficiency of the antenna were 3.1 dBi and 0.88, respectively. The antenna was achieved the UWB range by using a tilted annular-shaped printed line and modified DR structure.

Chemseddine Zebiri *et al.* (2019) [82] presented a compact CDRA having a defective ground for UWB applications. The structure was based on two CDRAs located heterogeneously concerning the center of the offset rectangular coupling aperture, considered three and four DRs. The impedance bandwidth of the antenna was 133% (3.6 to 18 GHz) with peak gain of 7.9 dBi.

Fan Wang *et al.* (2019) [83] presented a stacked DRA for UWB applications. It has a multilayer structure with different permittivity (6.15, 10.2, and 2.33) and different thicknesses. This single element antenna was converted into nine radiator elements and excited by a single feedline. This single antenna covered a range from 6 to 16 GHz with an impedance bandwidth of 90.9%. The newly modified structure of DRs was given the impedance bandwidth of 101.1% (5.42 to 16.5 GHz) with a peak gain of 6.2 dB.

2.2.7 UWB Reconfigurable DRA

Mehdi Abioghli *et al.* (2018) [83] designed a reconfigurable DRA having the dimensions of 40 × 40 × 7.3 mm^3. The geometry of the modified ground plane was constructed by joining two slots to an L-shaped stub. Finally, the DRA was designed with Rogers RT6010 (relative permittivity ε_r= 10.2) with T-shaped, mounted on an FR4 substrate. The reconfigurable concept was implemented by using the PIN diodes. 0.7 Volt was applied through the diode to bias them, and suitable impedance matching provided at 17 mm of ground length. The antenna reported rejecting switchable bands such as WiMAX (3.2 to 3.65 GHz), WLAN 5 GHz (4.8 to 6 GHz), and ITU 8 GHz (8 to 8.3 GHz), respectively.

Mehdi Abioghli *et al.* (2018) [84] implemented narrow band reconfigurable DRA for cognitive radio applications. The dual-port DR was placed on an FR4 substrate (permittivity of 4.4, thickness of 0.8 mm, tangent loss of 0.02, and dimension of 65 × 40 mm^2). The DR was made of Rogers RT6010LM with ε_r= 10.2. It was found that as the gap between the two metal strips increased, the resonant frequency shifted from 3 GHz into the upper frequency. The impedance bandwidth of the antenna achieved 80.34 % at the length of 17 mm. A wide tuning range was observed at VSWR < 2. To reduce mutual coupling, the space between the ground plane was chosen to be 10 mm. The radiation efficiency of the antenna was reported to be greater than 90%.

2.2.8 Super-shaped and other shaped DRAs for UWB operation

M. Simeoni *et al.* (2011) [85] presented a novel class of DRA, combining super-shaped contour and adopting plastic manufacturing material. Two different Super-shaped-DRA (S-DRA) were discussed. The first one was single feed S-DRA, and the second one was double feed based S-DRA. The single feed S-DRA antenna reported an operational bandwidth from 6 to 13 GHz. The maximum transmission coefficient was -12.7 dB. The double feed-based S-DRA covered the frequency range from 6 to 20 GHz. This antenna reported good 3 dB AR bandwidth.

Dileep Sankaranarayanan *et al*. (2016) [86] presented a unique and compact DRA-modified Koch snowflake-shaped for broadband usage. The radius and height of the CDRA were 2.68 cm and 1.5 cm. CDRA was fixed on top of the FR4 substrate, and a ground plane with the dimension of 10 cm × 10 cm was printed on the backside of the substrate. The designed geometry was used to enhance the performance of the antenna. It covered the frequency range from 4.7 to 12.4 GHz (90 % working bandwidth) with peak radiation efficiency and peak gain of 78 % & 8.76 dBi, respectively.

Dileep Sankaranarayanan *et al.* (2017) [87] discussed Bi Cone-shaped DRA, having Rogers TMM10i with a dielectric constant of 9.8. Comparative analysis between compact DRA, Bi-Cone DRA, and Bi-Cone DRA with triangular notches was discussed. The first geometry (conventional CDRA) provided an impedance bandwidth of 15%. The second geometry (Bi-cone DRA) provided an impedance bandwidth of 25.69%. The third geometry (BC DRA with triangular notches) provided an impedance bandwidth of 71%. The proposed antenna reported an impedance bandwidth of 93.1% (2.8 to 7.38 GHz).

Hailong Yang *et al.* (2018) [88] designed a slotted antenna for UWB operations. The size of the proposed antenna was 24 × 12 mm^2 and placed on top of the RT/Duroid 5880 substrate (thickness of 0.78 mm). The proposed antenna mainly consisted of a low pass stepped microstrip filter at the top of the dielectric substrate and two slots at the bottom. The measured results showed that the antenna covered the UWB frequency range from 3.1 to 11 GHz.

D. Sankaranarayanan *et al.* (2018) [89] presented a laterally fixed cylindrical DRA (LCDRA), excited by a coaxial probe and placed on the ground (4 × 4 cm^2). The permittivity of DR was 9.8 of Rogers TMM10i. Here, the authors showed three geometries: conventional CDRA, center-fed LCDRA, and offset-fed LCDRA, operating in the range of 4.8 to 5.9 GHz, 3.98 to 6.2 GHz, and 4.72 to 8.55 GHz, respectively. To improve bandwidth, similar triangular-shaped notches were extracted from LCDRA. The proposed antenna's frequency range was 6.5 to 10.1 GHz, with a peak gain of 7 dBi and radiation efficiency of 88 %.

Gagandeep Kaur *et al.* (2018) [90] presented UWB DRA, which worked as a RADAR imaging sensor for cancer detection applications. The RDRA having the modified ground plane, was excited by a stepped microstrip feed which covered the UWB frequency range from 4.3 to 12.6 GHz with an impedance bandwidth of 70.2%. The proposed RDRA reported a peak gain of 5.97 dB.

Piyush Sharma *et al.* (2019) [91] described turtle-shaped DRA for UWB applications. The dimension of the Roger RT/Duroid 5870 based substrate was 60 × 50 × 0.75 mm^3, and the modified ground plane with slotted DGS dimensions was 8 × 20 mm^2. The turtle-shaped DRA was operated at the frequency range of 3 to 10.9 GHz. Similarly, the bandwidth increased from 5.2 to 10.8 GHz by introducing a slab. The prototype covered the frequency range from 5.2 to 6.2 GHz, 7.2 to 9.6 GHz, and 11.6 to13.4 GHz. The radiation efficiency of the antenna was 70-90%.

Ahmed Zitouni *et al.* (2019) [92] discussed T-shaped compact DRA for UWB applications. The antenna consisted; T shaped DR excited by a stepped microstrip feedline, modified partial ground, and an inverted L-shaped stub. The DR was made of Rogers RT / Duroid 6010 with a dielectric constant of 10.2. The partial ground (25 × 11.5 mm^2) is fixed on the backside of the dielectric substrate. The proposed antenna covered the frequency range from 3.45 to 28 GHz.

F. Abushakra *et al.* (2020) [93] presented an E-shaped DRA for UWB applications, and it was excited by a coaxial probe using a trapezoidal strip to achieve the UWB range. The rectangular DR was transformed into an E-shaped DR, in which the quality factor decreases with increasing bandwidth. This antenna covered 3.85 to 13.3 GHz of the frequency band with an impedance bandwidth of 110%. The gain and radiation efficiency of the antenna reported as 7 dBi and 95%, respectively.

2.2.9 Circularly polarized DRA for UWB operation

Osama M. Haraz *et al.* (2010) [94] presented a circularly polarized (CP) DRA for UWB applications. It was made up of half-cylindrical DRA printed on the top of the substrate (permittivity=2.2), and the partial ground was printed on the bottom side of the substrate. The impedance bandwidth of the antenna was 90% (4 to 10.5 GHz). This novel design provided an AR bandwidth of 27% (5.3 to 7 GHz).

Piyali Chakraborty *et al.* (2021) [95] designed a dual circularly polarized DRA for UWB applications. This antenna was developed by placing a pair of symmetrically positioned DRs on a flat I-shaped monopole. The fundamental modes were excited at 3.8 and 6 GHz, and to generate CP, orthogonally placed DRs were added on top of the substrate. This antenna covered dual-band from 3.7 to 4.4 GHz (17.28%) and 5.8 to 6.2 GHz (11.56%) as 3-dB AR bandwidth, and reported an impedance bandwidth of 146.33% (2.1 to 13 GHz).

2.2.10 MIMO DRA for UWB operation

Mohammad Abedian *et al.* (2017) [96] designed WLAN band rejection MIMO DRA with dimensions of 29 × 29 × 5 mm^3. A ground stub was used to improve the isolation and impedance matching, and L-shaped strips were designed for band-notched function as WLAN systems from 5.15 to 5.85 GHz. Two L-shaped parasitic strips were used to create band rejections between 4.98 to 6.08 GHz. The performance results demonstrated that the proposed compact MIMO DRA provided consistent omnidirectional radiation patterns, a broadside impedance bandwidth of 106% with desired ECC of <0.16 within the limit.

M.M. Sani *et al.* (2020) [97] described a stair-shaped RDRA for UWB applications. Two radiators' element-based MIMO DR was designed with different permittivity (9.8 and 20) and used to enhance the antenna bandwidth. A diagonal stub and CPW feeding was used to improve the isolation by manipulating the current path. The UWB MIMO DRA covered 1.6 to 12.2 GHz of frequency (153.6% impedance bandwidth) with 4.72 dB of average gain.

CHAPTER 3

CYLINDRICAL AIR SPACED HIGH GAIN DIELECTRIC RESONATOR ANTENNA

This chapter presents the research work carried out to achieve the second objective of the proposed doctoral research work. A lot of work is available in the literature that focuses on the design of DRA antennas for specific wireless applications. Here a cylindrical air-spaced DRA is designed, simulated, fabricated, and tested for UWB applications. A hollow cylindrical structure is extracted from a Rectangular DRA (RDRA) with a modified ground to obtain UWB frequency response and high gain. So its simplicity in structure and ease of excitation, this type of RDRA has been an attractive choice for researchers in this field. Much work is available in the literature on the design and development of RDRAs for UWB applications to motivate them to choose a research path. The simulated and measured results are in good agreement, and an impedance bandwidth of 104.09% (3.28 to 10.4 GHz) along with a peak gain of 7.2 dB is obtained. This unlicensed band has a lot of applications in military, RADAR, satellite communication, wall image detection, and many other indoor wireless communication systems.

3.1 Introduction

A Rectangular DRA (RDRA) offers several attractive features, such as more degree of freedom in the parametric selection and easy design of optimization parameters. The design, simulation, parametric analysis, and experimental testing of RDRA with a quarter-wave transformer (QWT) feedline [98] [99] are presented in this section.

The proposed Cylindrical Air-Gap RDRA (CAGRDRA) in its geometry consists of a DR of alumina (electrical permittivity of 9.8, tan δ = 0.0001, thermal conductivity = 30 w/k/m, Rho = 3900 kg/m^3, heat capacity = 0.88 kj/k/kg, young's modulus = 370 KN/mm^2, Poisson ratio = 0.22), and it is placed on a dielectric substrate layer of a Rogers RT 5880 with an electrical permittivity of 2.2. The basic geometry of an RDRA is shown in Figure 3.1. By introducing the hollow or air-gap region in the existing geometry of DR, the effective dielectric constant and Q-factor of the DRA can be reduced, further improving the antenna's impedance bandwidth and gain [100] [101]. So its simplicity in structure and ease of excitation, this type of RDRA has been an attractive choice for researchers in this field. Much work is available in the literature on the design and development of RDRAs for UWB applications to motivate them to choose a research path.

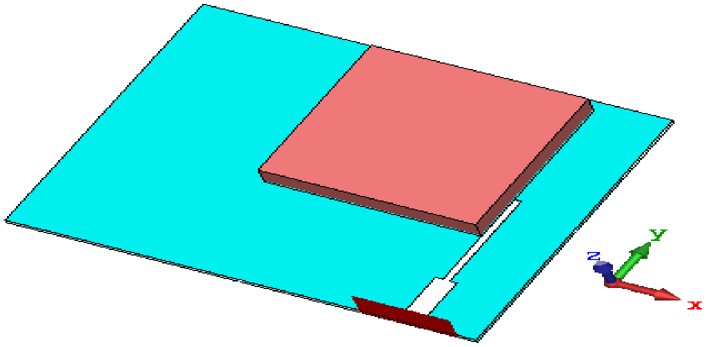

Figure 3.1: Perspective view of the solid RDRA

3.2 Proposed CAGRDRA Geometry

The designed antenna is a CAGRDRA (refer to Figure 3.2) for UWB applications. The proposed CAGRDRA takes the dimension of $50 \times 40 \times 4.835$ mm^3. This antenna geometry consists of an RDR, Rogers RT duroid substrate, modified ground, and QWT microstrip feedline. Inspired by the hollow or air gap-based techniques used in DRA to achieve the narrowband, wideband, and UWB applications [96]. A cylindrical-shaped DR with a radius of D1 = 6 mm and thickness = 4 mm is extracted from rectangular DR with base dimensions of $23 \times 23 \times 4$ mm^3. The QWT feeding method is used to excite the DR, and a modified ground structure is etched on the bottom side of the substrate. The DR used is Al_2O_3 material with a permittivity of $\varepsilon_{dr} = 9.8$, excited by a QWT type feedline printed on top of the substrate (Rogers RT 5880, $\varepsilon_s = 2.2$, hs = 0.8 mm), and the bottom layer of the substrate has a modified ground plane. The dimension of the QWT feedline is optimized with impedance matched to 50 ohms. Two metallic strips having the size of $M_2 \times M_1$ on the ground plane provide stable S_{11} of the antenna within the desired UWB range. The proposed CAGRDRA is designed and simulated on CST MWS V.16 software in a time domain solver with set of boundary conditions open (add space) in X, Y, and Z directions. All optimized parameters of DRA are labeled in Figure 3.2, and values are shown in Table 3.1.

Figure 3.2a shows the top view of the proposed CAGRDRA, Figure 3.2b shows the bottom view with its modified ground with metallic strips, and Figure 3.2c shows a 3-D view with an exciting port connected with the feedline.

Table 3.1: Optimized parameters of the proposed DRA

Parameters	L_l	L_w	L_{DR}	l_1	l_2	w_1	w_2
Values(mm)	50	40	23	7.7	14.4	2.2	0.75
Parameters	G_1	G_2	G_3	G_4	G_5	G_6	M_2/M_1
Values(mm)	48.5	23.4	28.5	21.5	14.2	9.2	15/10.5

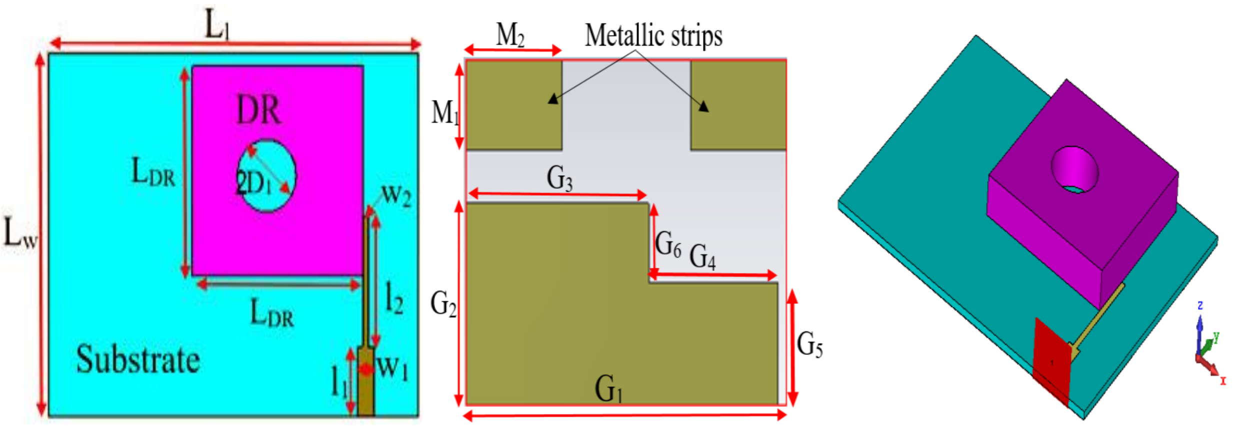

a b c

Figure 3.2: Simulated view of proposed CAGRDRA, a). Top view, b). Back view, c). 3-D view

3.3 Simulated Results

The hollow or air-gap-based DRA concept with the modified ground is designed, simulated, and validated using CST MWS V.16. First, the RDRA design is done using solver setting as hexahedral mesh type with an accuracy of -30 dB. Stimulation setting is done with all ports in source type using perfect boundary conditions as open (add space) in X, Y, and Z directions and selects all modes with normalizing to the fixed impedance of 50 Ω.

The voltage standing wave ratio (VSWR) result plotted in Fig. 3.3a shows a VSWR less than 2 with an impedance bandwidth of 7.1 GHz from 3.28 to 10.46 GHz. The 3D gain plot of the far-field is shown in Figures 3.3b-c, which reported a gain of 4.65 and 7 dB at 6 and 8 GHz, respectively. This antenna radiates energy in an omnidirectional pattern and shows how much energy it concentrates in a given direction compared to the total input power of the antenna.

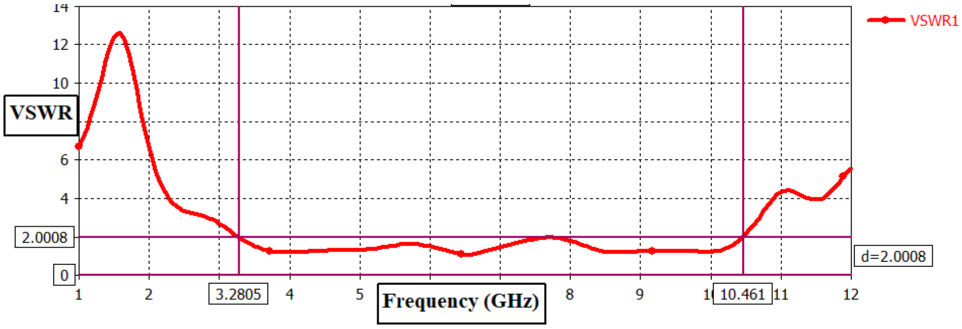

Figure 3.3 a: VSWR of the proposed antenna

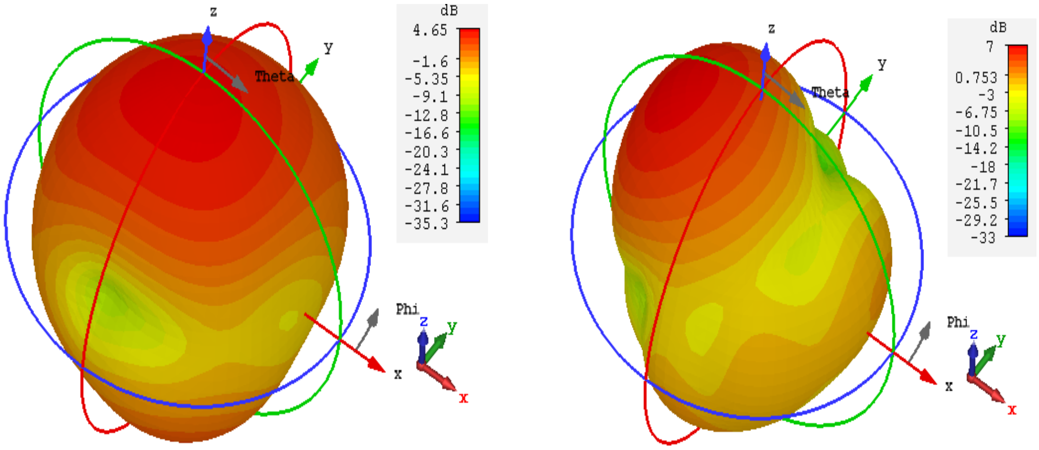

b c

Figure 3.3: 3-D Radiation pattern at; b). 6 GHz, c). 8 GHz

The following subsections discuss the evolution steps of the antenna along with simulated results, parametric sweep results of different parametric variations, surface current distribution and modes, and E-field distribution.

3.3.1 Antenna Evolution Steps

The six-step structures of antennas are shown in Figure 3.4 as Step_1, Step_2, Step_3, Step_4, Step_5, and Step_6, and the line graph in fig 3.5 represents S_{11} for each step by different colors like violet, yellow, green, blue, red, and black, respectively.

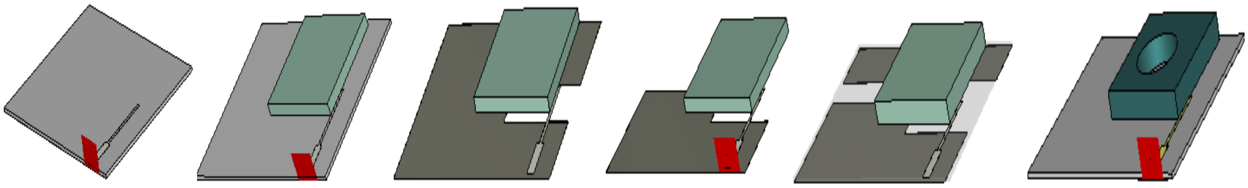

Step_1 Step_2 Step_3 Step_4 Step_5 Step_6

Figure 3.4: proposed Antenna Evolution Steps

All antennas can be used for wideband applications, except step_1 antenna, which has no working bandwidth without DR. Table 3.2 shows the frequency range and impedance bandwidth of all phases of antennas. The performance of the DRA stages is intended to obtain the final design and is given by the final antenna step_6 of the S_{11}, which covers the frequency band from 3.28 to 10.44 GHz, as shown in Figure 3.5.

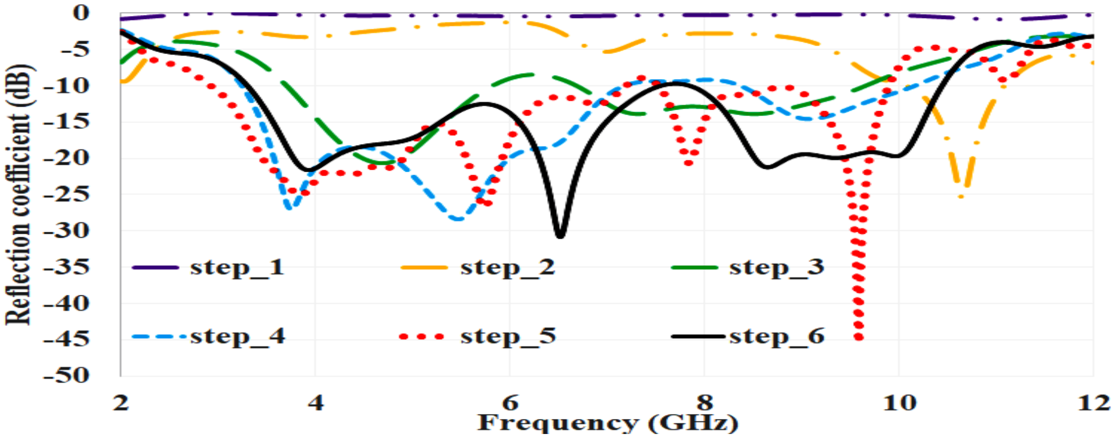

Figure 3.5: S_{11} of antenna evolution steps

Table 3.2: Antenna evolution steps covering the frequency range

Antenna steps	Frequency Range (GHz)	Impedance bandwidth (%)
Step_1	-	-
Step_2	9.8 to 11.1	12.44
Step_3	3.7 to 5.8; 6.6 to 9.6	44.21; 37.03
Step_4	3.3 to 7.1; 8.4 to 10.1	73.07; 18.37
Step_5	2.9 to 9.88	104.03
Step_6	3.28 to 10.48	104.09

3.3.2 Surface Current Distribution

The CAGRDRA was excited using the QWT microstrip feedline to see the distribution of energy at different frequencies. The current distribution of the metallic part of the antenna is presented in Figures 3.6a-d. The current rotation is observed from the surface current distribution on the ground plane and feedline. Also, it can be observed that the decoupling structure provided the maximum surface current on the edges of the rectangular decoupling slot at different frequencies [102]. At frequency 3.8 GHz, current directions on the x-axis are shown in Figure 3.6a. Figure 3.6b shows the current canceled with a single resonance path. Figures 3.6c and d show multiple places at which ground current is canceled and provided multiple resonance paths supporting higher-order modes. It can be seen that the peak current of 50.69, 39.12, 43.94, and 48.38 A/m, maintained in the ground and feedline at 3.8, 6.4, 8.8, and 10 GHz. Thereby allowing the CAGRDRA to exhibit widen bandwidth behavior.

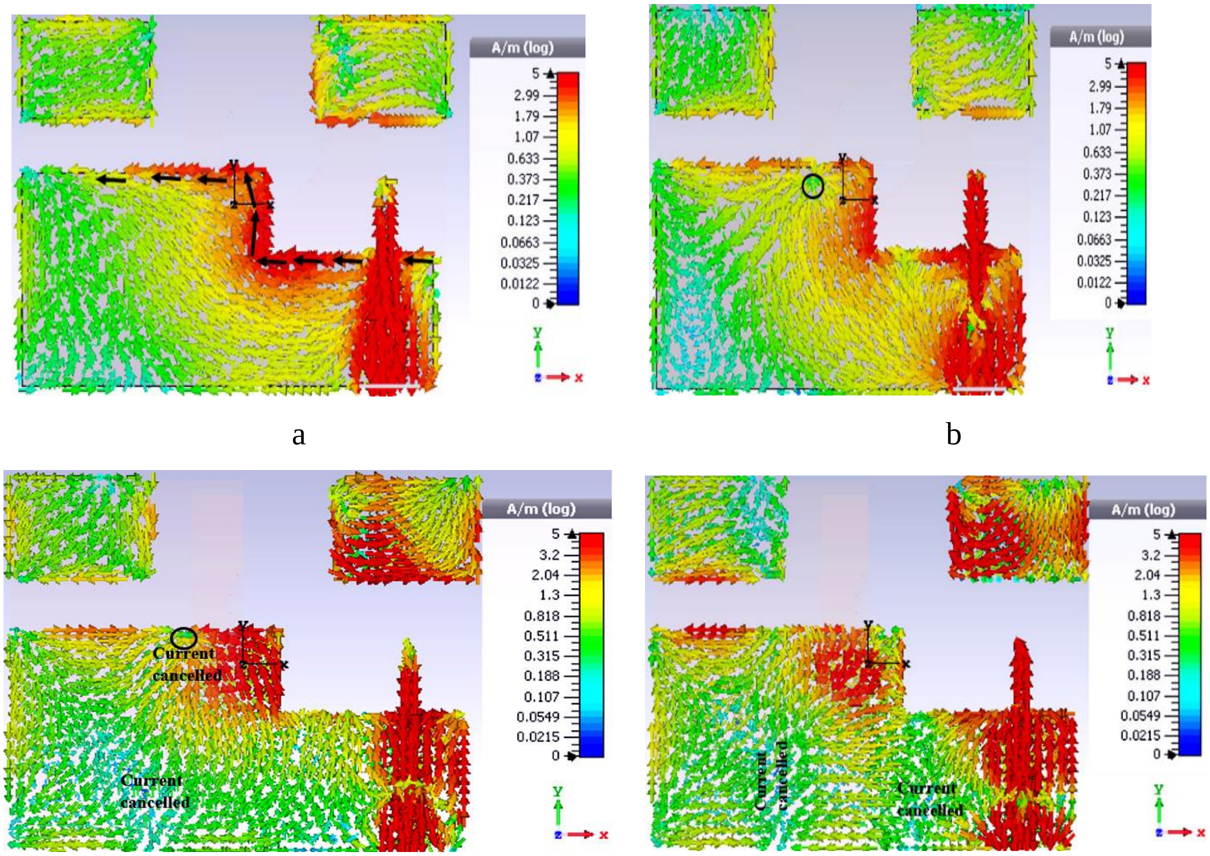

a b

c d

Figure 3.6: Surface current distribution at; a). 3.8 GHz, b). 6.4 GHz, c). 8.8 GHz, d). 10 GHz

3.3.3 Modes and E-field Distribution

Figure 3.7 shows the real and imaginary parts (red and blue color) of the input impedance of the proposed UWB CAGRDRA. It is observed from Figure 3.7 that there are four maximum peaks with real values of impedance and touching the same at zero values of imaginary impedance at the frequencies of 3.8, 6.4, 8.8, and 10 GHz in the desired frequency band. To get insight into the resonant modes at these four frequencies, the electric field distribution model is depicted in Figure 3.8.

The near fields depicted on the surface of DR at various resonant frequencies are given in Figure 3.8(a-i). Figures 3.7a-c show fundamental mode TE$_{11\delta}$ at 3.8 GHz with XY, XZ, and YZ planes, respectively. On the higher frequency side, it supports higher-order modes of TE$_{22\delta}$ at 6.4 GHz in Figure 3.8 d-f with XY, XZ, and YZ plane, respectively, TE$_{231}$ at 8.8 GHz in Figure 3.8 g-I with XY, XZ, and YZ plane, respectively, and TE$_{33\delta}$ at 10 GHz in Figure 3.8j-l with XY, XZ, and YZ plane, respectively. These modes support the widen impedance bandwidth of the proposed antenna.

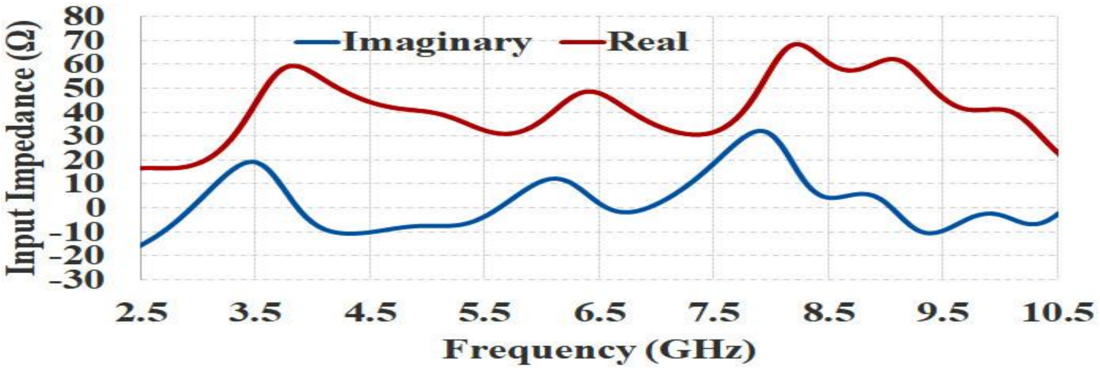

.

Figure 3.7: Simulated Antenna impedance plot

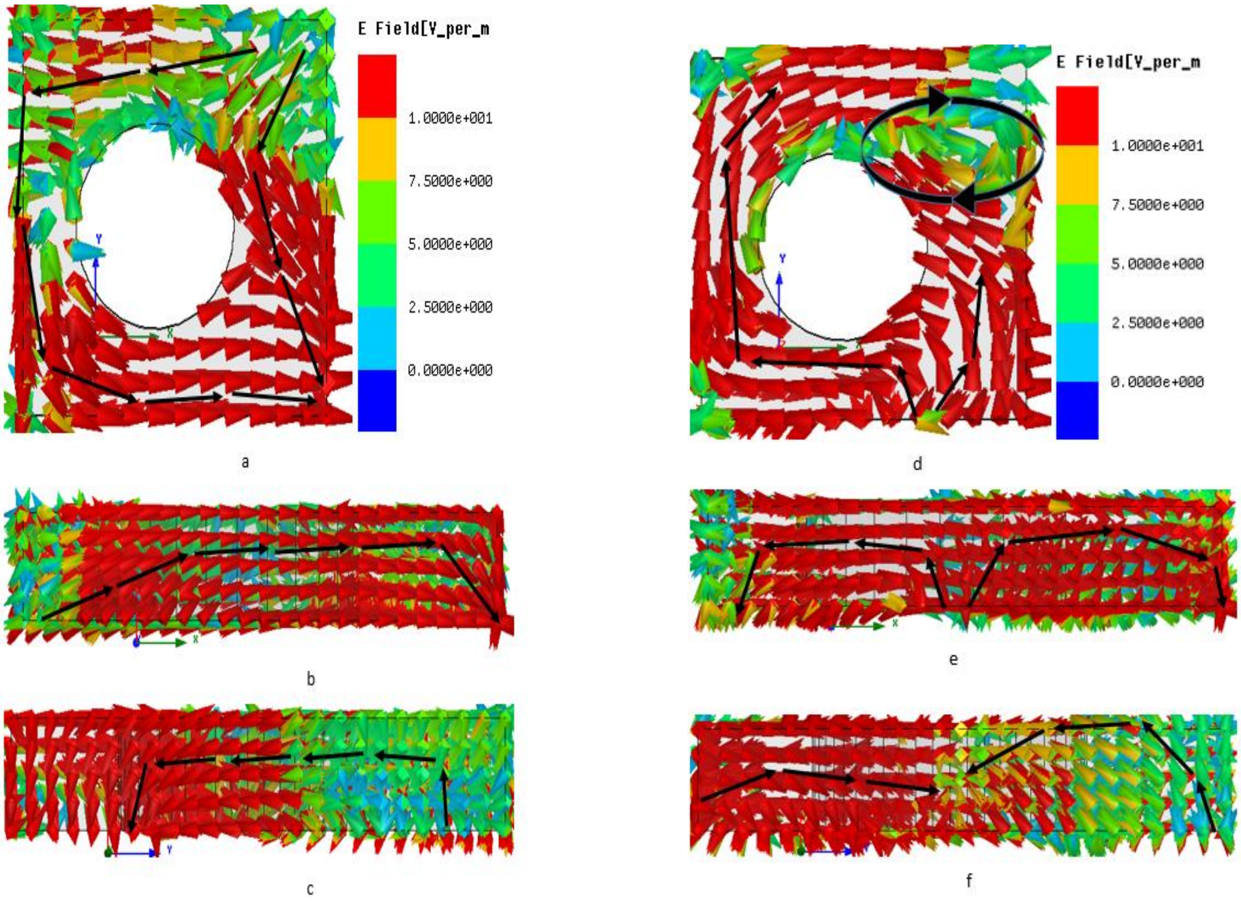

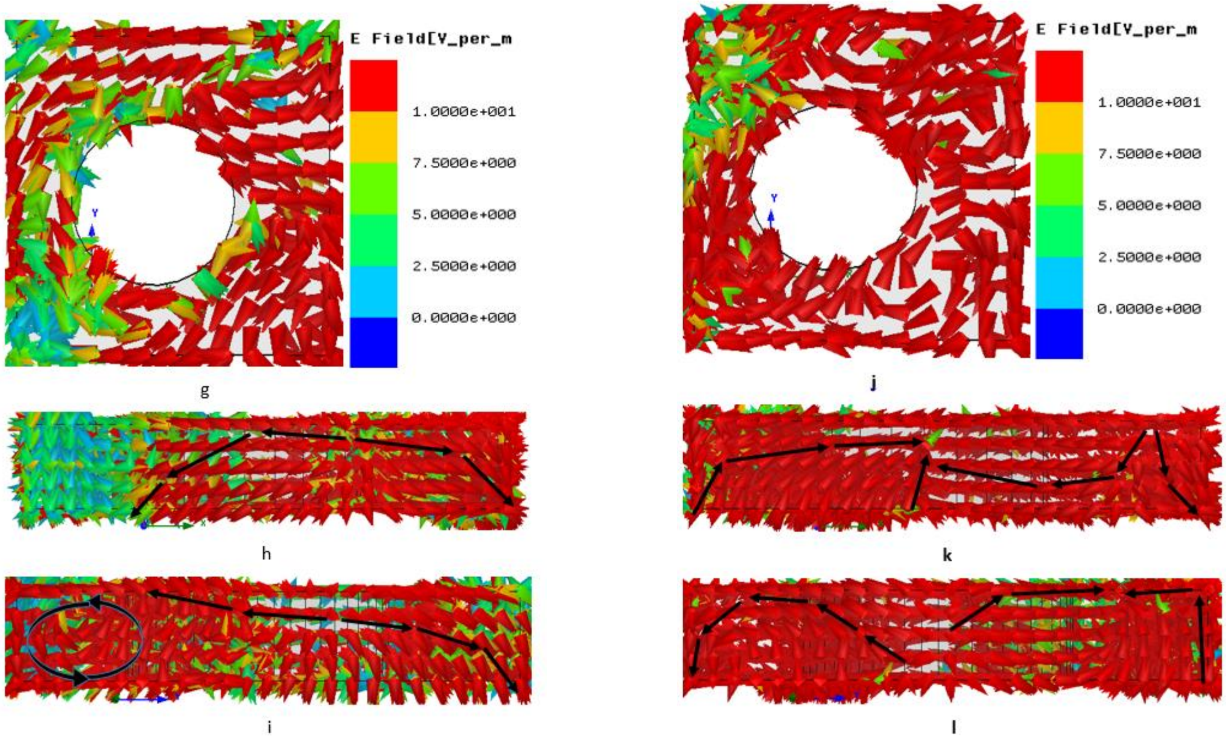

Figure 3.8: Near E-field distribution on hollow CAGRDRA at; a-c). 3.8 GHz ($TE_{11\delta}$ X-Y, X-Z, and Y-Z plane), d-f). 6.4 GHz ($TE_{22\delta}$), g-i). 8.8 GHz (TE_{231}), j-l). 10 GHz ($TE_{33\delta}$)

3.4 Parametric Analysis of the Proposed Antenna

The proposed CAGRDRA offers many parameters to the antenna engineers that can be optimized to achieve the best values of antenna performance, such as wideband or constant gain. Each appropriate parameter is varied in this section to observe its effect on antenna performance in terms of s_{11}, gain, and impedance matching.

3.4.1 Variations in the Outer Radius of Cylindrical Air-Gap

Figures 3.9a-b show the simulated parametric results of air-spaced DR in terms of hollow diameter D1. The hollow DR diameter directly affects the impedance bandwidth and gain of the antenna, as shown in Figure 3.9a-b. Here, the D1 is varied from 2 to 7mm, and observed that 6mm is the best value for VSWR and constant gain, as shown in Figure 3.9a and Figure 3.9b, respectively. If the hollow diameter increases, the antenna gain is improved, but the desired band starts shifting towards the higher frequency side.

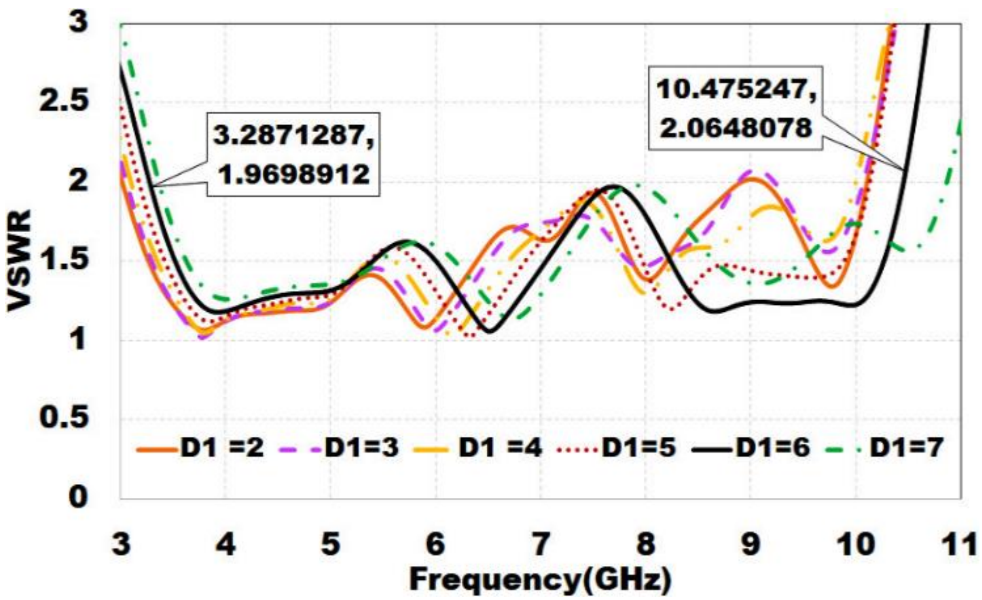

Figure 3.9 a: Effect of air-spaced cylindrical cut in RDRA (VSWR)

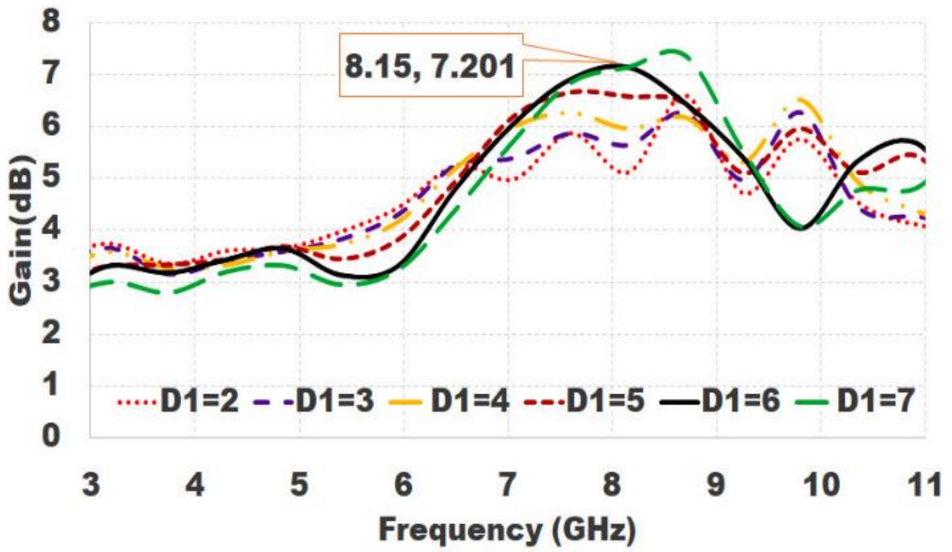

Figure 3.9 b: Effect of air-spaced cylindrical cut in RDRA (Gain)

3.4.2 Effect of Variation in the Height of Solid RDRA

In designing CAGRDA, the solid RDR height (hdr) was varied from 2mm to 7mm to understand its effect on the variation in the VSWR (≤2), as shown in Figure 3.10. Here, the RDR, chosen of $Al_2 0_3$ (alumina) material with a permittivity of 9.8 and heights of 0.5, 1, and 4mm easily available in the market. The best value of RDR is chosen as 4mm, for which a wide band VSWR is achieved.

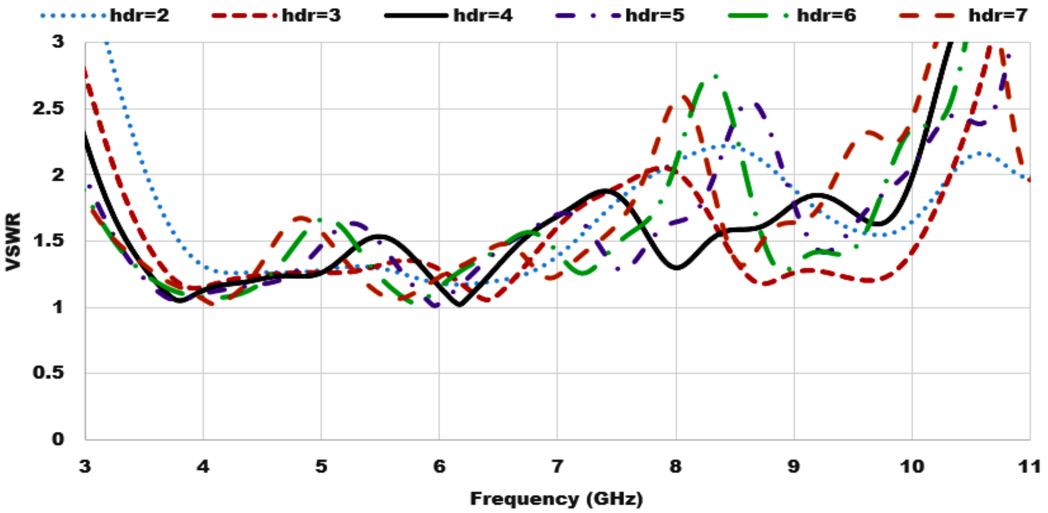

Figure 3.10: Effect of change in solid RDR height (VSWR)

3.4.3 Effect of Variation in the G6 and G2 of Modified Ground

The ground plane structure of the antenna is modified along the X and Y-axis to allow the effective fringing fields to radiate with better performance in terms of impedance bandwidth. To illustrate this, Figures 3.11a-b show the variation in the ground in terms of G2 and G6. The value of G6 is varied from 7.2 to 11.2 mm, and the results are shown in Figure 3.11a with different colours. It has the optimized value of G6 = 9.2 mm, for which the antenna gives a wider bandwidth.

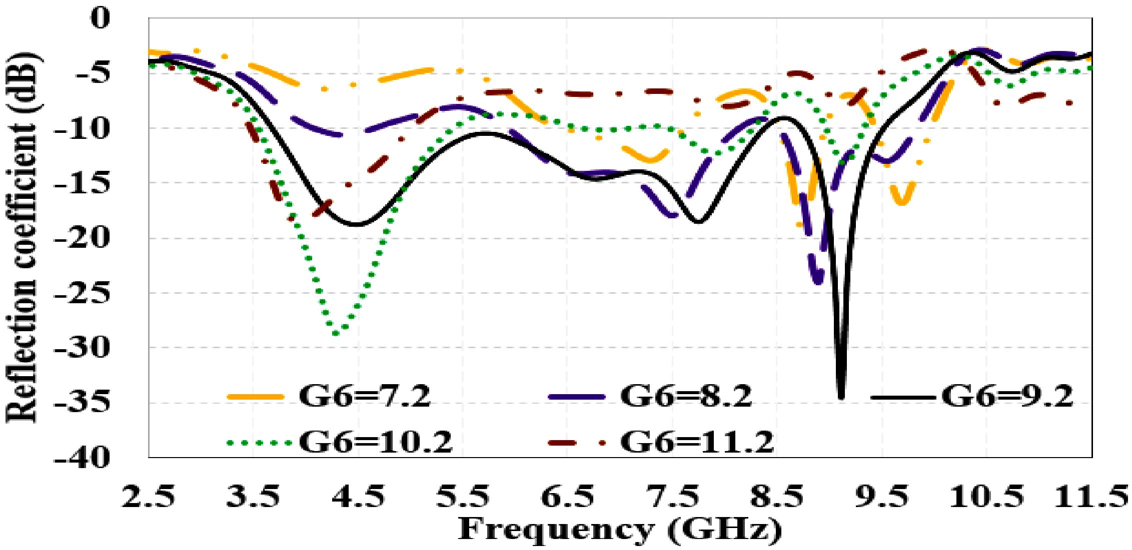

Figure 3.11 a: Effect of change in ground dimensions G6

The second ground parameter, G2, is varied from 21.4 to 39.4 mm, and the best value of 23.4mm is found. A line graph Figure 3.11b shows a UWB range from 3.28 to 10.44 GHz at this value.

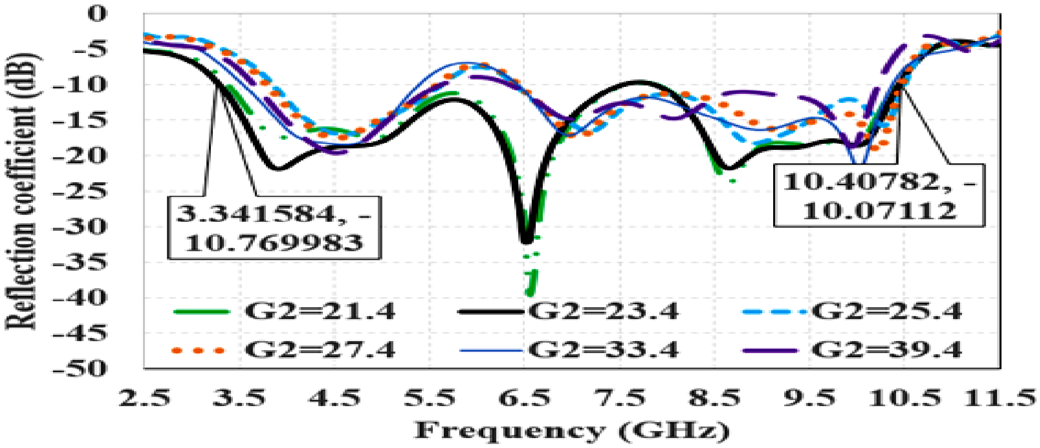

Figure 3.11 b: Effect of change in ground dimensionsG2

3.5 Air-Spaced RDRA Fabrication and Testing for Validation of Results

The proposed CAGRDRA was fabricated using wet etching techniques on Rogers RT duroid 5880 substrate with an electrical permittivity of 2.2, a thickness of 0.78 mm, and a tangent loss of 0.0009. Figure 3.12 a-b shows the snapshot of the front view with feedline and back view of the proposed antenna with assembled DRA on the top layer.

The fabricated antenna was tested on a vector network analyzer (Agilent E5071C) to validate antenna parameters results like S-parameters (dB), VSWR, etc. The results are shown in Figure 3.13 with S_{11} screenshot of VNA Figure 3.13 shows the comparison of simulated and measured results of the proposed antenna in terms of S_{11} (dB). These results are plotted in Microsoft excel for validating the two results (one from software and another from fabrication). The simulated and measured impedance bandwidth of antennas are 104.09% (3.28-10.4 GHz) and 103.86% (3.23-10.21 GHz). It makes the proposed CAGRDRA practically suitable for UWB applications of interest.

a b

Figure 3.12: Fabricated proposed CAGRDRA; a). Top view, b). Bottom view

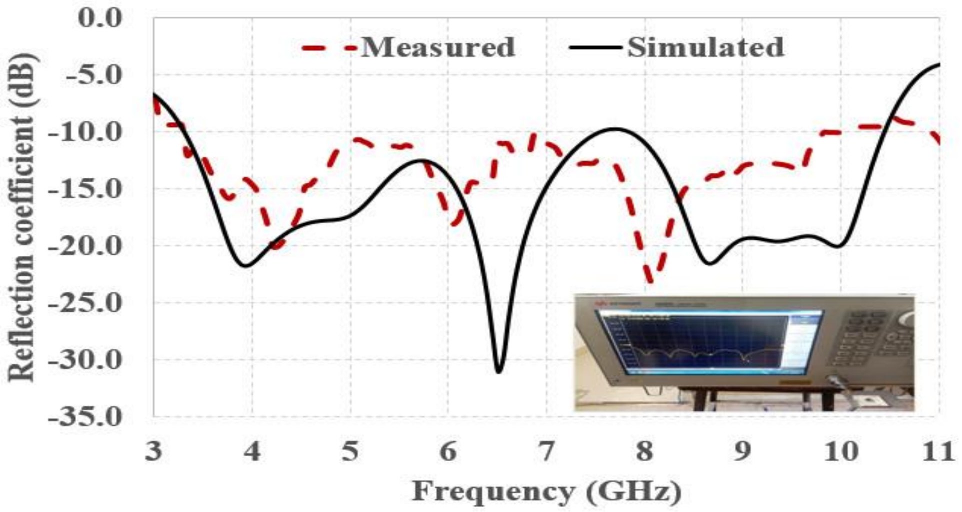

Figure 3.13: Simulated and measured S-parameter of proposed CAGRDRA

The proposed CAGRDRA was also tested to measure the radiation pattern and gain in an anechoic chamber with a handling frequency of 2 kHz to 18 GHz at IIT Roorkee (Uttarakhand). This chamber has a transmitting horn antenna with a gain of 12 dBi. It provides an ideal environment (no disturbances or eco) for the measurement of antenna gain using the Friss transmission equation [103]. Figure 3.14 shows the comparison plot of simulated and measured gain (black and red color) values. The simulated average radiation efficiency of the proposed antenna is approximately 88%, as shown in Figure 3.14 with dark blue color.

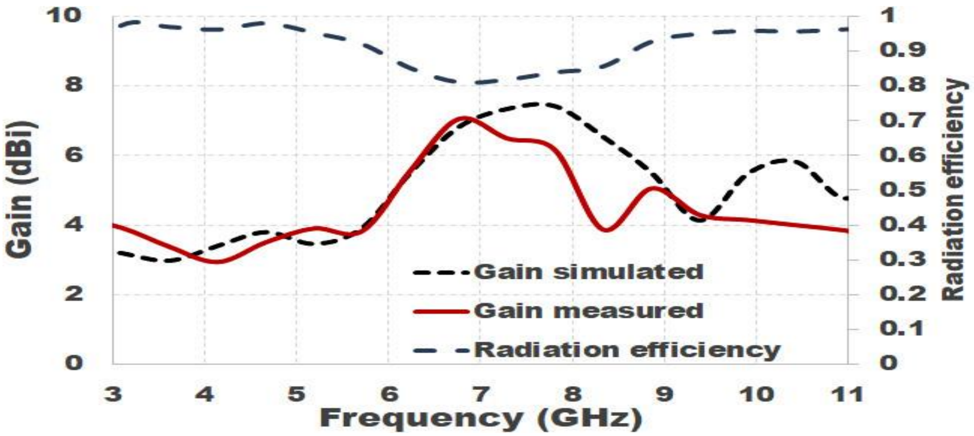

Figure 3.14: Measured and simulated gain and simulated radiation efficiency

Figure 3.15a-c describes the simulated and measured co and cross-polarization plots for the E plane of the antenna at three different frequencies, i.e., 4.1, 6.2, and 8.1 GHz. A few variations in simulated and measured E-plane radiation pattern plots can be seen because of some misalignment of DR during fabrication and between transmitter and receiver. The radiation patterns show that the proposed CAGRDRA radiates effectively in all directions within the desired UWB operation. Further, the cross-polarization (green and blue color) level is lesser than the co-polarization (Dark blue and red colors) level and shows an omnidirectional pattern in the E-plane.

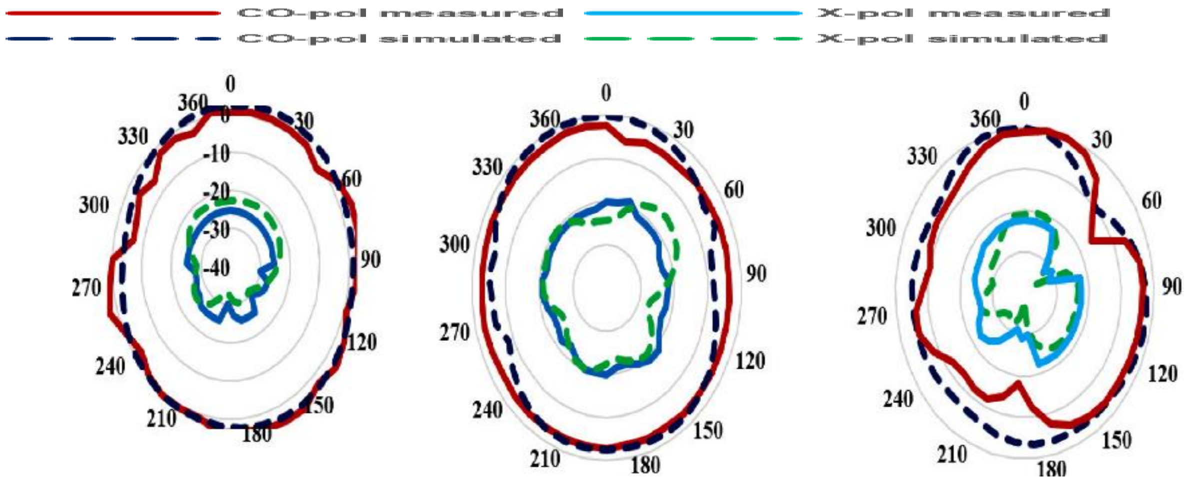

a b c

Figure 3.15: Simulated and measured co and X polarization pattern of antenna; a). 4.1 GHz, b). 6.2 GHz, c). 8.1 GHz

3.6 Conclusion

This chapter presents the research work carried out to achieve the 2nd objective of the proposed doctoral research work. The designed CAGRDRA antenna is made by cutting out alumina DR and pasting it on a rectangular DR sheet. This leads to UWB operation from 3.28 to 10.4 GHz and a peak gain of 7.2 dB. The impedance bandwidth of 104.09% (simulated) and 103.86% (measured) is achieved, allowing the proposed CAGRDRA to be suitable for UWB communication applications.

CHAPTER 4

ELLIPTICALLY AND CIRCULARLY POLARIZED DIELECTRIC RESONATOR ANTENNAS FOR UWB OPERATION

4.1 Introduction

Short-range communications face a rich scattering environment, which suffers from problems like fading due to multipath and power loss due to disintegrating conditions or mismatch in the orientation of transmitter and receiver antennas. To overcome these problems, the UWB communication systems require antennas with EP/CP properties that can receive signals along both horizontal and vertical planes.

Therefore this chapter presents two UWB DRAs with EP/CP properties to overcome polarization mismatch losses in short-range UWB communication systems. The research work presented in this chapter aims to achieve the second (partially) and third objectives of the proposed doctoral research work. Two DRAs, mainly an **OM-shaped DRA** excited by a P-type feedline having DGS in the ground structure with elliptical polarization characteristics and **stacked asymmetrical-shaped DRA** with circular polarization characteristics, are presented in this chapter.

There are number of techniques to achieve CP/EP polarization properties [104] [105]. Since the multi-feeding systems suffer from the disadvantage of being complex and leading to big antenna structures, the use of a modified shaped DR is the best way to achieve CP/EP characteristics with a single feeding method ., Therefore the two DRAs presented in this chapter achieve EP/CP properties typically with a single feeding mechanism only. The proposed DRAs have been designed, simulated and fabricated, and tested for validation of their radiation properties. This chapter is organized as follows: Section 4.2 presents an OM-shaped DRA for UWB operations with high gain and EP properties. Likewise, Section 4.3 presents the design and development of asymmetrical shaped DRA with a modified ground plane for existing CP properties within the UWB range of its operation.

4.2 Design and Development of an Ultra Wideband OM-Shaped DRA

This section presents the design and development of an OM-shaped DRA, designed and fabricated on the Rogers RT duroid 5880 substrate with a block of OM-shaped Alumina DR placed over it. The proposed ‘OM’-shaped DRA is excited by a P-type feedline for UWB operation. The proposed antenna provides an EP behavior covering 6 to 11.1 GHz and impedance bandwidth of 8.3 GHz with a peak gain of 7.66 dB.

4.2.1 Antenna Geometry and Design

The proposed dual-polarized OM-Shaped DRA is designed and simulated using CST MWS V.16 software. This antenna is made of Alumina DR (ε_{DR} = 9.8, tan δ = 0.0001, thermal conductivity = 30 w/k/m, Rho = 3900 kg/m^3, heat capacity = 0.88 kj/k/kg, young's modulus = 370 KN/mm^2, Poisson ratio = 0.22), and it is placed on a Rogers 5880 RT duroid based substrate (ε_r = 2.2, height = 0.8mm, tan δ = 0.0009). The geometry of the proposed antenna is shown in Figures 4.1(a-c) with top, back, and perspective views, respectively. Figure 4.1a shows the top view of the antenna geometry as an inverted OM-shaped DR (in red) and P-type feedline (in grey). The DR is excited by an inverted P-type transformer-based microstrip feedline having a length (lf1 +lf2) of 22.5 mm, offering an input impedance of 50 **Ω**. A conformal metallic strip (length = 5.7mm, height = 4mm) is connected between the edge of the feedline and the DR, it is shown in Figure 4.1c. This type of feeding allows better coupling of EM fields to the DRA. The bottom of the Rogers substrate is a reduced copper ground layer from which three slots are etched to make it a reduced DGS, shown in Figure 4.1a. This DGS improves the antenna's impedance bandwidth and impedance matching within the desired UWB of operation [106] [107]. A DGS improves the current distribution on the antenna ground layer, thereby allowing it to resonate at the same frequencies as the antenna and hence provides an improved bandwidth [102]. The effect of etching out these slots in the ground layer is shown in Figure 4.4b using the S11 graph. It can be observed from figure 4.4 that the S_{11} without DR with the full ground has no bandwidth (red color), in the second case, DR placed on top of the substrate with full ground covers 8.6 to 12 GHz (blue color). It does not cover the UWB range, so DGS slot 1 was extracted from the ground. The DGS is helped to shift the frequency band towards the lower side and improving the impedance bandwidth, and slot 2&3 are used for improving the impedance matching within the UWB (3.1 to 11.4 GHz) operations. In addition to the DGS, the ground layer is also a reduced ground structure to reduce the antenna size.

The proposed OM-shaped DRA is labeled in figure 4.1a-c, and its optimized parametric values are also mentioned in table 4.1. The next section of this chapter explains the DRA design process steps, and the equations are used to obtain the optimized DRA parameters.

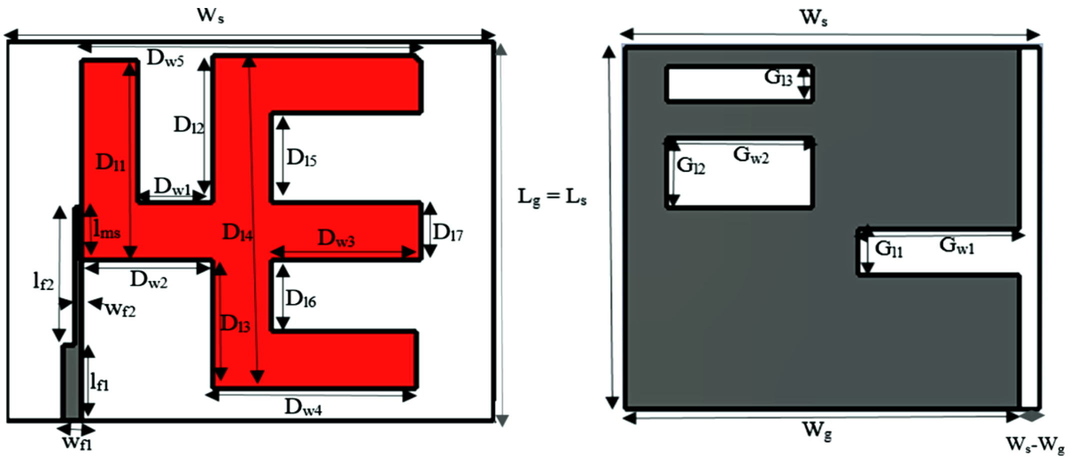

a b

Figure 4.1: Proposed 'OM' Shaped DRA; a). Top view, b). Back view

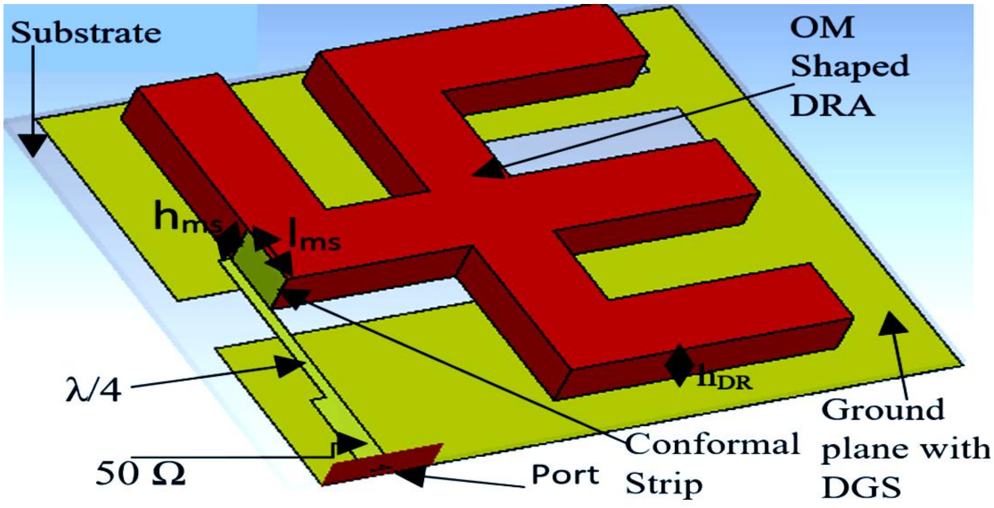

Figure 4.1c: Perspective view of proposed 'OM' Shaped DRA

Table 4.1: Detailed optimized dimensions of the 'OM' shaped DRA

Parameter	Dimensions (mm)	Parameter	Dimensions (mm)
D_{l1}	21	G_{l1}	5.2
D_{l2}	15	G_{l2}	7
D_{l3}	14	G_{l3}	5
D_{l4}	35	G_{w1}	19.5
D_{l5}	9.4	G_{w2}	17.5
D_{l6}	7.6	$L_g = L_s$	40
D_{l7}	6	W_s	50
D_{w1}	7.6	W_g	47.5

D_{w2}	13.6	l_{f1}	7.7
D_{w3}	15.4	l_{f2}	14.8
D_{w4}	21.4	w_{f1}	2
D_{w5}	35	w_{f2}	1
h_{DR}	4	h_s	0.8
lms	5.7	hms	4

4.2.2 Design Procedure

The proposed DRA is designed and simulated using CST MWS V.16 software with mesh settings of 10 cells per lambda and open boundary conditions using the time domain solver. The DRA design procedure starts with selecting the Alumina sheet as the dielectric resonator for the antenna structure by comparing the antenna performance on three different DR materials as shown in Figures 4.2 & 4.3 (with ε_{DR} = 9.8, 15 & 30 with black, blue & red colors) respectively. The next step after selecting DR material is the selection of the base substrate and its dimensions for antenna designing. The size of the base substrate of Rogers RT Duroid 5880 with properties (electrical permittivity of 2.2, Tan δ = 0.0009, thermal conductivity = 0.2 w/k/m) is set as 40mm × 50mm × 0.8mm. Thus a rectangular sheet of dimensions 35 × 35 mm^2 of commercially available Alumina (Al_20_3) is cut into the final optimized OM-shaped DR that is pasted on Rogers's substrate. The design equations (4.1 to 4.5) mentioned in this section are followed for designing the proposed OM-shaped UWB DRA.

The dimensions of the DR are calculated according to the resonant frequency of operation given by equation 4.1 [108]. Using l = m = n = 1 for TE_{111} mode, ε_{DR} = 9.8, D_{l4}= 35mm, D_{w5} = 35mm, h_{DR} = 4mm as the length, width and height of 'OM' shaped DR respectively (cube of Alumina with dimensions 35mm × 35mm × 4mm) in equation 4.1, K_x , K_y and K_z are found as 89.75, 89.75 and 324.88 respectively.

$$f_{TE_{lnm}} = \frac{v}{2\pi\sqrt{\varepsilon_r}}\sqrt{k_x^2+k_y^2+k_z^2} \tag{4.1}$$

Here k_x, k_y, k_z are the wave propagation numbers along x, y, z directions.

$$k_x = \frac{l\pi}{D_{l4}},\ k_y = \frac{n\pi}{D_{w5}},\ k_z = \frac{m\pi}{2h_{DR}} \tag{4.2}$$

$$(k_x)^2 + (k_y)^2 + (k_z)^2 = \varepsilon_{DR}\,(k_0)^2 \tag{4.3}$$

$$k_z \tan\left(\frac{k_z h_{DR}}{2}\right)=\sqrt{(\varepsilon_{DR}-1)k_0^2-k_z^2} \qquad (4.4)$$

$$k_0=\frac{2\pi}{\lambda_0}=\frac{2\pi f_0}{v} \qquad (4.5)$$

Using these values in equation 2 with V = 3 $\times 10^8$ m/sec as the velocity of light and ε_r = 9.8 as the dielectric constant of DR, h_{DR} = 4mm, the resonant frequency of 5.2GHz is calculated for the cubical DR (35mm × 35mm × 4mm). Using the values of K_x , $K_{y,}$ and K_z in equation 4.1, K_0 is found to as 110.85.

The next step that follows in the optimization of the proposed DRA design is to reduce the ground structure and cut out slots from it to make it a DGS Figure 4.4 (a). Since Ground is crucial for getting desired impedance bandwidth of UWB operation, it is changed to the reduced ground as the antenna size is comparatively reduced with this technique. Figure 4.4(b) shows the S_{11} plot of the proposed structure without DR with full ground layer, DR with full ground layer, and DR with DGS slots 1 to 3 cut from it, respectively. The DGS helps in shifting the frequency band towards the lower side while improving the impedance bandwidth of the excited UWB (3.1 to 11.4 GHz) of the proposed DRA. This is mainly because the three slots in the ground produce current loops that excite the lower frequencies apart from the frequencies at which the DRA already shows resonance. This ground structure is used with all three intermediate DRA geometries to produce the final DRA 4 design.

The intermediate design Steps followed while optimizing the proposed OM-shaped DR geometry, which offers improved gain and dual-polarization properties, are mentioned in the next subsection.

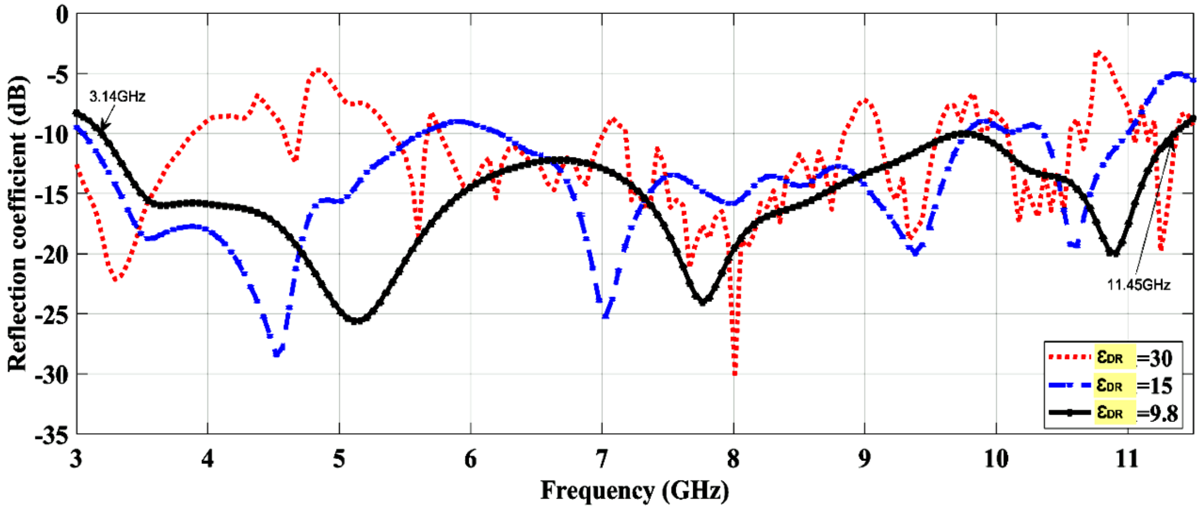

Figure 4.2: Comparison of S_{11} Plot for three different DR materials

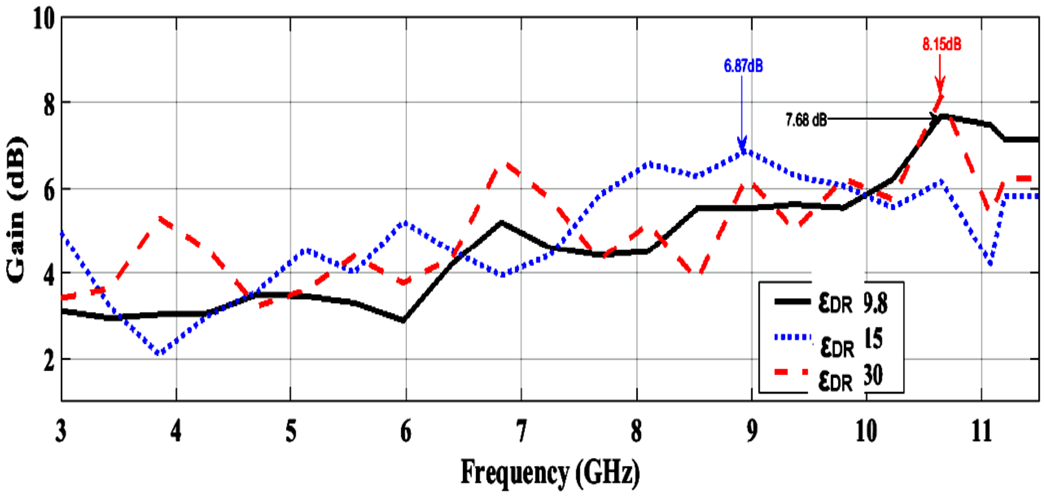

Figure 4.3: Comparison of Gain parameter Plot for three different DR materials

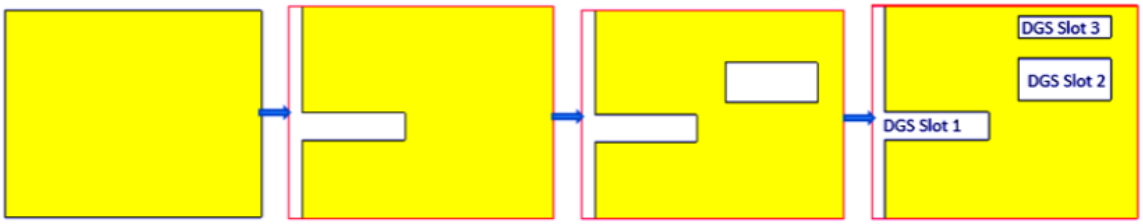

Figure 4.4 (a): Evolution steps of DRA ground layer

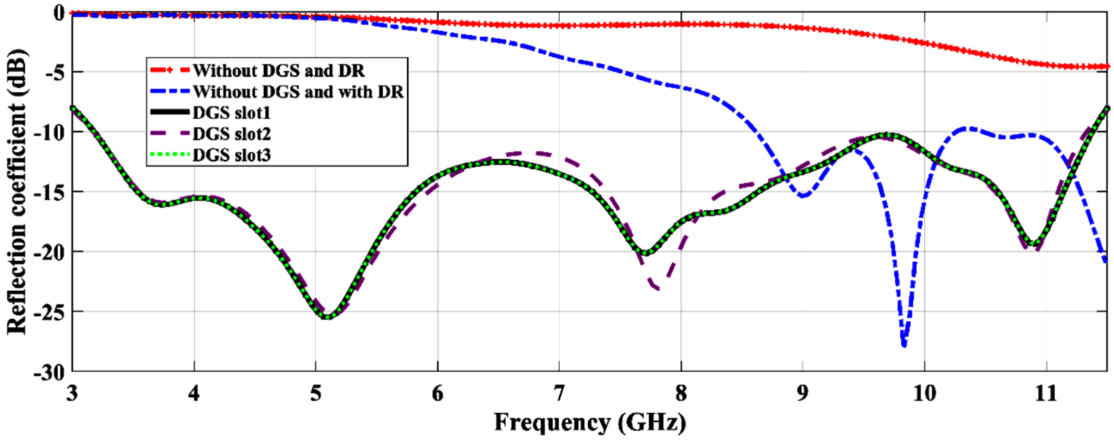

Figure 4.4(b): S_{11} plot of the proposed DRA with and without DGS & DR

OM Shaped DRA Evolution Steps: In ascending order, the antennas' four intermediate design step structures are shown in Figure 4.5 as DRA1, DRA2, DRA3, and DRA4 followed while designing the optimized UWB dual-polarized DRA4.

- The dimension of DRA1 takes 35 × 17.5 × 4 mm^3, has ground with three DGS, and is excited by a QWT feedline figure 4.5(b). The design equations 4.1 to 4.5 mentioned in this section are followed for designing the proposed OM-shaped UWB DRA.

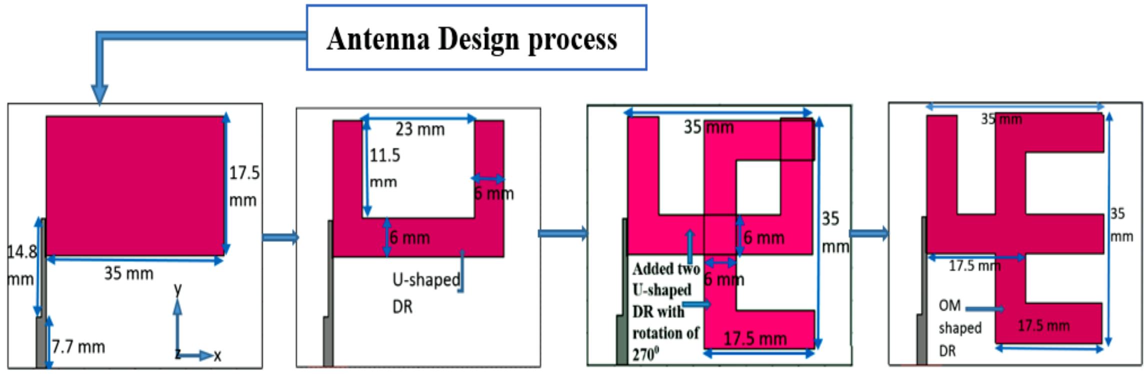

DRA1 DRA2 DRA3 DRA4

Figure 4.5: Intermediate design steps of UWB 'OM' shaped DR

Figure 4.5(b) shows the DRA ground structures for DRA 1, DRA2, DRA3, and DRA4, respectively.

The simulated S-parameter response for the DRA1 structure is shown in figure 4.6a as blue color. Multiple resonances are excited by the cubical DR in DRA1 geometry at 5 GHz, 7 GHz, 8 GHz, 9 GHz, and 10.3GHz because the DR excites more than one operating mode, including the fundamental mode. This DR is fed with a P-type transformer feedline that offers an input impedance of 50 ohms to the proposed antenna. The Peak gain reported for this geometry could be seen in Figure 4.6b as 6.09dB at 11GHz. Figure 4.6c (blue colour) shows that the DRA1 is linearly polarized.

- The dimensions of the solid rectangle were taken to be 23 × 11.5 × 4 mm, and a smaller rectangular DR was extracted from DRA1 to obtain DRA2 as a U-shaped DRA. The resultant S_{11} plot for DRA2 geometry is shown in red color in figure 4.6a. A UWB from 3.1 to 11.1 GHz is excited by the U-shaped DRA 2 but has poor impedance matching from 7 to 11.3GHz. Figure 4.6b shows an improved peak gain (by 0.38dB) for this geometry as 6.38dB at a frequency of 9.8GHz. Figure 4.6c shows the (Red curve) axial ratio bandwidth plot for this geometry. The DRA2 geometry is elliptically polarized and covers a frequency band from 5.9 to 9.2 GHz (AR< 10dB). Since the impedance matching for the frequency band from 7 to 11.1GHz is not much below the desired -10dB level in the aforementioned

DRA2 geometry, an improvement in peak gain is also expected for short-range UWB applications, so DRA 3 geometry is proposed.

- The DRA 3 geometry is formed by adding the two U-shaped DRs of which one is the U-shaped DRA 2, and the other one is the DRA2 rotated by 270^0 as shown in figure 4.5(a). The peak gain for DRA 3 geometry is further improved (by 0.89dB) and is reported as 7.27dB at 10.5GHz, as shown with a green colored graph in figure 4.6(b). The green curve in figure 4.6a shows the S_{11} parameter plot of DRA3. Since a notched UWB behaviour (3.1 to 11.1 GHz) with a notched band from 9.3 to 10GHz and an elliptically polarized behaviour from 6.3 to 9.2GHz and 10.1 to 11.5 GHz is obtained for DRA3 geometry, DRA4 geometry is proposed to cover the entire UWB from 3.12 to 11.4 GHz
- The final proposed DRA4 geometry is formed by cutting out the loop part from DRA 3 (based upon the perturbation theory of creating air slots in the proposed DR structure) in figure 4.5 to develop the final OM-shaped DRA4. The black color curve in figure 4.6a shows the S_{11} plot excited by the DRA 4 geometry. An excited UWB from 3.1 to 11.4 GHz is observed for the DRA4 geometry. Figure 4.6b shows that the simulated peak gain for the DRA4 geometry is the highest among all the proposed DRA geometries. This DRA4 geometry generates both the horizontal and vertical components of the electric field because of its shape, and hence this geometry shows dual (elliptical) polarization properties for a frequency band from 6 to 11.1GHz, as shown in figure 4.6c. Since this DRA4 geometry shows the best results with the covered UWB range (3.1 to 11.4 GHz), the simulated peak gain of 7.66dB, and axial ratio bandwidth of 5.1 GHz, it is the selected final geometry for the proposed UWB DRA.

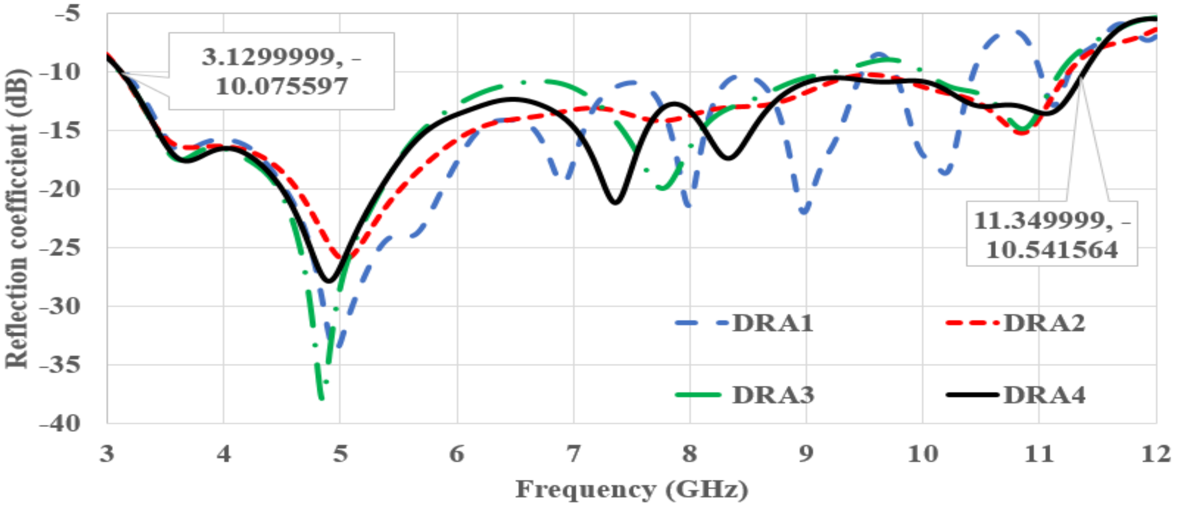

Figure 4.6a: S_{11} plot of the Intermediate design steps of the optimized ‘OM’ shaped DR

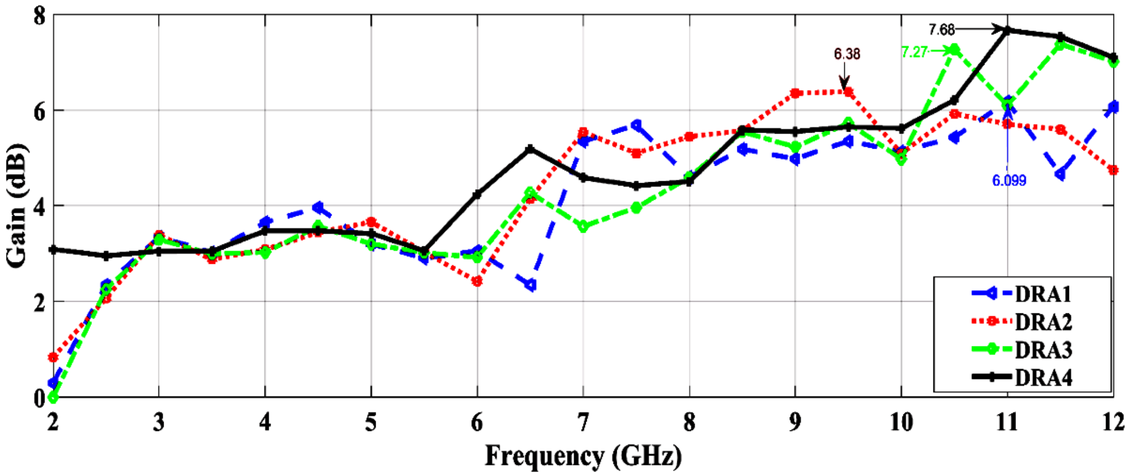

Figure 4.6b: Broadband gain plot for four DRA geometries

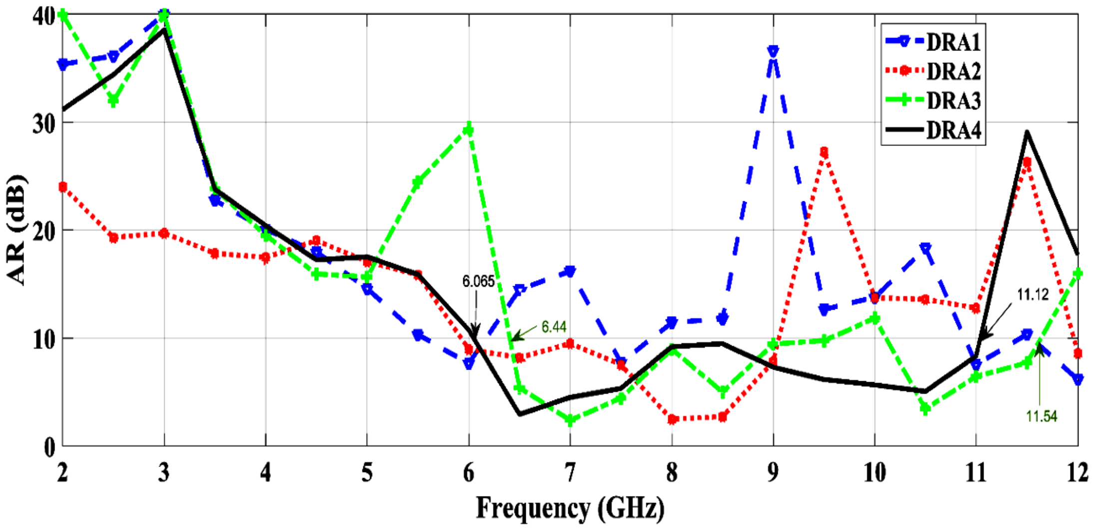

Figure 4.6c: Axial ratio plot for the four DRA geometries

4.2.3 Validation of Modes

A rectangular DRA exhibits fundamental and higher-order in terms of TE, TM, and HEM modes [109] [108]. The importance of the modes is to merge them to improve the impedance bandwidth. Orthogonal modes are used for achieving the polarization diversity in DRAs. Figure 4.7 shows the real and imaginary parts of the proposed DRA impedance matching plot. The peaks of the real impedance are taken here, and zero for the imaginary impedance plot, according to this impedance matching plot. For selecting modes, the input impedance matching values of modified OM-shaped DRA is generally at 4.8, 7.2, 8.35, and 10.9 GHz. The fundamental/dominant mode, TE_{111} for the proposed optimized OM-shaped DRA, exists at 4.8 GHz, which is very near to the theoretically calculated frequency of the fundamental mode of 5.2GHz for the cubical DR (as mentioned in section). The other higher-order modes that exist during DRA operation radiating an ultra-wideband are the TE_{211} and TE_{221} at resonant frequencies of 6.5 and 8.35 GHz, respectively. Since higher-order modes correspond to higher resonant frequencies within the frequency band. Merging the modes gives respective widened bandwidth, and hence the desired ultra-wideband performance from the proposed DRA is achieved [110] [111].

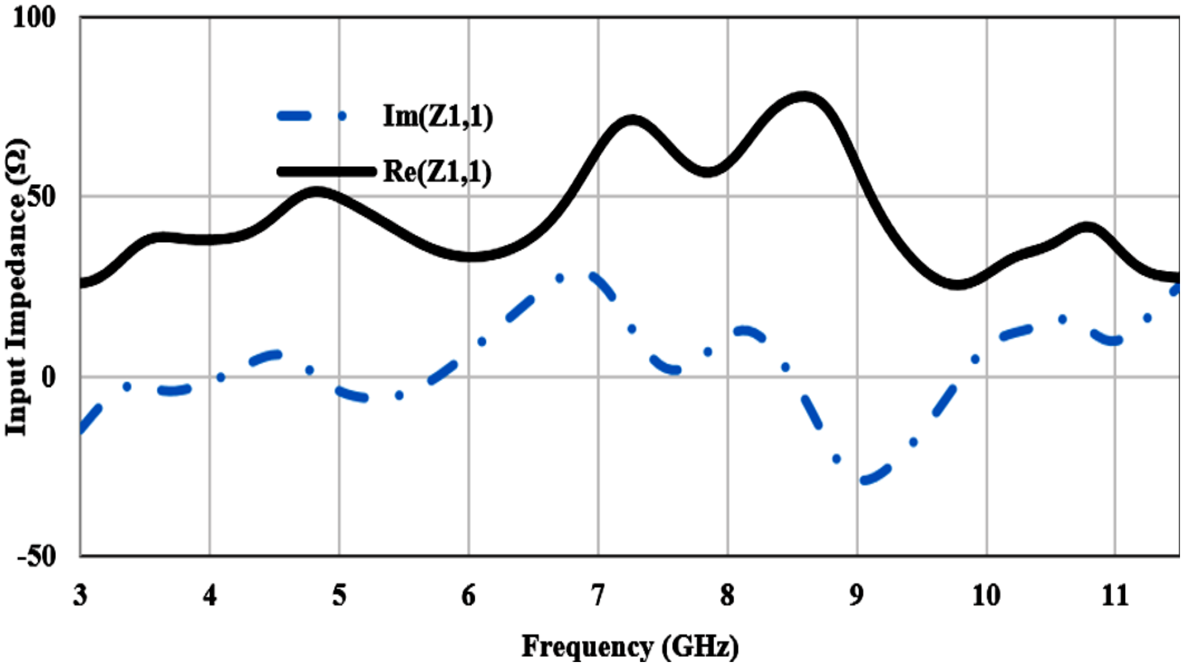

Figure 4.7: Input impedance plot (simulated) real and imaginary

Figures 4.8a- f show the simulated E-field distribution at a reference phase of 0 degrees on the DRA surface at the modes of TE_{111}, TE_{211}, TE_{221} at resonant frequencies of 4.8 GHz, 6.5 GHz, 8.35 GHz, respectively [112]. The resonant frequency of the fundamental mode is also calculated by equations (4.1 to 4.5) and is found to be almost the same. It is observed from figures 4.8a-b that a fundamental mode of TE_{111} exists on the XY plane and YZ planes of DRA, respectively, at 4.8GHz with a maximum E field strength of 12433V/m on the DR surface. The H field distribution on the DRA surface is also shown in figure 4.8a-b, which shows the existence of TE_{111} mode at 4.8GHz. Figures 4.8c-d show the E and H field distribution on the XY and YZ planes of the OM-shaped DRA at 6.5GHz, indicating the existence of TE_{211} mode with a maximum E field magnitude of 13873 V/m. Figure 4.8e-f shows the E and H field distribution on the XY and YZ planes of the OM-shaped DRA at 8.35 GHz depicting the existence of TE_{221} mode and a maximum E field magnitude of 15036V/m.

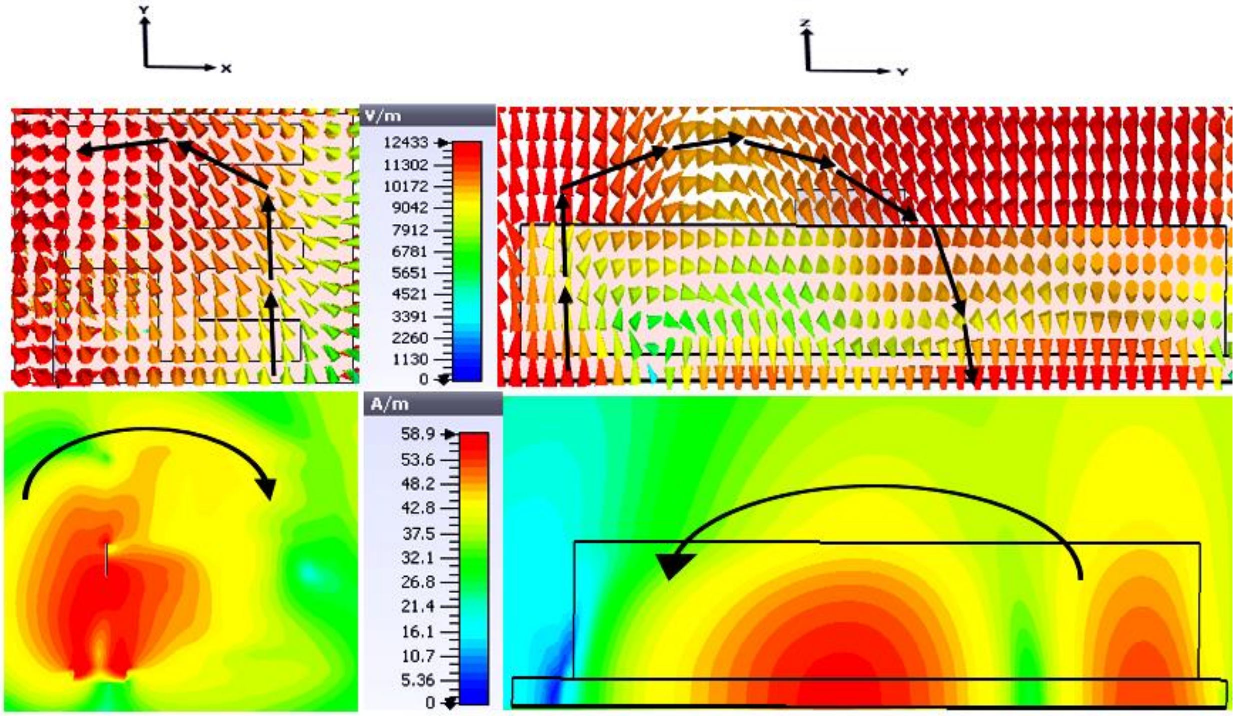

a b

Figure 4.8 a-b: 2-D view of E-field distribution over inverted 'OM' shaped DRA surface; a). X-Y plane view at 4.8GHz, b). X-Z plane view at 4.8 GHz (TE_{111})

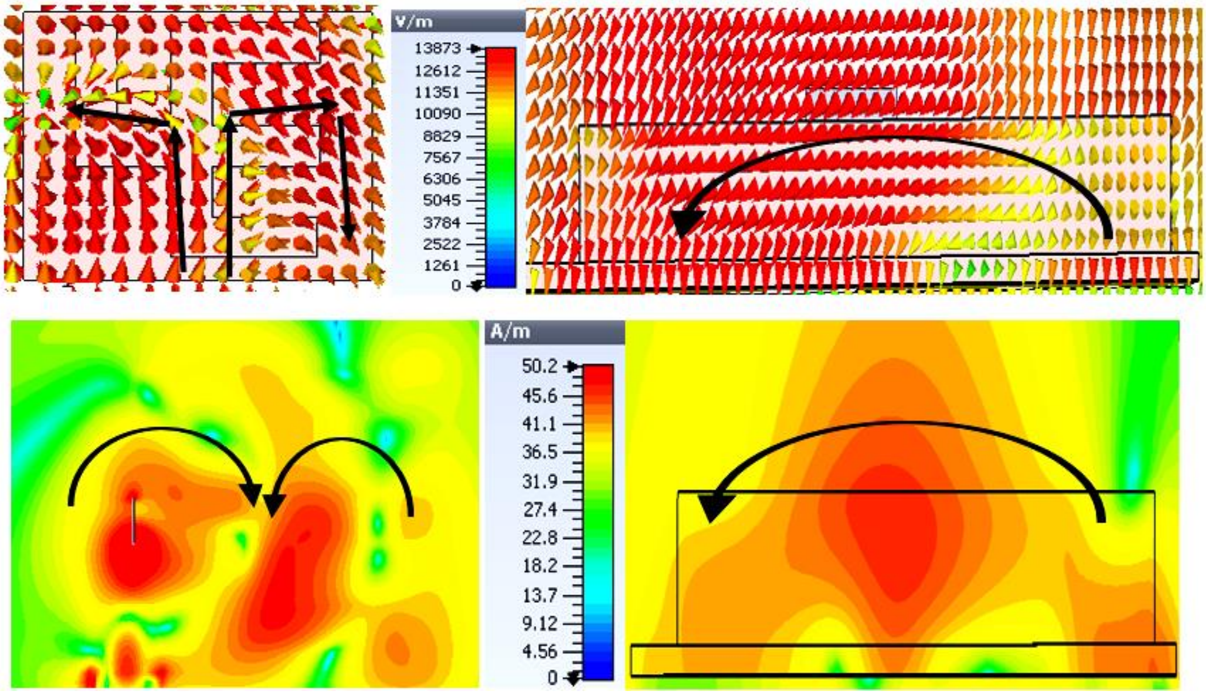

c d

Figure 4.8 c-d: 2-D view of E-field distribution over inverted 'OM' shaped DRA surface; c). X-Y plane view at 6.5GHz, d). X-Z plane view at 6.5GHz (TE_{211})

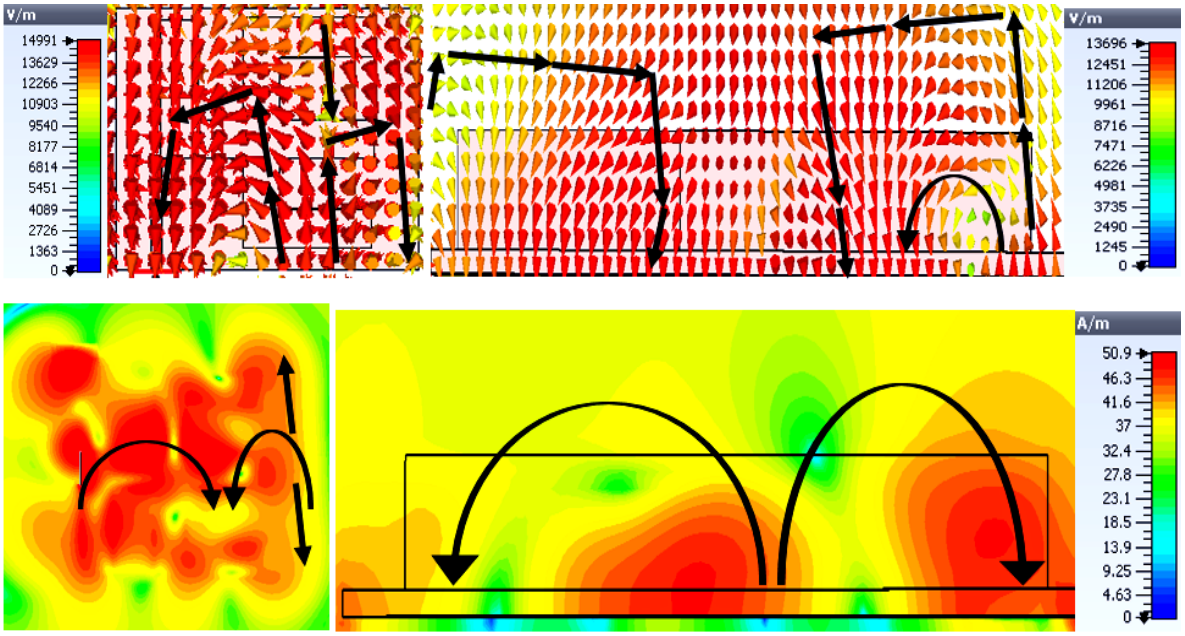

e f

Figure 4.8 e-f: 2-D view of E-field distribution over inverted 'OM' shaped DRA surface; e). X-Y plane view at 8.35 GHz, f). Y-Z plane view at 8.35 GHz (TE_{221})

It is also observed from figure 4.9a- d that the electric field distribution follows an elliptical path over the DRA's surface at the frequencies of 6.5, 7.2, 8.35, and 10 GHz supporting the view that the antenna radiates out elliptically polarized EM waves in its far field of operation and hence overcomes any polarization mismatch losses in the received signal strength. In order to further illustrate the generation of elliptically polarized EM waves by the proposed DRA, as figure 4.9a-b shows, the orthogonal modes, TE_{211}^{x} and TE_{211}^{y} generated on the surface of OM-shaped DR at the frequencies of 6.5 and 7.2GHz. Furthermore, TE^{y}_{221} and TE^{x}_{221} orthogonal modes are also generated on the DRA surface at the frequencies of 8.35 GHz and 10 GHz, as illustrated in figure 4.9c - d. The orthogonal modes indicate that the OM-shaped DRA radiates the horizontal and vertical components of the E field. The E field component at TE^{y}_{221} has a higher magnitude (15036 V/m) as compared to TE^{x}_{211} (13873V/m), and the E field component at TE^{x}_{221} has a higher magnitude (14991V/m) as compared to TE^{y}_{221} (13696V/m) for the proposed DRA. Therefore the proposed OM-shaped DRA shows an elliptically polarized behaviour (with axial ratio < 10dB) for the frequency band from 6 to 11.1GHz.

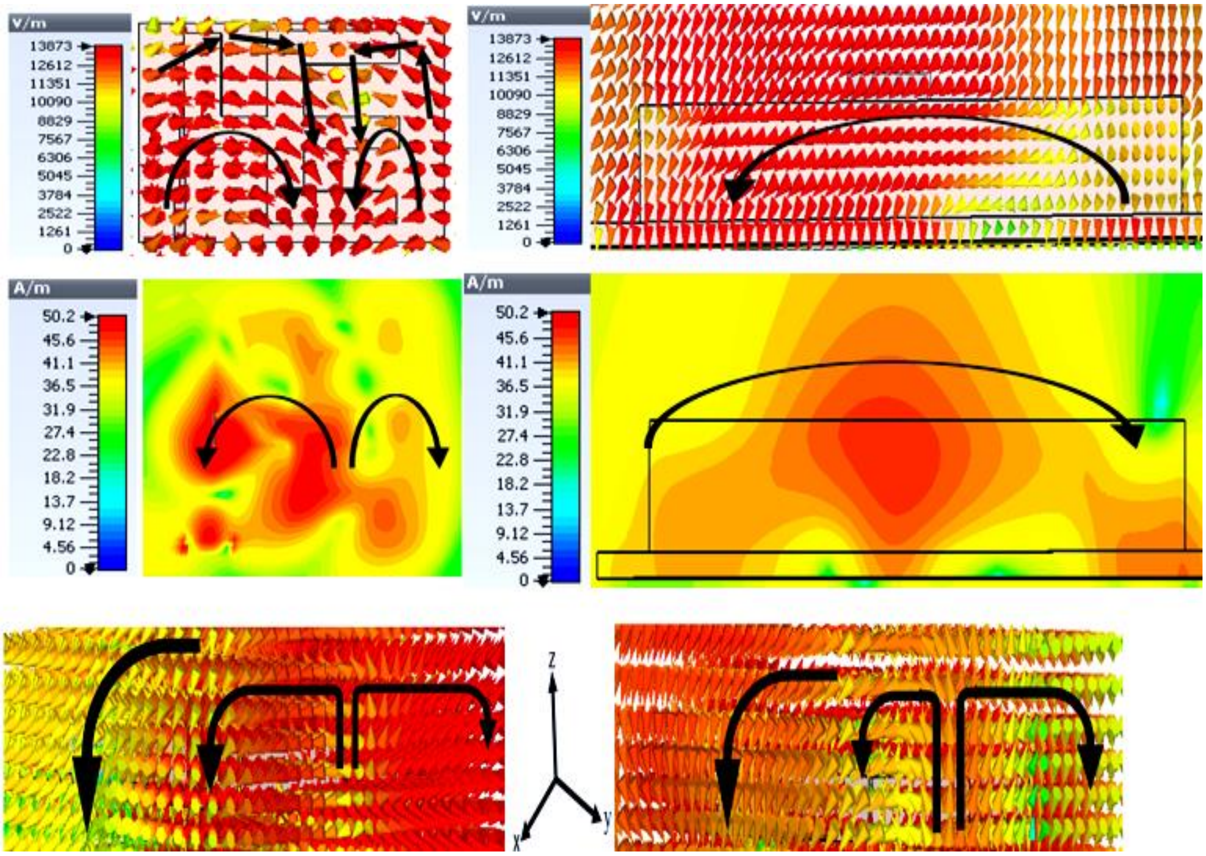

a b

Figure 4.9 a-b: validation of orthogonal modes of; a). TE_{211}^{x} at 6.5 GHz, b). TE_{211}^{y} at 7.2GHz

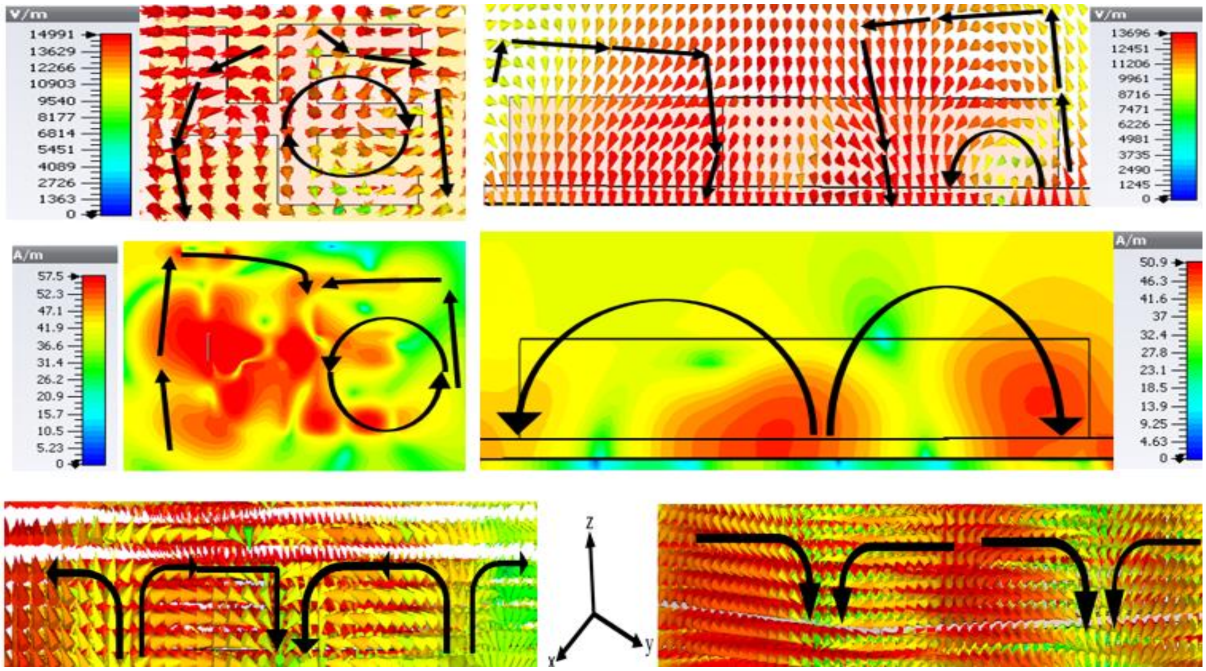

c d

Figure 4.9 c-d: validation of orthogonal modes of; c). TE^{x}_{221} at 8.35GHz, d). TE^{y}_{221} at 10 GHz

4.2.4 Parametric Optimization of OM-shaped DRA

This section presents the parametric optimization carried out for the proposed OM-shaped DRA parameters to obtain the desired UWB and gain characteristics. The DRA optimization is performed in CST MWS V.16 software, parametric sweep option with the time-domain solver. The DRA design procedure mentioned in the previous section explains the optimization of the rectangular block of DR to the final OM-shaped DR geometry. The optimization of the conformal strip for desired impedance matching results is stated. Some more DRA parameters that are optimized are the slots in the ground and the length and width of the feedline. The final DRA optimized parameters are mentioned in table 4.1. The details of parametric optimization are mentioned in further subsections as follows.

4.2.4.1 Optimization of P-type feedline

The width of the feedline from the lower and upper end of the P shape has been optimized to get the desired impedance matching of 50 ohms with the proposed DRA. Figures 4.10a-b show the simulated S-parameter graph of proposed DRA when feedline width is optimized and for the impedance matching of W_{f1}. The feedline width of W_{f1} and W_{f2} is varied from 1 to 3.5 mm and 0.5 to 2 mm, and it is observed that a feedline width of 2mm and 1mm give the best results with an impedance bandwidth from 3.1 to 11.4 GHz; hence it is best suited for the proposed DRA geometry. Figure 4.11c shows the best impedance matching for a frequency band of 3.1 to 11.4 GHz, as the black color plot shows that the best input impedance matching of 50 ohms is maintained for the desired UWB for the proposed DRA operation. Figure 4.10d offers the parametric optimization of the feedline length. It is observed from figure 4.10 that if the length of the feedline increases, the resonances start shifting towards the right, and the impedance matching at the resonances also reduces. It is observed that the best value of feedline length l_{f2} = 14.8mm is observed with a reported impedance bandwidth of 8.26 GHz (3.14 to 11.4 GHz), as shown in Figure 4.10d, and hence it is chosen as the best-optimized value for the feedline length.

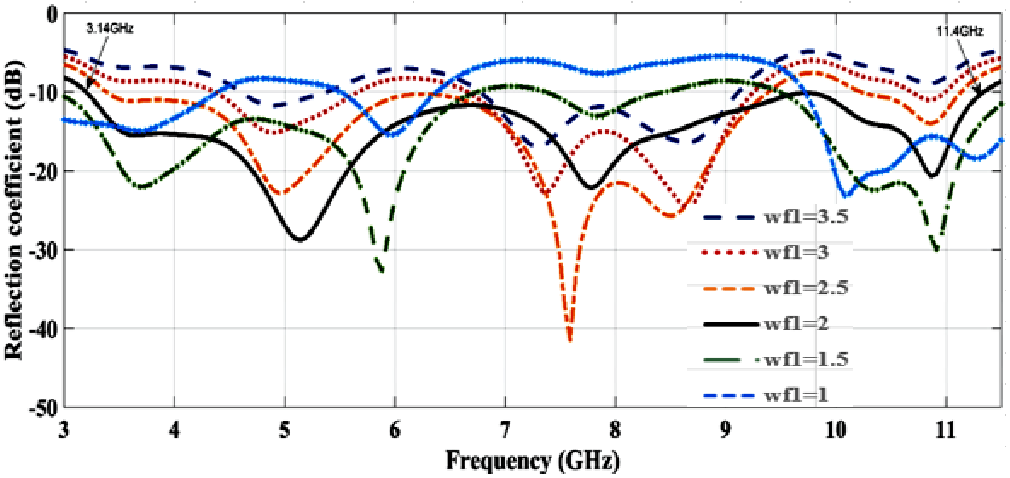

Figure 4.10a: Parametric optimization of feedline the width wf1varies from 1 to 3.5 mm

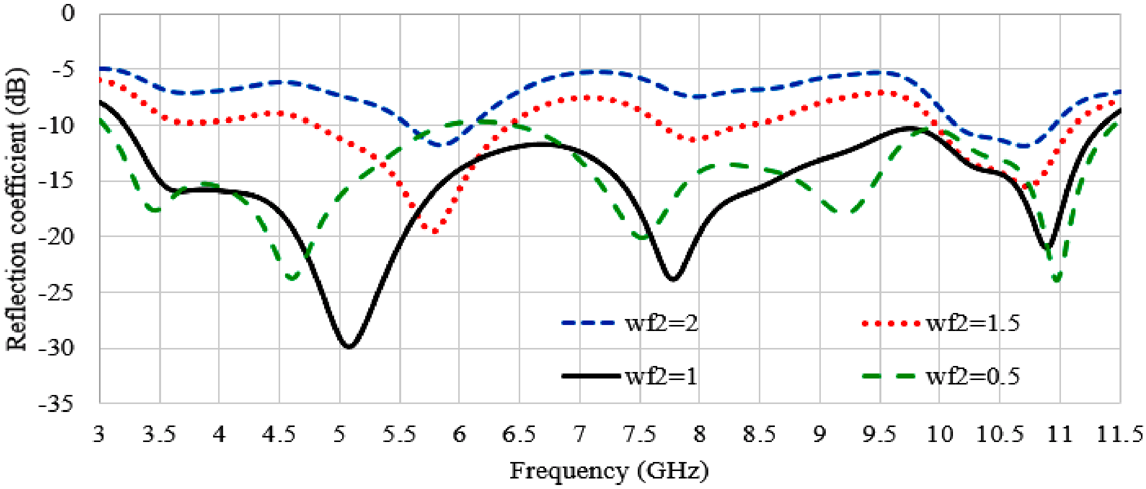

Figure 4.10b: Parametric optimization of the width wf2 of feedline varies from 0.5 to 2 mm

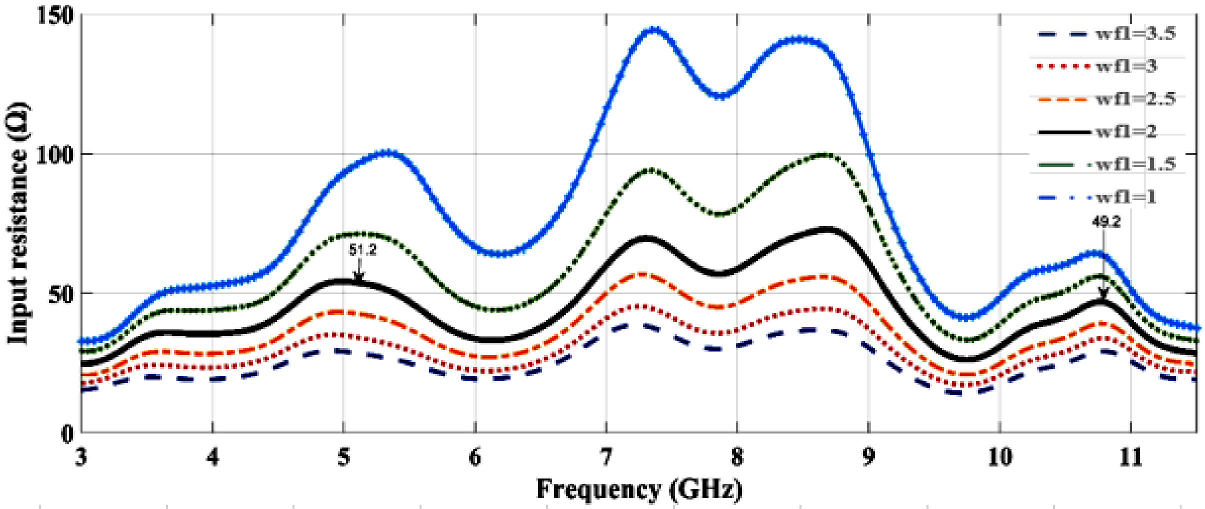

Figure 4.10c: Parametric optimization of the width wf1 of feedline for 50 ohm impedance matching

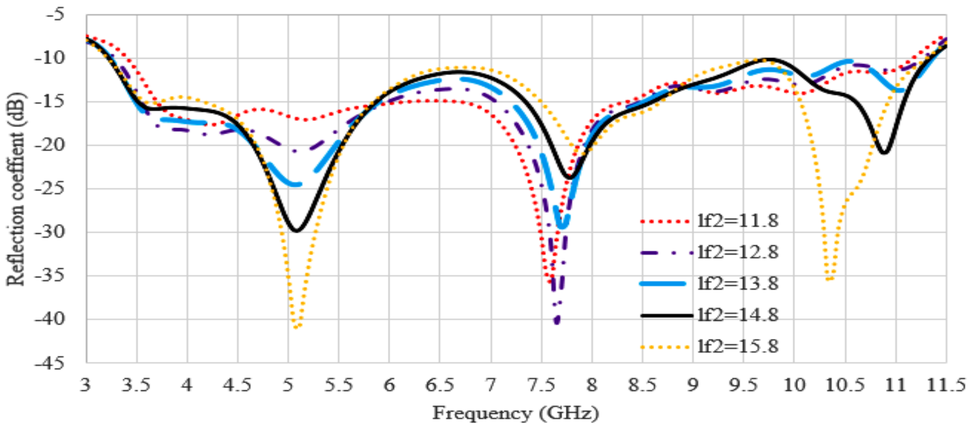

Figure 4.10d: Parametric optimization of the length lf2 of feedline varies from 11.8 to 15.8 mm

4.2.4.2 Variations in the conformal strip's height and length

A metallic conformal strip of copper with optimized dimensions of $l_{ms} \times h_{ms}$ as 5.7mm × 4 mm is also coupled between the feedline and the backside of DRA. This improves the impedance matching at the desired UWB from 3.1 to 11.4 GHz and improves the axial ratio bandwidth of the proposed antenna for the elliptically polarized wideband exhibited by the proposed DRA from 6 to 11.1GHz. Figures 4.11 a-b show the parametric variations followed while optimizing the height and length of the conformal metallic strip to get the desired impedance bandwidth results. The height of the conformal strip is varied from 0 to 7.2 mm, and the length is varied from 3.9 to 7.5 mm. Since best results are obtained with the metallic strip's height of 4mm and length of 5.7 mm, as shown in figures 4.11 a-b, these are the selected parameters for the copper-based metallic strip height and length.

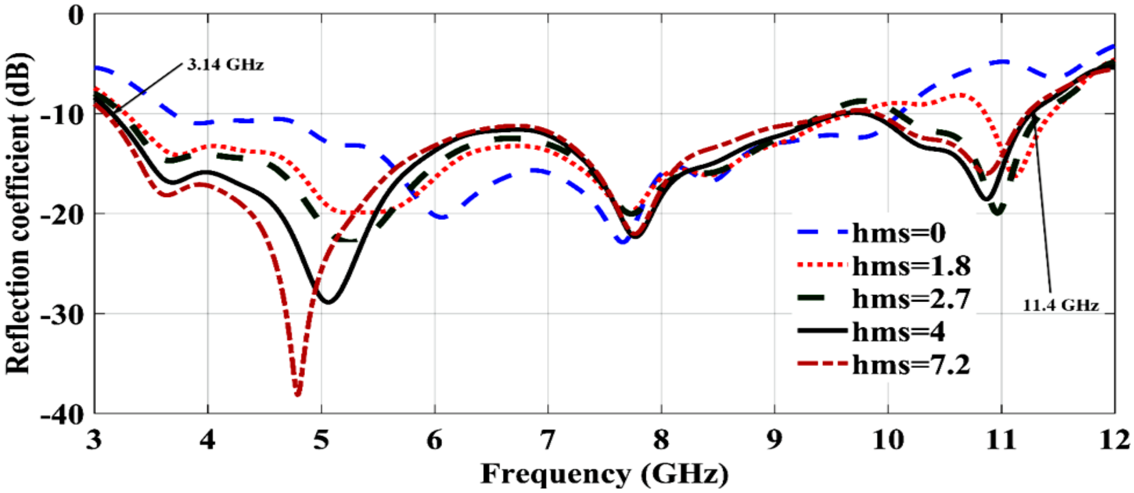

Figure 4.11a: Variation in the impedance bandwidth results of proposed DRA by varying the height of the metal strip

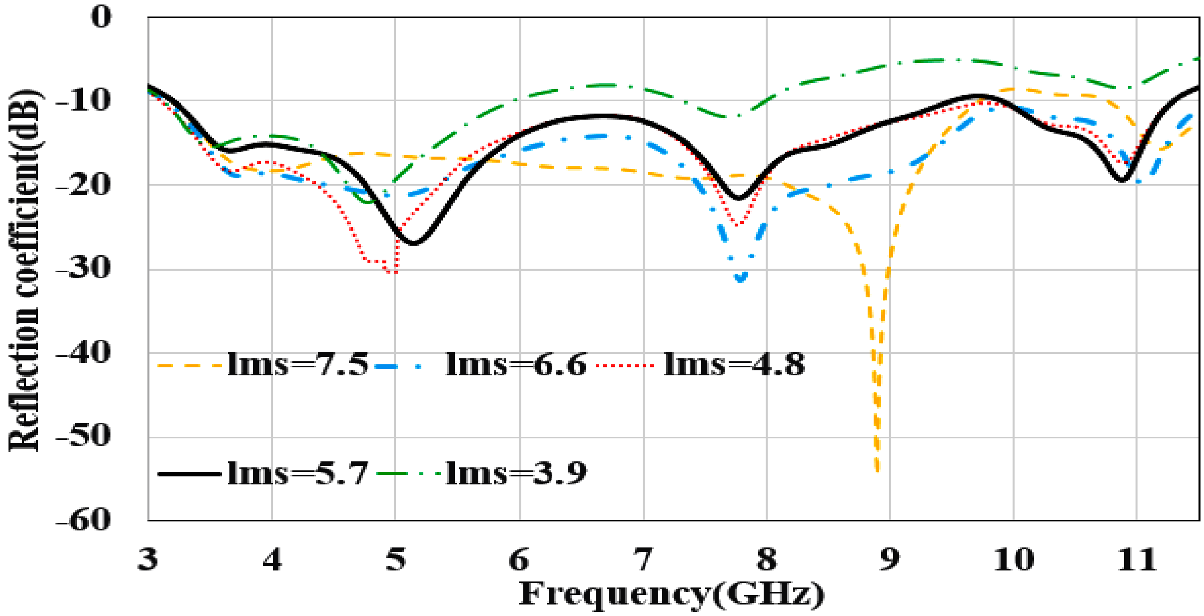

Figure 4.11b: Variation in the impedance bandwidth results of proposed DRA by varying the length of the conformal strip

4.2.4.3 Variation of Slots (Length and Width) in the ground

The ground layer of the proposed DRA is made defected with three slots cut from it to excite the desired UWB (3.1 to 11.4 GHz). The rectangular slot on the extreme right side of the ground layer was optimized for its length and width. Figures 4.12a-b show the variation in the dimensions of the Gl1 and Gw1 slot (refer Figure 4.1b) parameters in the ground layer to obtain the desired ultra-wideband response from the proposed OM-shaped DRA. It can be observed from figures 4.12a-b that the length and width of the rectangular side slot are varied from 4.8 to 6 mm for slot length and 17.5 to 21.5 mm for slot width, respectively, to optimize the impedance bandwidth of the proposed DRA. It is observed that as the slot's length increases, the resonance shifts towards the right, and the impedance matching also deteriorates. With the decrease in length of the slot, the resonance shifts towards the left, and the impedance matching at the entire band is disturbed since the best results of the impedance bandwidth are obtained at Gw1=19.5mm and Gl1= 5.2 mm, which excites the desired UWB with optimized impedance bandwidth, shown as a black curve in figure 4.12a-b from 3.1 to 11.4 GHz.

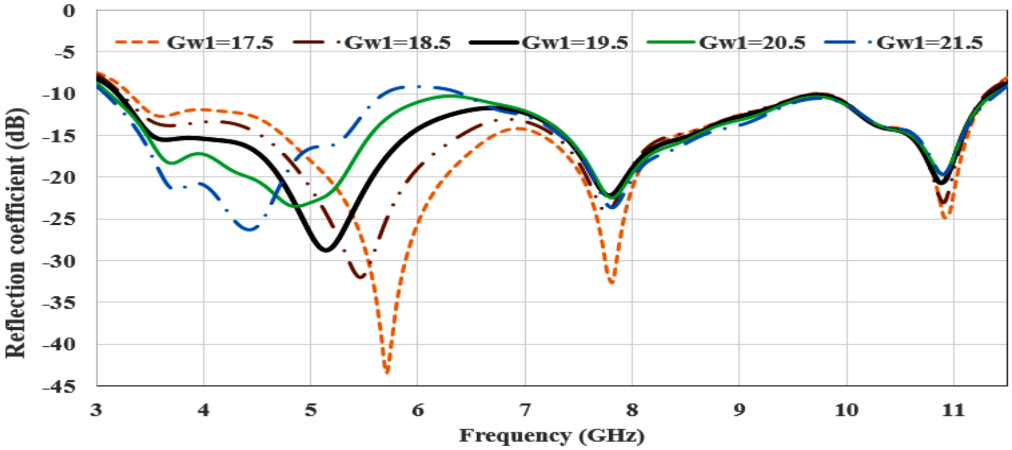

Figure 4.12a: Parametric optimization of the rectangular side slot for Gw1 parameter

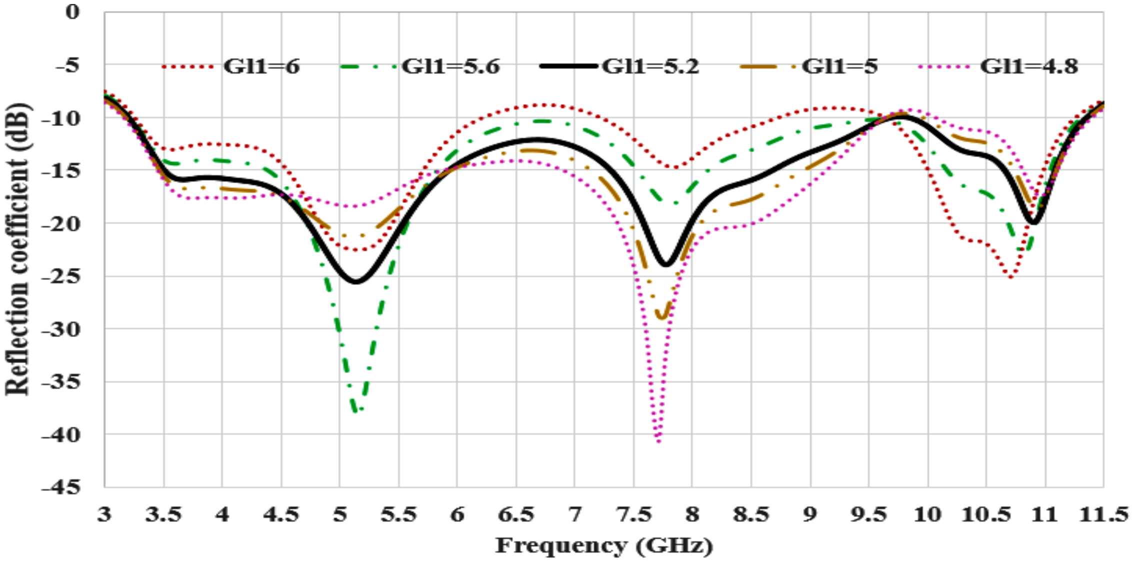

Figure 4.12b: Parametric optimization of the rectangular side slot for Gl1 parameter

4.2.4.4 Current distribution on DRA Ground surface

The proposed antenna had three slots cut from the infinite ground, with and without DGS, as the T-shape and two rectangular slots are shown in Figure 4.1b (back view). The slot has been cut in such a way as to increase the effective path length of the surface current shown in Figure 4.13a-c. This Figure shows the surface current distribution with and without DGS in the ground at 4.8, 7.25, and 10.5 GHz. It is observed that the DGS modifies current distribution on the ground and reports higher-order modes at higher frequencies because of multiple resonant paths present on the side of higher frequencies, as shown in Figure 4.13 a-c.

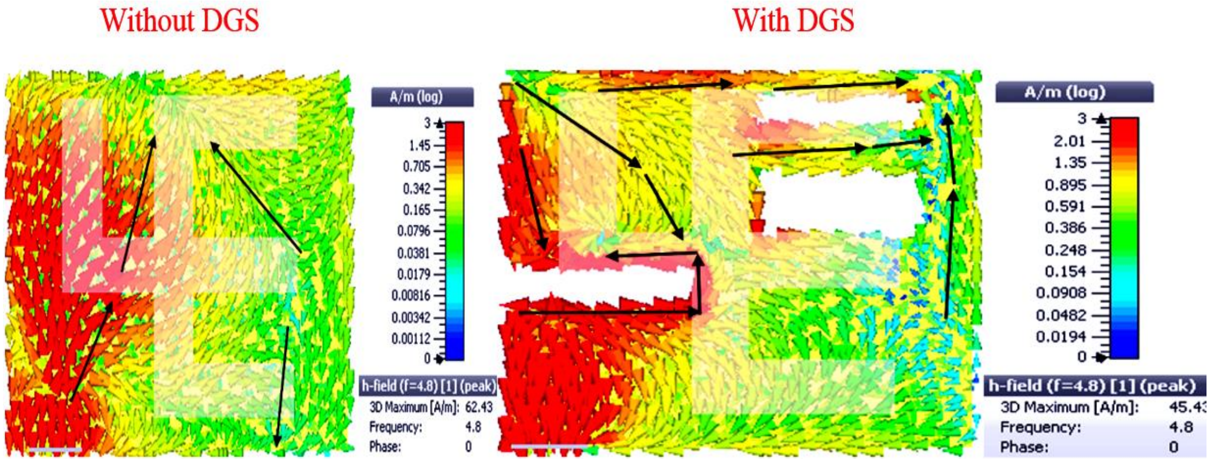

Figure 4.13a: Surface current distribution with and without DGS in the ground at 4.8 GHz

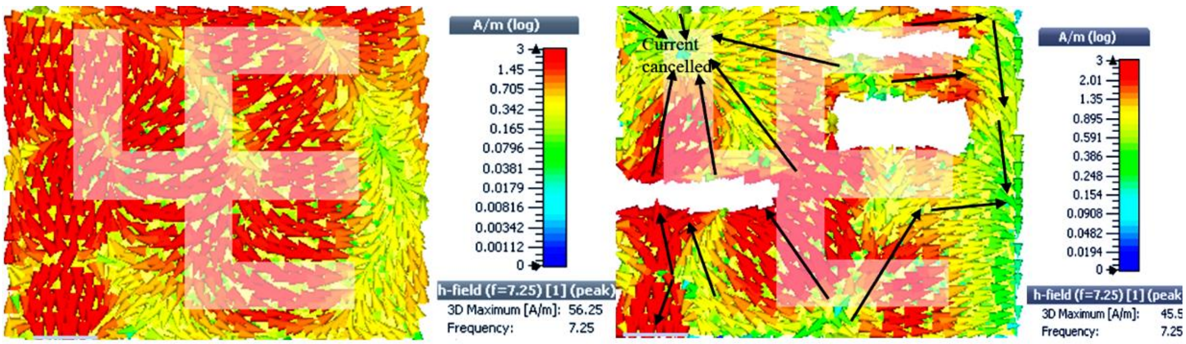

Figure 4.13 b: Surface current distribution with and without DGS in the ground at 7.25 GHz

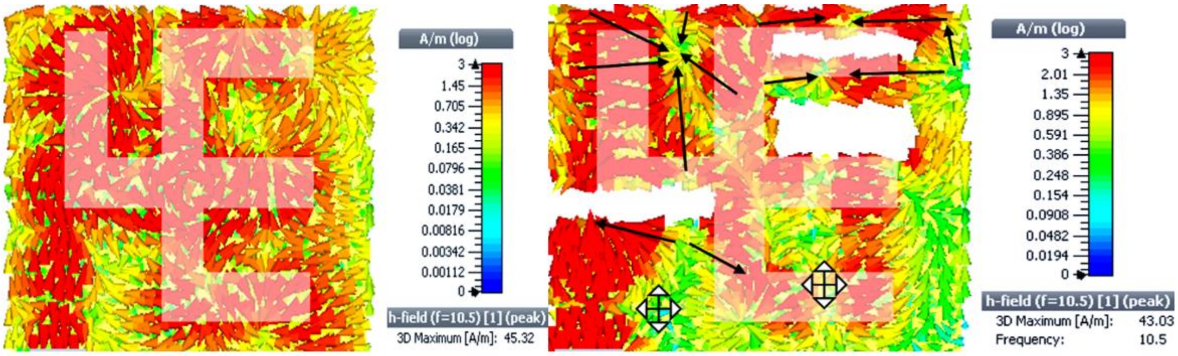

Figure 4.13c: Surface current distribution with and without DGS in the ground at 10.5

4.2.5 DRA Fabrication and Validation of simulated Results

The proposed OM-shaped DRA was fabricated using two dielectric substrates, a Rogers 5880 ($\varepsilon_S = 2.2$ & h = 0.8mm) and an Alumina ($\varepsilon_{DR} = 9.8$ and h = 4mm). The defected ground structure and the feed network (of copper with a thickness of 35 microns) are deposited on the bottom and top of the Rogers substrate, respectively, using a wet etching process. After that, an OM-shaped dielectric resonator is cut out from an Alumina sheet (Al_2O_3) using a water jet cutting process and fixed over the Rogers substrate at the termination point of the P-type feedline using an instant glue (Araldite). Figure 4.14a shows the snapshot of the proposed ‘OM’ shaped DRA prototype, which was tested using a VNA E 5093A to validate its S_{11} results. The fabricated antenna is also tested for its gain and radiation pattern measurements in an anechoic chamber (chamber with a frequency range of 10 kHz to 18GHz). Figures 4.14 b-c show the snapshots of the antenna’s back and front view, respectively, while measuring the antenna’s gain and radiation pattern in the anechoic chamber.

a b c

Figure 4.14: a). Prototype of the proposed OM-shaped DRA on a Rogers’s sheet, b). Back view of an antenna in an anechoic chamber, c). Front view of the antenna while testing

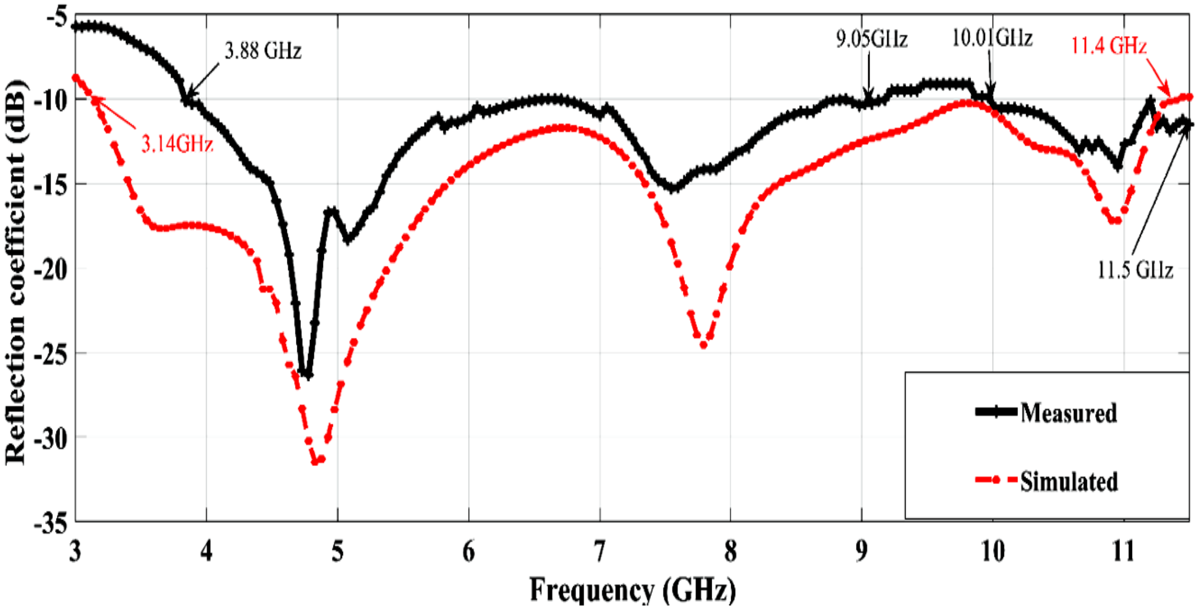

Figure 4.15: Comparison of simulated and measured S_{11} parameter of the OM Shaped DRA

Figure 4.15 shows the comparison plot of the proposed antenna's simulated and measured S-parameters with respect to frequency. It can be seen from figure 4.15 that the measured results closely follow the simulated ones. A slight variation in calculated results from the simulated ones can be seen, and the main reason for this can be credited to the fact that the instant glue (Araldite with $\varepsilon_r = 3$) that is used to paste the DR on the substrate causes a little impedance mismatch at the desired band. In addition to this, the measurements are made in a typical LAB environment. The nearby surroundings cause reflections to the radiating antenna and thus cause an impedance mismatch to the proposed DRA during radiation. The tested antenna shows a measured impedance bandwidth of 5170MHz and 1500 MHz from 3.88 to 9.05 GHz and 10 to 11.5 GHz, respectively, with 79.99% and 13.95% impedance bandwidths at the center frequencies of 6.42 GHz and 10.5GHz, respectively. Table 4.2 shows the comparison details of frequency bands covered by the OM-shaped DRA and the bandwidth at those bands in terms of simulated and measured results.

Table 4.2: Comparison of Simulated and measured impedance bandwidth of the antenna

Results(S parameters) by	**Frequency Band**	**Impedance BW**
Simulated using CST MWS V’16	3.14 to 11.4 GHz	8.26 GHz and 112%
Measured on VNA	3.88 to 9.05 GHz and 10 to 11.5 GHz	5.17GHz, 79.99% at 6.46GHz and 1.5GHz, 13.95GHz at 10.75GHz

The gain measurements of the proposed DRA were also done in an anechoic chamber using a Horn antenna with a calibrated gain of 12dBi. Figures 4.16a-c and 4.17a-c depict the comparison plots of simulated and measured polar plots of the co and cross-polarization radiation (gain) patterns of the proposed DRA at three resonant frequencies of 4.8 GHz, 7.2GHz, and 10.5 GHz, respectively (as the azimuthal and the elevation planes of antenna’s radiation). The proposed DRA shows an approximate omnidirectional radiation pattern in the elevation plane, as shown in Figure 4.16. The gain is found to be stronger than cross-polarization gain by around -16dB at the three mentioned resonances along the elevation plane. Figure 4.17 shows the co and cross-polarization patterns of the proposed DRA along the azimuthal plane. An approximate omnidirectional pattern is also seen along the azimuthal plane with a co and cross-polarization magnitude difference of around -18dB at the three resonances.

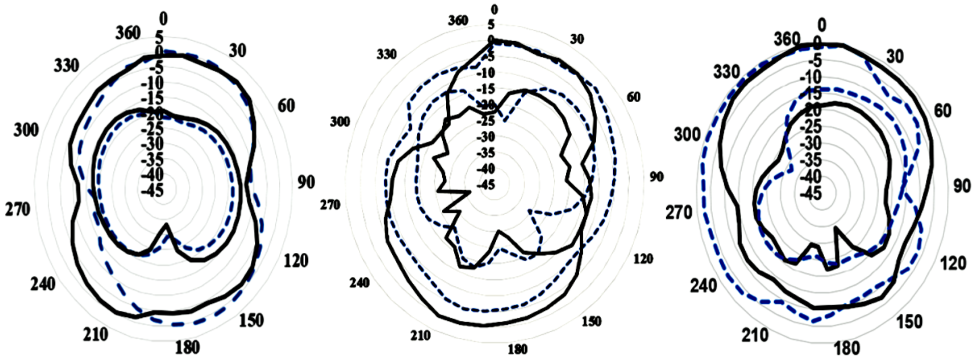

a b c

Figure 4.16 a-c: Comparison of Simulated and measured Co and cross-polarization gain pattern at a). 4.8 GHz, b). 7.25 GHz, c). 10.5 GHz in the Azimuthal plane

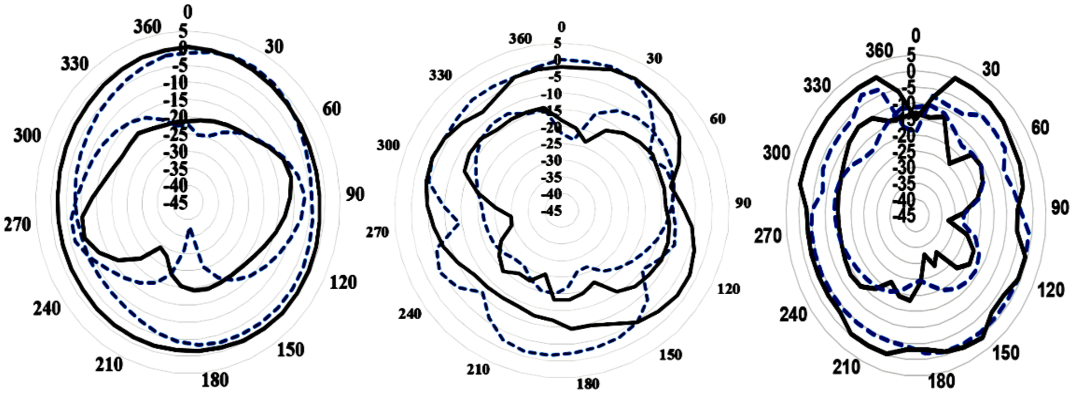

a b c

Figure 4.17 a-c: Comparison of Simulated and measured co and cross-polarization gain pattern: a). 4.8 GHz, b). 7.25 GHz, c). 10.5 GHz in the elevation plane

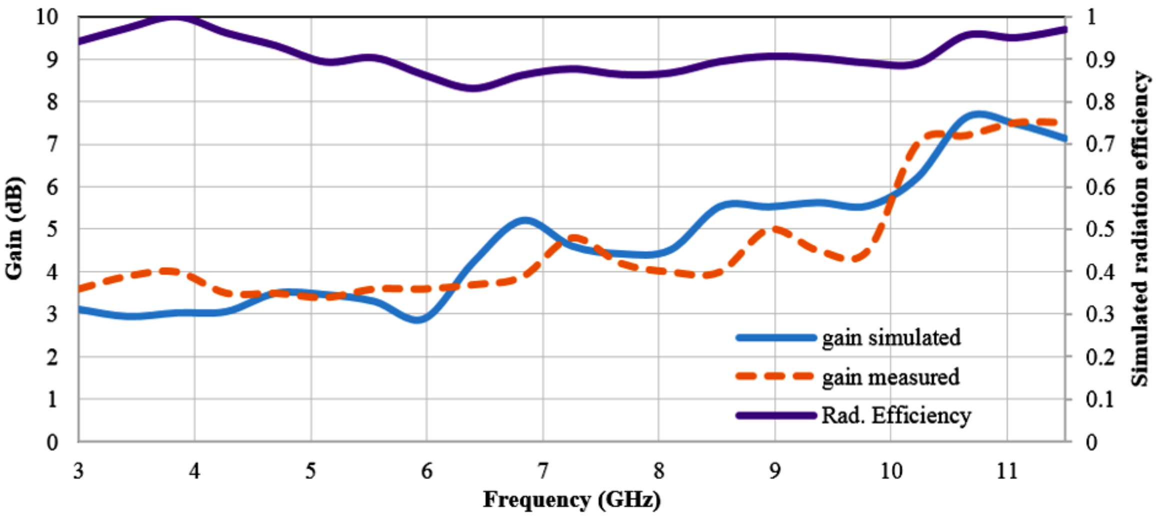

Figure 4.18: Simulated and measured gain and simulated radiation efficiency

Figure 4.18 shows a plot of the antenna's simulated radiation efficiency as a function of frequency and also the comparison plot of the proposed DRA's simulated and measured gain. It can be seen from the figure that the antenna shows a peak measured gain of 7.68 dB at around 11.3GHz and an average gain of approximately 4.6dB for the entire band of operation (compared to a simulated peak gain of 7.68 dB and an average gain of 4.7dB for the entire band). This allows the antenna to be practically suitable for short-range indoor wireless communications for 4G and 5G portable devices to support high data rate multimedia applications. The proposed DRA also possesses average radiation efficiency of around 93% and is, therefore, an efficient radiator for multimedia-rich UWB applications.

The next part of this chapter explains the details of CP DRA for UWB operations in section 4.3.

4.3 Broadband circularly polarized stacked dielectric resonator antenna

This subsection presents the second DRA design that covers the third research objective of the proposed doctoral research work. Therefore a compact asymmetrical structured DRA with an F-shaped metallic strip-based ground plane that is used to achieve broadband axial ratio bandwidth (from 6.4 GHz to 12.4 GHz) is presented here. The proposed DRA shows a broadband CP operation.

4.3.1 Antenna Geometry and Configuration

The geometry of the circular polarized asymmetrical shaped DRA is shown in Figure 4.19. It consists of two rectangular DR blocks of Alumina (permittivity $\varepsilon_{DR} = 9.8$) as shown in red and blue color, fed with current using a microstrip feedline as shown in Figure 4.19 (a & c-d). The first and second block height, length, and width are t_{DR1}, t_{DR2}, l_{DR1}, l_{DR2}, w_{DR1}, w_{DR2}. The ground and feed network is printed on a low-cost FR_4 substrate ($L_s \times W_s \times t_s$) as $25 \times 25 \times 0.8$ mm^3) having an electrical permittivity (ε_s) of 4.4. On top of this substrate, a microstrip feedline is printed to excite the DR radiator with 50 Ω input impedance. The microstrip feed-line has two parts $l_{f1} \times w_{f1}$ (50 Ω) and l_{f2} ($\lambda/4$) $\times$ w_{f2}, which are added to each other. The metallic F-shaped strip added with a partial ground plane is printed on the bottom side of the substrate. The partial ground plane has dimensions $Lg \times W_g$, and F-shape metallic strip parameters are l_{t1}, l_{t2}, l_{t3}, s_{t1}, and s_{t2}, as shown in Figure 4.19b. The metallic strip is used to maintain the overall gain of the antenna. The perspective and side view of the final designed antenna is shown in Figure 4.19c-d. All design parameters with optimized values are given in Table 4.3.

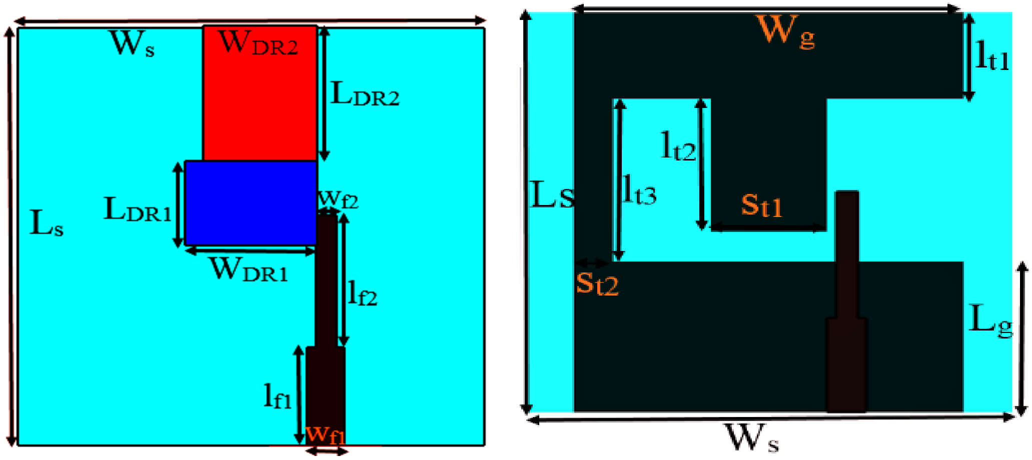

a b

Figure 4.19: Compact size of DRA; a). Top view, b). Back view

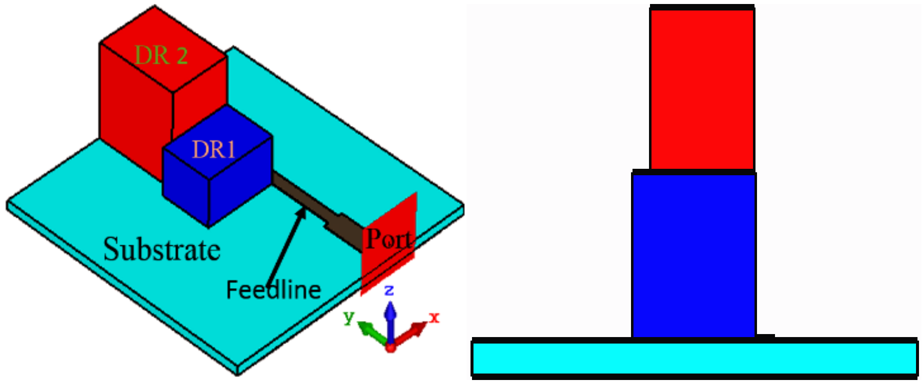

c d

Figure 4.19: Compact size of DRA; c). Perspective view, d). Side view

Table 4.3 Optimized Dimensions of the proposed antenna

Parameter	Dimension_(mm)	Parameter	Dimension _ (mm)	Parameter	Dimension _ (mm)
Ls = Ws	25	**W_g**	20	**st2**	2
L_g	9.4	**WDR1**	7	**lt1**	5.4
ldr1	5	**W DR2**	6	**lt2**	7.6
ldr2	8	**wf1**	2	**lt3**	10.2
lf1	5.9	**wf2**	1.1	**t_{DR1}**	4
lf2	7.9	**st1**	6	**t_{DR2}**	8

4.3.2 DRA Design Procedure and Operation

The proposed circular polarized asymmetrical shaped DRA is designed and simulated using CST MWS V.16 software with mesh-type hexahedral settings and 50 Ω fixed input impedance matching and open boundary conditions along X, Y, and Z directions of the time domain solver. Two rectangular sheets of dimensions $L_{DR1} \times W_{DR1} \times t_{DR1}$ mm^3 and $L_{DR2} \times W_{DR2} \times t_{DR2}$ mm^{3}of commercially available Alumina (Al_20_3) are segmented to each other to form the final optimized asymmetrical shaped DRA.

4.3.2.1 Stacked DRA design and operation

The final DRA that is designed and developed has five intermediate evolution step structures in ascending order, as depicted in Figure 4.20 as Ant.1, Ant.2, Ant.3, Ant.4, and Ant.5. The design of the DRA is carried out using perturbation theory, the stacked asymmetrical structure of DR is employed to improve the impedance bandwidth and obtain a wide AR bandwidth [113]. The volumes (Vdra) of two DRs (DR1 and DR2) are 140 mm^3 and 384 mm^3 (A total volume: 524 mm^3), as shown in Figure 4.19c. The total volume (Vtotal) of DRA is 728 mm^3 (13 × 7 × 8). Therefore the air-spaced volume Vs = 728 – 524 = 204 mm^3. The effective permittivity (ε_{reff}) of the DRA depends on the volume (V_s, Vdra) and relative permittivity (ε_{DR} = 9.8). With and without perturbed DR is calculated as ε_{reff} = 7.14 using equation (4.8). Thus, ε_{reff} and Qp of DR decrease using equation (4.9 to 4.10), improving the bandwidth of the proposed antenna.

$$\varepsilon_{reff} = \frac{\varepsilon_{DR}Vdra+\varepsilon_0 Vs}{Vdra+Vs} \tag{4.8}$$

$$Q=\frac{1+3(\frac{\pi}{\sqrt{\varepsilon_{DR}}})^2}{(\frac{\pi}{\sqrt{\varepsilon_{DR}}})^3\left[1+(\frac{\pi}{\sqrt{\varepsilon_{DR}}})^2\right]} \tag{4.9}$$

$$Qp=\frac{1+3(\frac{\pi}{\sqrt{\varepsilon_{reff}}})^2}{(\frac{\pi}{\sqrt{\varepsilon_{reff}}})^3\left[1+(\frac{\pi}{\sqrt{\varepsilon_{reff}}})^2\right]} \tag{4.10}$$

The resonant frequency of DRA operation is calculated by Equation (4.11 to 4.13) at 10.65 GHz when the total size of DRA is 13 × 7 × 8 mm^3, and values of kx, ky, kz, ko are 448.79, 392.69, 196.34, 230.79, respectively.

$$f_{TE_{lmn}} = \frac{v}{2\pi\sqrt{\varepsilon_{reff}}}\sqrt{k_x^2 + k_y^2 + k_z^2} \tag{4.11}$$

$$k_x = \frac{l\pi}{l_{eff}},\ k_y = \frac{n\pi}{w_{eff}},\ k_z \tan\left(k_z \frac{h_{DR}}{2}\right) = \sqrt{(\varepsilon_{reff}-1)k_0^2 - k_z^2} \tag{4.12}$$

$$l_{eff} = l_{dr1} + l_{dr2}\ ,\ \text{and}\ w_{eff} = w_{dr1} + w_{dr2} \tag{4.13}$$

Where k_0 represents the wave number in the free space, k_x, k_y, and k_z are wavenumbers.

The dimensions of the DRA substrate are taken to be 25 × 25 × 0.8 mm^3, which has a modified ground structure, and the DR is excited by a QWT feedline. Figure 4.21a-c shows the simulated S_{11}, gain, and axial ratio plots for each intermediate step followed when developing the stacked CP DRA.

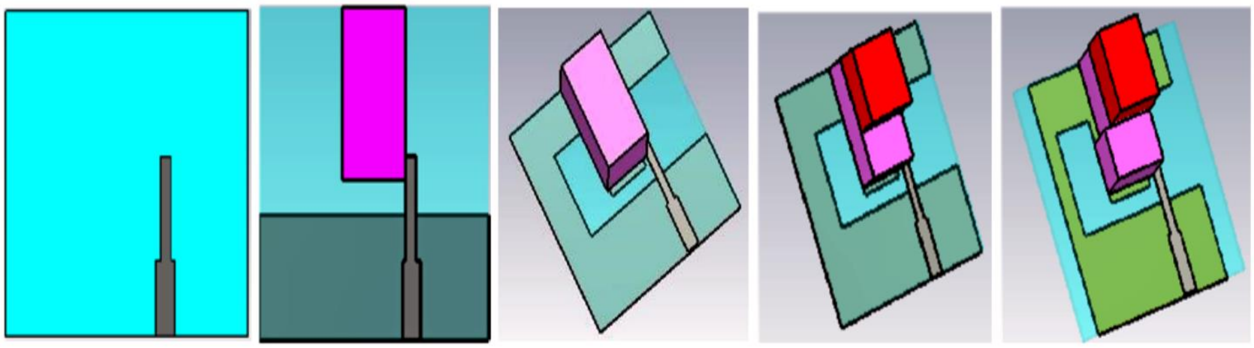

Ant. 1 Ant. 2 Ant. 3 Ant. 4 Ant. 5

Figure 4.20: Intermediate Design steps of the final DRA design (Ant. 5)

Table 4.4 shows the results in terms of S_{11}, Gain, and Axial Ratio of Intermediate steps of designed DRA (Ant 5), and these steps are discussed one by one as follows.

Table 4.4: Performance of all five antennas

Antenna Steps Name	**10 dB Impedance BW %**	**Peak Gain(dB)**	**AR BW(≤3)**	
			Band 1	**Band 2**
Ant. 1	-	2.5	-	
Ant. 2	70.3 % (6 to 12.5 GHz)	3.77	-	
Ant. 3	68.1 % (6 to 12.4 GHz)	5.64	8.3 % (6.9 to 7.5 GHz)	8.9% (8.6 to 9.4 GHz)
Ant. 4	63.8 % (6.4 to 12.4 GHz)	5.36	17.3 % (8.7 to 10.3 GHz)	
Ant. 5	63.8 % (6.5 to 12.4 GHz)	5.6	63.8 % (6.5 to 12.4 GHz)	

- **Step 1:** Ant.1 is designed and simulated with the full ground using CST MWS V'16. It has an FR4 substrate with electrical permittivity of 4.4, the ground is etched on the bottom side of the substrate, and the QWT feedline that offers input impedance of 50 Ω, is etched on the top of the substrate, as shown in Figure 4.20. This antenna has no operating bandwidth, S_{11} plot of Antenna 1 is shown in Figure 4.21a (green color). Therefore in step 2, a DR block is mounted on the substrate to excite the desired frequency bands.
- **Step 2:** In Ant.2, a DR of dimensions 13 × 7 × 8 mm^3 calculated using equations (4.11 to 4.13) is mounted on top of the base substrate, and a partial ground is etched on the bottom of the substrate. Ant.2 obtains broad impedance bandwidth of 70.3% (5.8 to 12.4 GHz) with a gain of 3.77 dB but does not have a 3 dB AR bandwidth, as shown in Figure 4.21a-c by the dotted red color plot Antenna 2 reports a low gain. Therefore the ground is modified in step 3.
- **Step 3:** Ant.3 is formed by modifying Antenna 2 by using an F-shaped metallic strip that is added with the partial ground, and no change to the DR shape is made. This modified ground provides the constant gain within the operating range of the antenna, as shown in Figure 4.21. Ant. 3 reports an impedance bandwidth of 68.1% from 6 to 12.4 GHz with a peak gain of 5.63 dB. This antenna also shows a dual-band CP of 8.3% (6.9 to 7.5 GHz) and 8.9% (8.6 to 9.4 GHz).
- **Step 4:** Further, Ant.4 is an improved version of Antenna 3 by adding DR2) a second block (Red-one) on top of the DR1 block (the pink one) placed earlier. This provides an asymmetrical shape to the DRA, having two different heights of 4 mm (The first one) and 8mm (the Second one). This Ant. 4 geometry achieves an AR bandwidth (17.4 %) from 8.7 to 10.3 GHz and impedance bandwidth (63.8%) from 6.4 to 12.4 GHz, respectively.
- **Step 5:** Ant. 5 geometry is designed with improved DR widths. The width of the second DR is increased by 1mm from 6 to 7mm to achieve an AR bandwidth of 63.8 % (6.4 to 12.4 GHz), as observed in Figure 4.21c. Table 4.4 shows the performance of the designed antenna having five different stages.

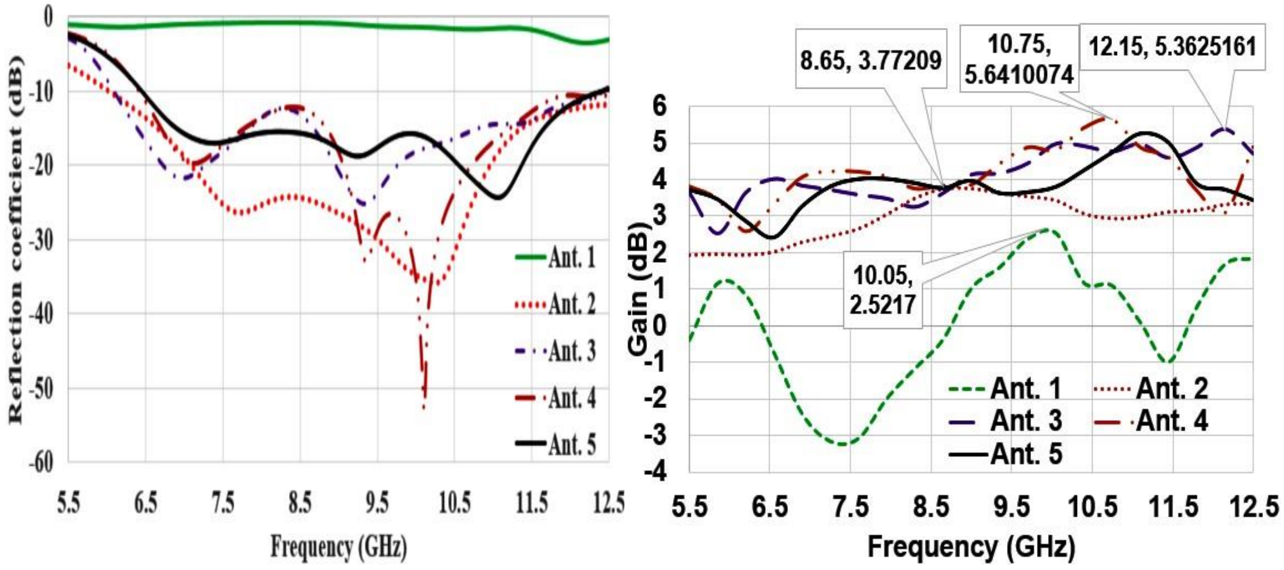

a b

Figure 4.21: Intermediate Design steps of proposed DRA; a). S_{11} plot, b). Gain

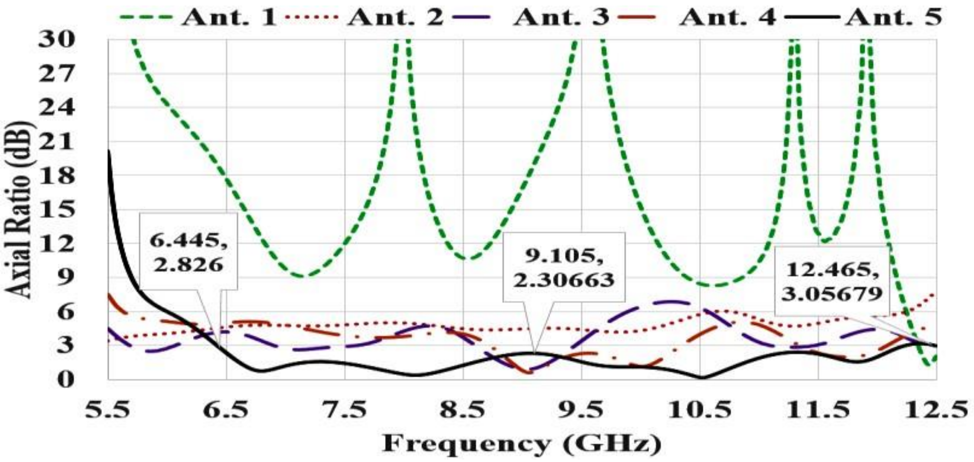

c

Figure 4.21c: Frequency response concerning Axial Ratio

4.3.2.2 Validation of Field Modes and CP Mechanism

The concept of E-field analysis is reported in this subsection. Figure 4.22 shows the impedance plot of the antenna showing the resonant frequencies at the different operating modes [114] [115]. There are two peaks of the real part of the impedance plot to confirm the operation of the antenna with two resonating modes at 9.1 and 11.28 GHz. Figure 4.24 shows the E field distribution inside the DR at these frequencies. Figure 4.23 a-b confirms the operation of an antenna with the fundamental and third-order mode as $TE_{\delta 11}$ and $TE_{\delta 13}$ at frequencies of 9.1 and 11.28 GHz, respectively.

To understand the mechanism of CP generation, the E −field distribution is analyzed in the constant $z = h$ plane at different time instants, shown in Figure 4.25a - d. The rotation of the field vector in the clockwise direction with respect to t=0, t/4, t/2, 3t/4, and t represents the dominant left-hand CP field radiation that could be verified by analyzing the radiation pattern reported in the later section of this chapter [21]. The E field distribution in the constant z −plane is reported at the fundamental mode frequency only, and not reported at the frequency of higher-order mode for brevity. However, the analysis also represents the clockwise rotation of the field vectors at the higher-order mode operation frequency.

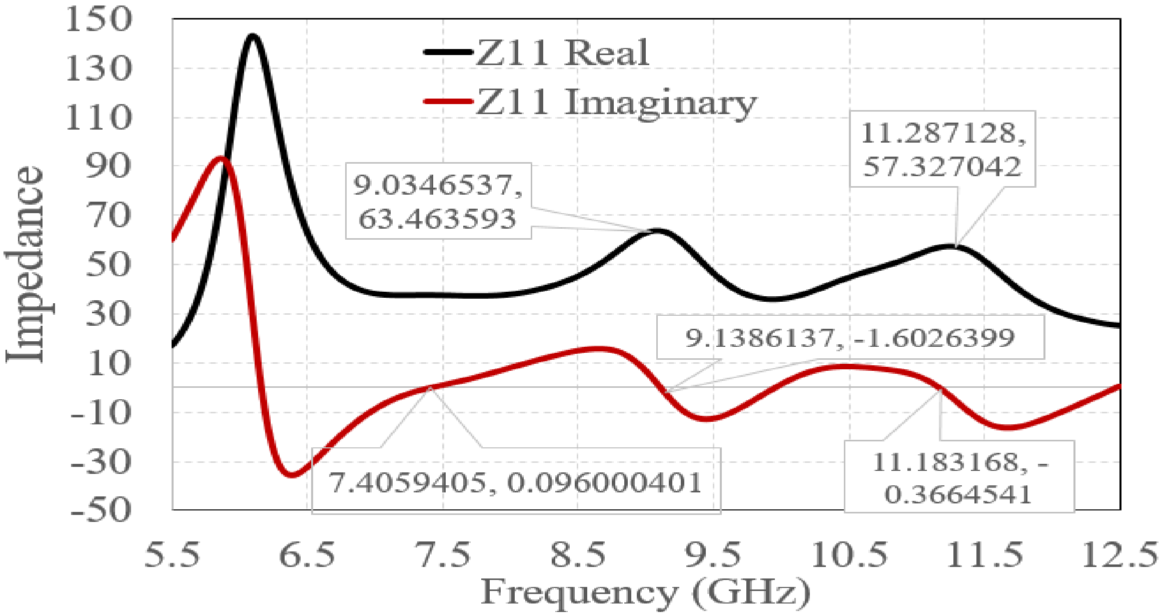

Figure 4.22 The impedance plot of the antenna showing the resonant frequencies

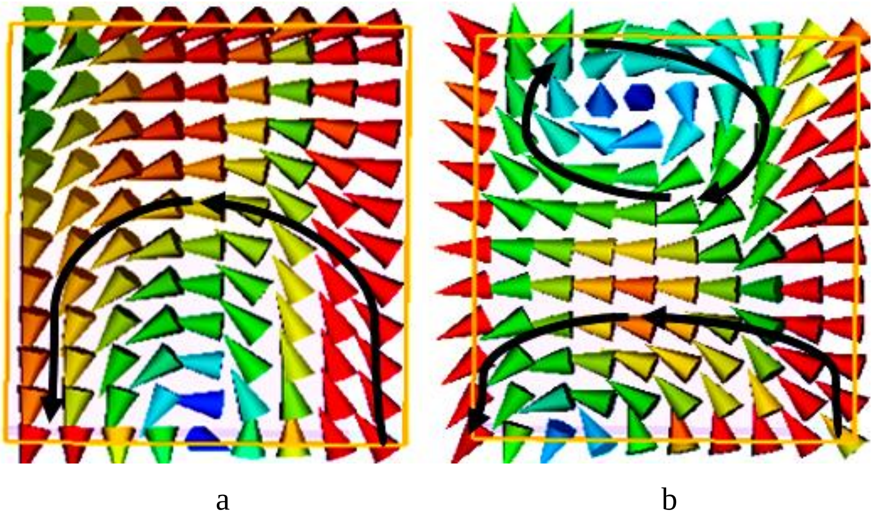

a b

Figure 4.23 The E field distribution at; a). 9.1GHz, b). 11.28 GHz

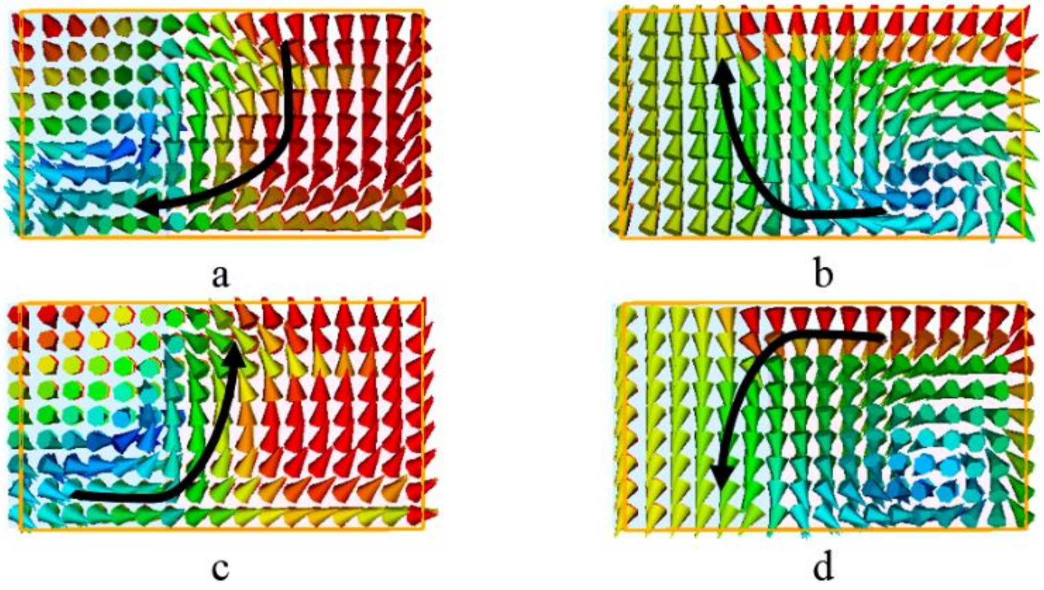

Figure 4.24 The E field distribution in constant $z = h$ plane at 9.1 GHz at the time; a). $t = 0$, b). $t = T/4$, c). $t = T/2$, d). $t = 3T/4$

4.3.3 Parametric Optimization of Stacked DRA

The parametric optimization of the DRA dimensions for achieving the best DRA outcomes and the parameter to use for the CP inside the antenna structure is carried out in this subsection of the chapter. The DRA optimization is performed using the CST MWS V.16 software, with the parametric sweep option and the time-domain solver. Here each parameter is varied one at a time to examine how it affects the performance of the proposed antenna in terms of reflection coefficient, AR bandwidth, and impedance bandwidth. Further subsections mention the specifics of parametric optimization one at a time.

4.3.3.1 Variation of the height of DR

The asymmetric size of DRs affects the frequency band of operation and AR bandwidth. The height of two DRs are t_{DR1} and t_{DR2}, and are varied to obtain the best value via parametric sweep and can be seen from Fig. 4.26a–d. When t_{DR1} is varied from 2 to 10 mm, t_{DR2} is fixed to 8 mm. The frequency band shifts to the left as t_{dr1} increases, as seen in Figure 4.26a. The proposed antenna's best AR bandwidth (6.4 to 12.3 GHz) is claimed to be 4mm, making it the best value of $t_{DR1,}$ as shown in Figure 4.26b. In the next step, t_{DR1} is fixed, and t_{DR2} varies between 4 to 12 mm, as shown in Figure 4.26c-d. As t_{DR2} increases, the frequency band shifts to the left, as shown in Fig. 4.26c. Furthermore, as shown in Figure 4.26d, the proposed antenna is reported to have the best impedance and AR bandwidth 6GHz (6.4 to 12.4 GHz) of 8 mm, making it the best t_{DR2} value.

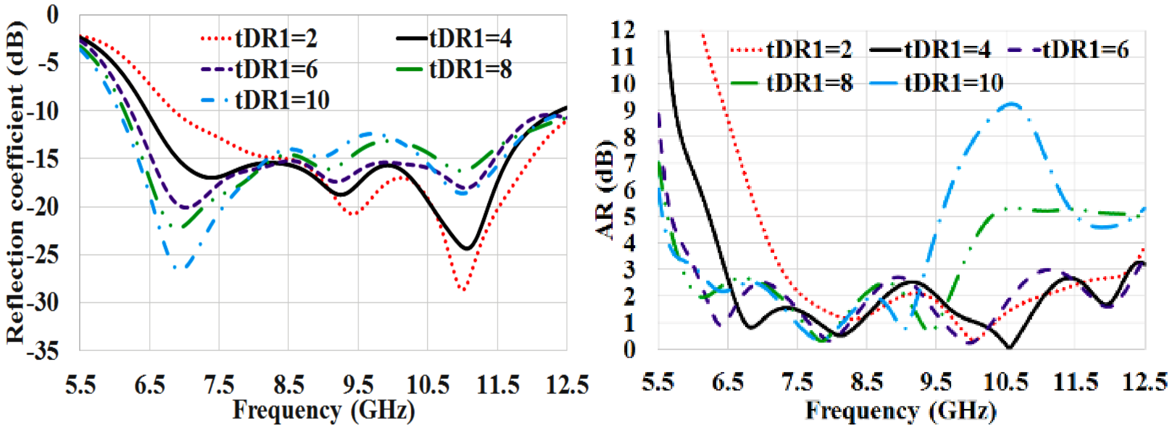

a b

Figure 4.26 a-b: Reflection coefficient and Axial Ratio for the various height of t_{DR1} (mm)

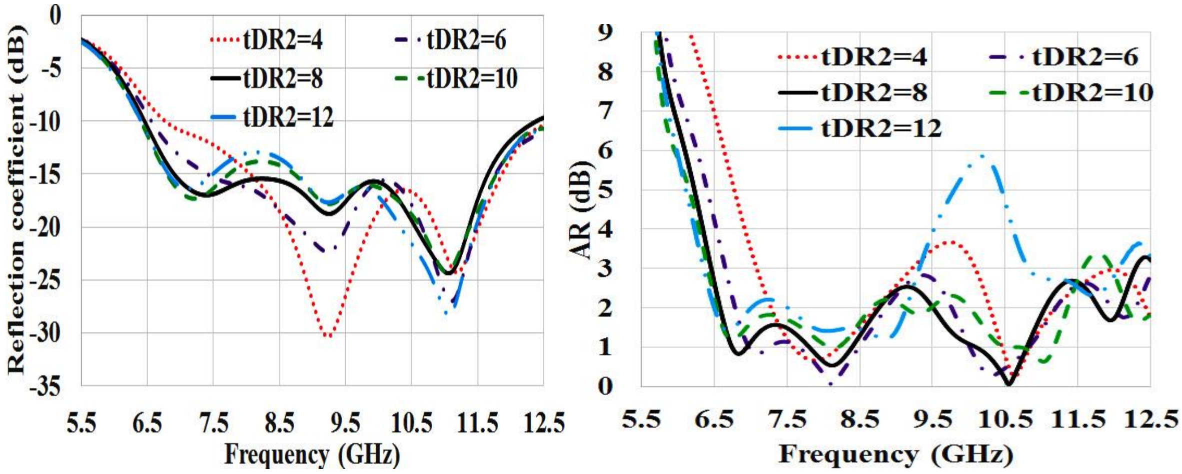

c **d**

Figure 4.26 c-d: Reflection coefficient and Axial Ratio for the various height of t_{DR2} (mm)

4.3.3.2 Variation of F-shaped strip

The modified ground plane has F shaped strip with main key parameters as s_{t1}, s_{t2}, l_{t1}, l_{t2}, and l_{t3}, as shown in Figure 4.19b. Here, two main parameters are varied as s_{t1} and st_2 to achieve a broader impedance bandwidth and AR bandwidth, as shown in Figure 4.27 a-d. When s_{t1} is varied from 3.5 mm to 8 mm, s_{t2} is fixed at 2 mm. The dual-frequency band is reported at 7.5 mm & 8 mm, as shown in Figure 4.27a. The best-optimized value of s_{t1} is 6 mm to achieve suitable impedance and AR bandwidth of 6 GHz (6.4 to 12.4 GHz). The second parameter of s_{t2} is varied from 1mm to 4 mm, and the best value of 2 mm is chosen as in Figure 4.27c – d to obtain a wide impedance and AR bandwidth of 6 GHz (from 6.4to 12.4 GHz).

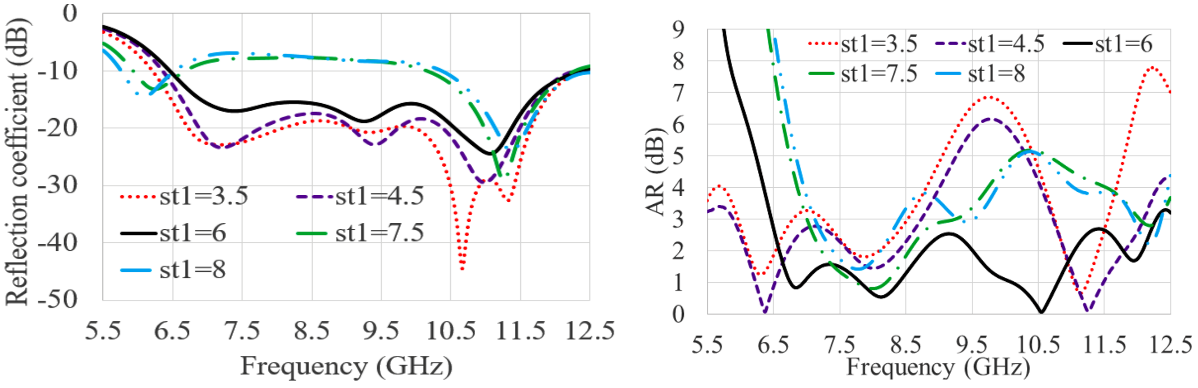

a b

Figure 4.26 a-b: Reflection coefficient and Axial Ratio for variation in st1 from 3.5 to 8 mm

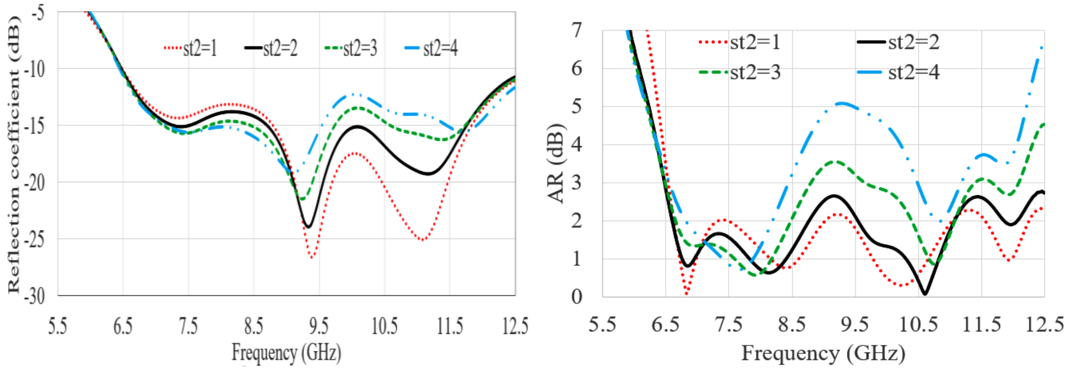

c d

Figure 4.27 c-d: Reflection coefficient and Axial Ratio for variation in st2 from 1 to 4 mm

4.3.4 Stacked DRA Fabrication and Measurements of Results for Validation

The proposed Asymmetric shaped stacked DRA was fabricated on FR4 substrate with a thickness of 0.8 mm, with electrical permittivity and tangential losses of 4.4 and 0.0024, respectively, using photolithography techniques. The feedline is printed on the top of this substrate, and DRA is placed on the substrate close to the feedline to excite the DRA for radiation. The ground layer of the F-shape is added on the bottom side of the substrate. The far-field results of this proposed antenna are measured using an anechoic chamber, and the fabricated prototype setup with test and measurement is shown in Figure 4.27a-b. The view of fabricated DRA is shown in Figure 4.27c-d.

The fabricated DRA has tested S_{11} (dB) parameters using a KEYSIGHT (E5063A) vector network analyzer, working on a frequency range from 500 MHz to 18 GHz. Radiation pattern (RHCP, LHCP), Gain, and axial ratio measurements are performed in an eco-free environment that is an anechoic chamber with a frequency range from 2 kHz to 18 GHz with a transmitter horn antenna of 12 dBi gain.

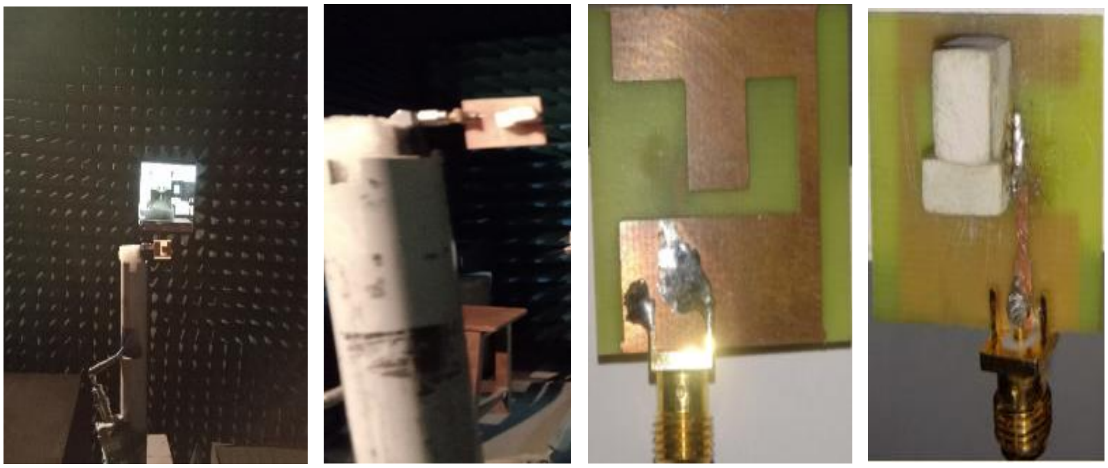

Figure 4.27: a-b). Measurement setup with DRA, c-d). Back and Top view of fabricated DRA

The simulated and measured S_{11} plot and AR plot of the designed antenna are presented in Figure 4.28 a-b. The measured S_{11} plot is almost similar to the simulated ones. However, slight left shifting of the frequency band is observed due to fabrication errors, and the use of Fevitite epoxy adhesive is used for joining the DR layers onto the substrate. The simulated and measured impedance bandwidth of 63.8% (6.4 to 12.4 GHz) and 66.7% (5.9 to 11.8 GHz) is observed. The simulated and measured AR bandwidth are obtained as 63.8 % (6.47 to 12.3 GHz) and 2.52 %, 43.7 % (5.8 to 6.1 GHz and 6.9 to 10.9 GHz), respectively.

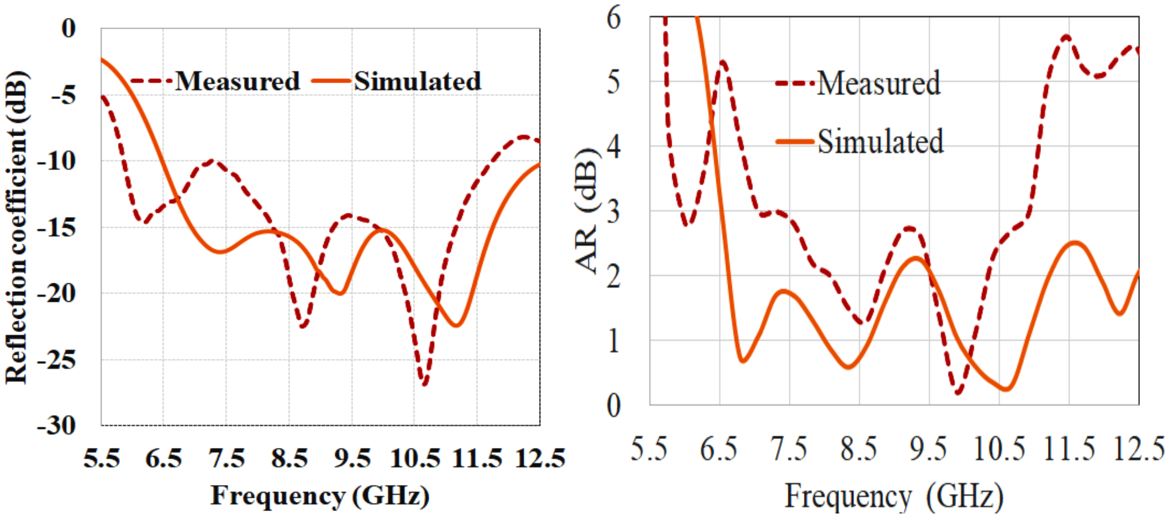

a b

Figure 4.28: Simulated and measured parameters; a). S_{11}, b). Axial ratio

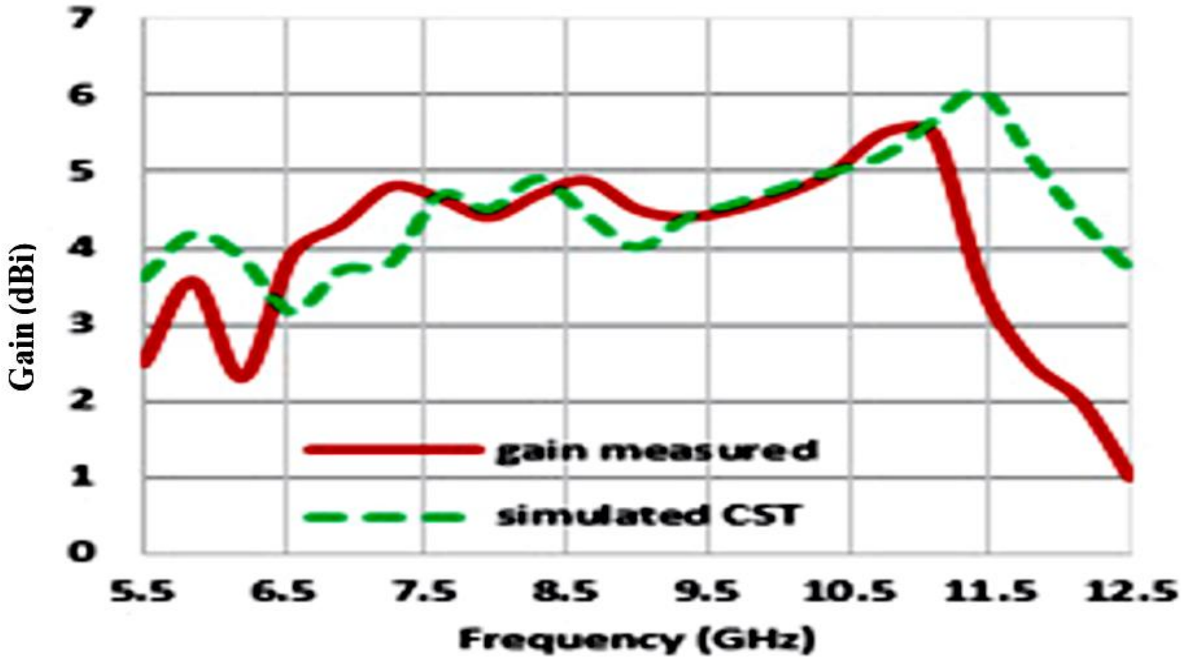

Figure 4.29: Gain as a function with frequency

The simulated and measured gain plot of the proposed asymmetric-shaped DRA over the operating frequency band is shown in Figure 4.29. It is observed that the simulated peak gain of 6.01dBi at 11.5 GHz and measured peak gain is 5.6 dBi at 11 GHz. There is a difference of around 0.5 dBi between the simulated and measured gain values. This mismatch can be explained because of the fabrication errors and measurement errors while executing DRA experimental testing.

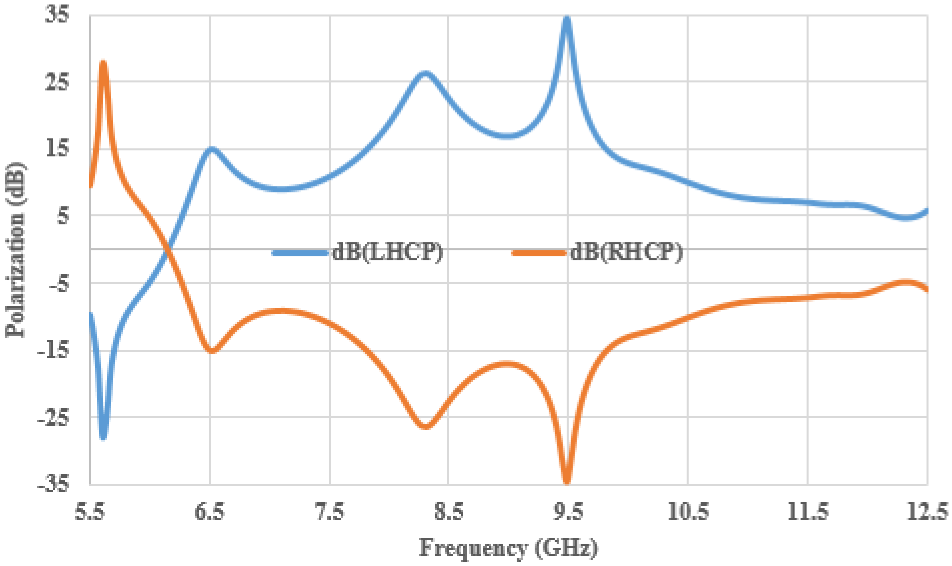

Figure 4.30: Simulated left-hand and right-hand circular polarization

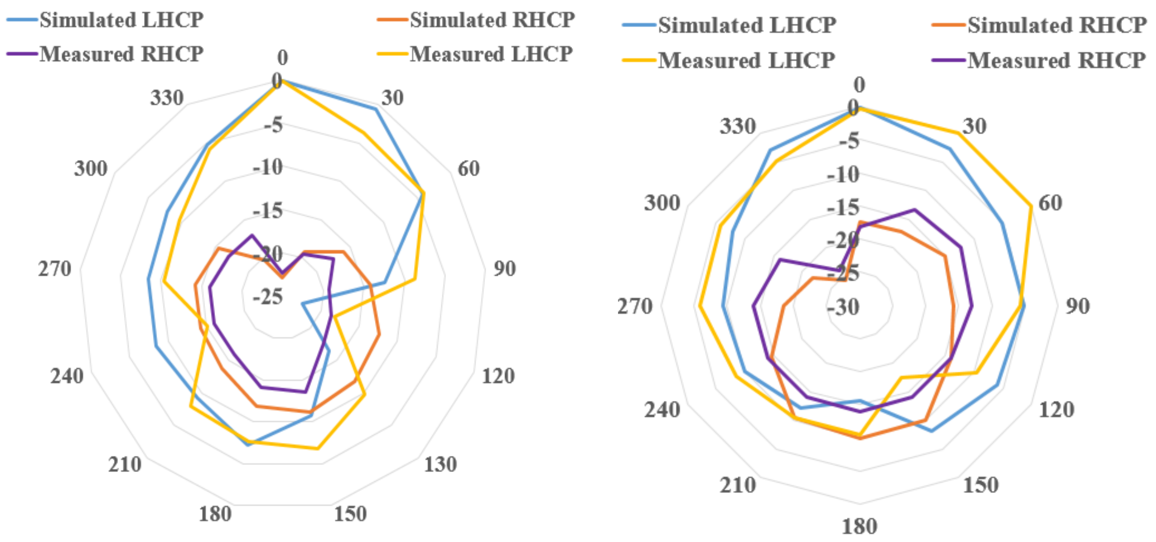

a b

Figure 4.31: Radiation pattern LHCP and RHCP at; a). 6.6 GHz, b). 9.1 GHz

This proposed antenna is dominated by the left-handed polarization (Blue & Yellow color) compared to the right-handed polarization (Orange & Purple color), as shown in Figure 4.30. Figure 4.31a - b shows the measured and simulated radiation patterns of the proposed DRA at 6.6 and 9.1 GHz for LHCP and RHCP. Good agreement between simulated and measured results have been reported. Referring to Figure 4.31a - b, it is observed that the LHCP fields are much stronger as compared to the RHCP in the proposed asymmetric-shaped CP DRA. So this antenna has LHCP property when phi =0 at 6.6 and 9.1 GHz.

4.4 Conclusion

This chapter presents the research work carried out to fulfill the third and second (partially) objectives of the proposed doctoral research work. Two broadband elliptically and circularly polarized DRAs are presented for UWB operation. The first DRA design is an OM-shaped DRA that achieved the UWB (3.1 to 11.1 GHz) communication with EP characteristics (6 to 11.1 GHz). The fabricated antenna consists of an OM-shaped DR made of alumina material mounted on the Rogers substrate and offers an input impedance of 50 ohms using a P-type microstrip feedline. The magnitude of the E field component with two orthogonal modes shows an elliptically polarized behavior from 6 to 11.4 GHz. The peak simulated radiation efficiency for the proposed DRA is reported to be 97.78%. In the second design, a compact stacked asymmetrically structured based DRA achieves the third objective for UWB (6.4 to 12.4 GHz) communication with CP characteristics (6.4 to 12.4 GHz). This antenna consists of two DR blocks with asymmetric height and width stacked over each other, excited by the QWT feedline. The asymmetrical shape of DR is used to obtain the CP with simulated and measured AR bandwidth (AR≤3) of 63.8% and 43.7%, respectively. The proposed stacked DRA has attractive performances for CP UWB systems. This antenna can be used for military applications, satellite communication, weather forecasting, defense tracking system, etc.

CHAPTER 5

DIELECTRIC RESONATOR ANTENNAS IN MIMO CONFIGURATION FOR UWB OPERATION

5.1 Introduction

MIMO antenna Configuration is implemented by employing multiple antennas on the transmitting and receiving sides of a communication system. MIMO systems are able to overcome multipath and fading issues related to high data rate communication systems [116]. Since DRAs are effectively used in high data rate applications, these antennas can be implemented in multiple input multiple output systems to achieve the aforementioned advantages of a MIMO communication system. Therefore, this chapter presents the design and development of two MIMO DRA configurations with dual ports that also cover the research work done to cover the fourth objective of the proposed doctoral research work. The proposed two radiators' element-based DRAs are excited by a quarter wave transformer feedline. Both the proposed DRAs are compact with an omnidirectional radiation pattern and present good isolation properties within the working UWB range of the proposed antennas.

The first DRA design is a **Compact Rack Shaped two element based MIMO DRA** consisting of two DRs (Rogers RT 6010) as radiator elements, placed on top of the FR4 substrate. These DRAs are fed with an inverted T-shaped metallic parasitic strip (MPS) placed between the two dielectric resonators (DRs) to improve the impedance bandwidth, and a separation of more than 15.6 dB has been reported within the UWB range. The second design that is presented in this chapter, is a **compact cross-shaped parasitic strip-based Dielectric Resonator Antenna array in a MIMO configuration.** The proposed MIMO DRA consists of two DRs having electrical permittivity (ε_{DR} = 10.2) of Rogers RT 6010 used as radiator element**s. The proposed compact cross-shaped parasitic strip MIMO DRA** is designed and fabricated to achieve high isolation (≥ 20dB within the range).

This chapter is divided into two sections. Section 5.2 discusses the first DRA design, fabrication, and testing to achieve the desired parameters, and section 5.3 discusses the second DRA design, fabrication, and testing to achieve the desired objective 4 of the proposed research work of in this doctoral thesis.

5.2 Compact Rack Shaped Two Element Based MIMO Dielectric Resonator Antenna

This section discusses the rack-shaped DRA with improved isolation for UWB operations. This MIMO antenna structure is implemented with the help of two rectangular-shaped DRs, which are further converted into rack-shaped DRs with a stub-based partial ground and inverted T-shaped MPS.

5.2.1 Geometry of Rack Shaped UWB DRAs in MIMO Configuration

The proposed UWB Rack-shaped DRA in MIMO configuration is as shown in Figure 5.1 a-b. The proposed DRA is designed as two rack-shaped DRs of Rogers RT 6010 with relative permittivity of 10.2, tan δ = 0.0023, thermal conductivity = 0.78 W/K/m and thickness of 5 mm, placed on a FR4 substrate (relative permittivity = 4.4, thickness = 0.8 mm, tan δ = 0.025, thermal conductivity = 0.3 W/K/m). The two radiator elements of dimensions $L_{DR} \times W_{DR} \times h_{DR}$ are excited by quarter wave transmission feedlines. An inverted T-shaped metallic parasitic strip (MPS) is placed between the two radiators. DRs and feedlines are fixed on the top of the substrate (FR4) layer, and a ground plane ($L_{gnd} \times W_{gnd}$) is etched on the bottom side of the substrate. The length and width of the substrate are $L_{sub} \times W_{sub}$, with a height (h_s) of 0.8 mm. In the center of the partial ground plane, an impedance matching stub ($l_{stub} \times w_{stub}$) is added for matching purposes and for providing good isolation between the proposed DRAs in MIMO configuration [117]. These antennas provide UWB behavior from 3.54 to 10.88 GHz with an impedance bandwidth of 7.34 GHz, having good isolation and low ECC in the excited UWB. The impedance bandwidth and AR bandwidth of the proposed antenna have been improved by using an inverted T-shaped MPS [118]. Figure 5.1a-d show the front, back, side, and perspective view of the proposed UWB MIMO DRA. All optimized parameter values are shown in Table 5.1, and these values are obtained using the parametric sweep method in CST MWS V.16 software.

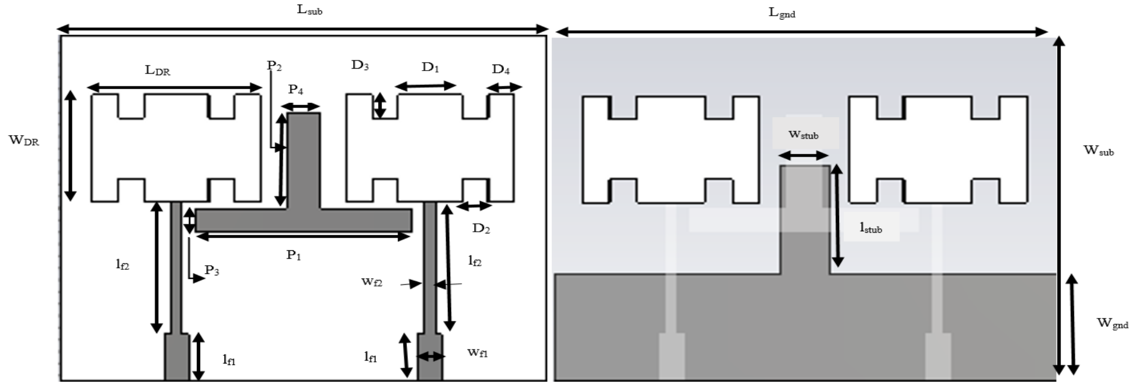

a b

Figure 5.1: Simulated two radiator element MIMO antenna; a). Top view, b). Back view

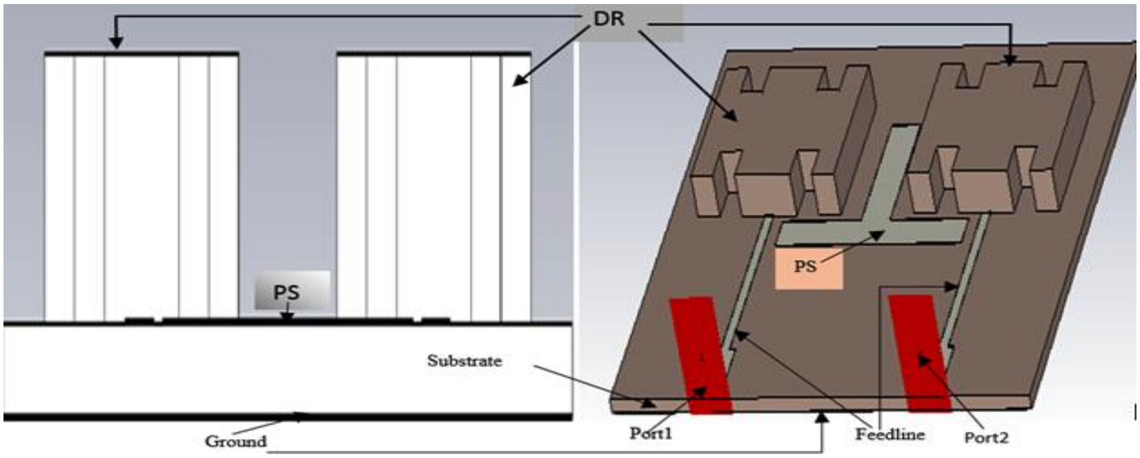

c d

Figure 5.1: Simulated two radiator element MIMO antenna; c). Side view d). Perspective view

Table 5.1 Optimized values of proposed MIMO DRA

Parameter	Values (mm)	Parameter	Values (mm)	Parameter	Values (mm)
L_{DR}	14	w_{stub}	3.5	D_3	2
W_{DR}	9	l_{f1}	4	D_4	2
L_{sub}	37.6	w_{f1}	1.9	P_1	16.8
W_{sub}	29	l_{f2}	11	P_2	7.9
L_{gnd}	37.6	w_{f2}	0.8	P_3	2
W_{gnd}	9	D_1	5	P_4	2.6
l_{stub}	9.2	D_2	2	h_{DR}	5

5.2.2 Design Procedure and Operation

The proposed antenna was designed and fabricated on an FR4 substrate with an electrical permittivity of 4.4, a thickness of 0.8 mm, tan = 0.025, and thermal conductivity = 0.3 W/K/m, with the optimized parametric values mentioned in Table 5.1. The DRA design procedure initially starts with selecting the Rogers RT 6010 sheet as the dielectric resonator for the MIMO antenna structure and choosing the appropriate electrical permittivity (10.2). Two rectangular sheet of dimensions 14×9 mm^2 of commercially available Rogers RT 6010 (thickness = 5 mm, tan δ = 0.0023, thermal conductivity = 0.78 w/k/m) is converted into the final optimized as rack-shaped DRs.

5.2.2.1 Design Steps and Simulated Results

The proposed DRA is designed and simulated using CST MWS V.16 software with mesh settings of 10 cells per lambda and open boundary conditions using the time domain solver. In ascending order, the four intermediate design phase structures of antennas are shown in Figure 5.2a–d as DRA1, DRA2, DRA3, and DRA4. Figure 5.3 shows the simulated S_{11}, S_{21}, axial ratio, and gain plots for each intermediate design step, simulated when a UWB DRA is developed in a MIMO configuration. The reflection (S11/S22) and transmission (S21/S12) parameters of a two-port network define the impedance bandwidth and EM coupling between the ports in a two-port network, these are shown in Figure 5.3a-b, respectively. The ability of an antenna to radiate more or less in any direction than a theoretical antenna is known as antenna gain. The gain of the proposed DRAs in the MIMO configuration is shown in Figure 5.3d. The evolution steps to obtain an optimized DRA geometry are explained below:

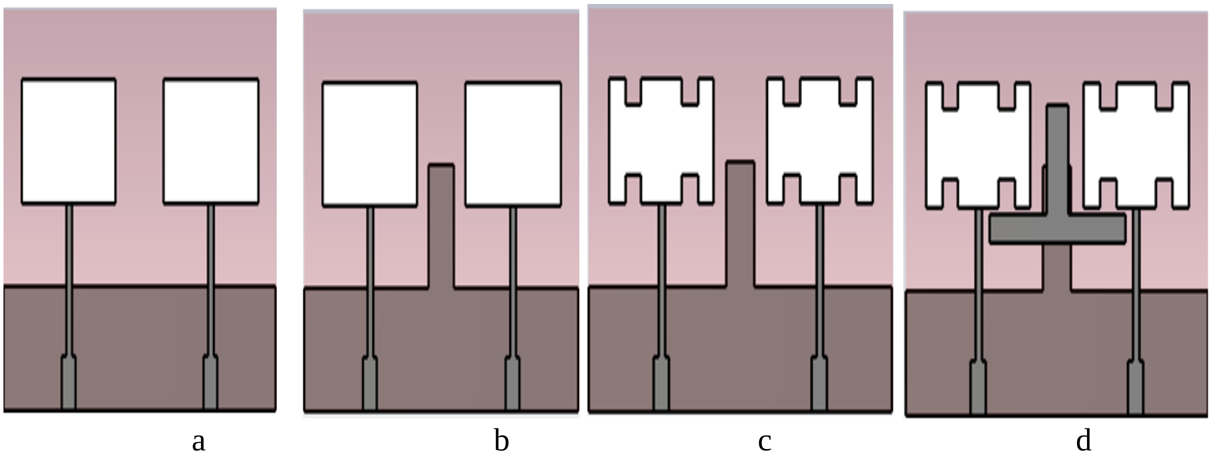

Figure 5.2: Top view of four antennas; a). DRA1 b). DRA2 c). DRA3 d). DRA4

- **DRA1:** The DRA1 structure, which consists of two rectangular DRAs fed using QWT feedline and a reduced ground as the first step of the proposed MIMO DRA, is shown in Figure 5.2a. The simulated S-parameters, gain, and axial ratio responses of DRA 1 geometry is shown in Figure 5.3. The two rectangular DRs are made up of Rogers RT6010 with the sizes of 14 mm × 9 mm × 5 mm each and are excited by a QWT feedline with an input impedance of 50 ohms. Figure 5.3a–b shows that DRA1 covers a frequency band from 5.09 to 10.1 GHz with an isolation of 12 dB between the radiating DRAs, and AR bandwidth (≤ 40.1 dB) of this geometry offers a linearly polarized (LP) antenna.
- **DRA 2:** DRA2 geometry is shown in figure 5.2 b. A ground stub is introduced between the two rectangular DRAs to achieve good impedance matching and improve the isolation

compared to DRA1 geometry. This DRA2 covers a frequency band from 4.9 to 10.1 GHz with improved isolation of 21 dB between the two DRAs, but it does not cover the desired UWB range, so the next step is to further improve the impedance bandwidth. But AR bandwidth (≤ 36.2 dB) of the antenna is considered LP.

- **DRA3:** In the DRA3 geometry shown in figure 5.2(b), the length of the two DRAs is notched to give them a rack shape. The DRA 3 geometry covers an operating frequency range of 4.8 to 10.28 GHz with the same isolation between antennas as in DRA2 geometry, as can be verified from Figure 5.3(a-b). AR bandwidth of DRA3 is improved with LP characteristics as compared to DRA1 and DRA2.
- **DRA4:** An inverted T-shaped parasitic strip between the two radiator elements improves the DRA4's impedance bandwidth. Figure 5.3 a-b, shows the simulated results for final DRA4 geometry with a black colored graph for S11/S22 and S12/S21 parameters, respectively, with good performance in terms of the reflection coefficient (≤-10 dB), AR bandwidth, transmission coefficient (≤-15.6 dB), and gain. It is observed that the two elements MIMO DRA4 provide the best results in terms of UWB frequency band, good isolation properties between the two DRAs, and better AR bandwidth (≤ 25.1 dB) for a frequency band from 3.54 to 10.89 GHz.

All intermediate steps of proposed DRA evolution results are shown in Table 5.2.

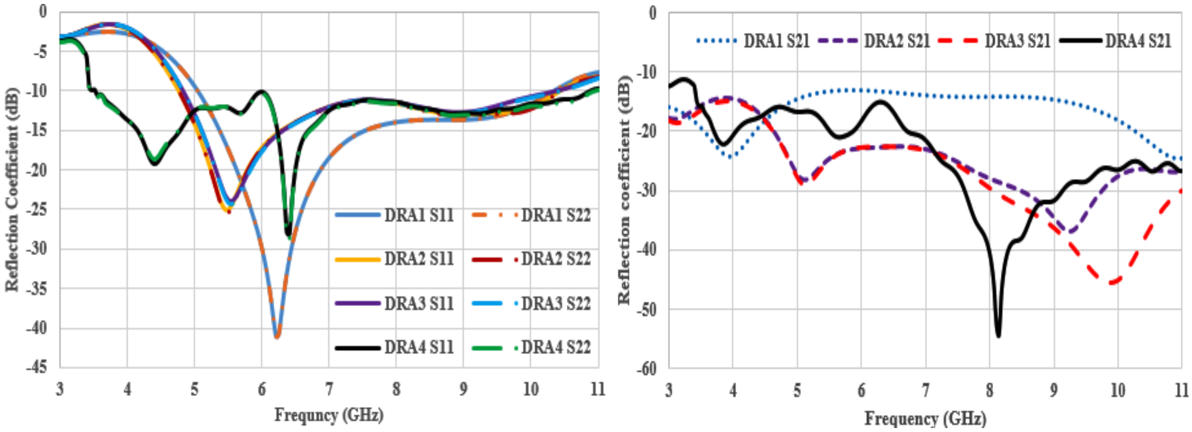

a b

Figure 5.3: S-Parameter's; a). S_{11} and S_{22}, b). S_{21}

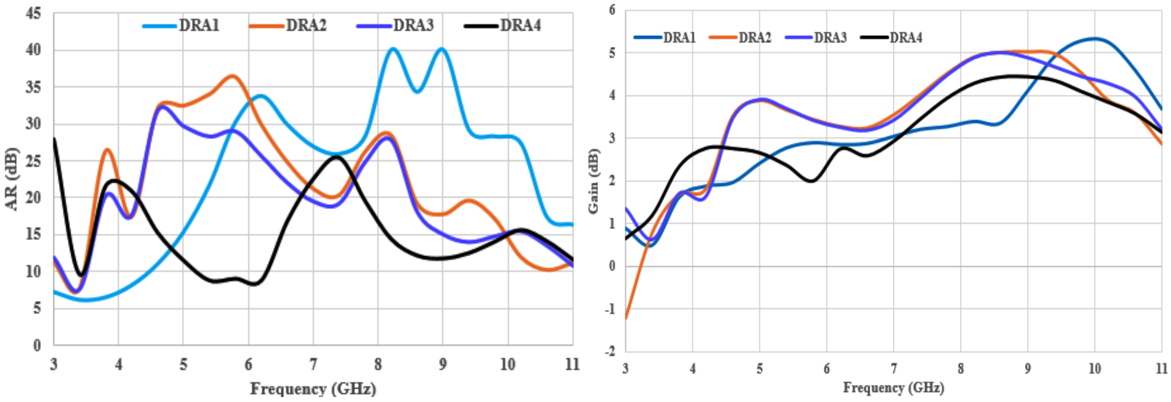

c d

Figure 5.3: c). Axial Ratio bandwidth, d). Gain

Table 5.2 Performance steps of all antennas simulated results

Antenna	**S_{11}, S_{22} dB**	**Impedance bandwidth %**	**S_{21} Isolation(dB)**	**Gain range (dB)**	**Axial ratio (dB)**
DRA1	5.09 to 10.1 GHz	66	12 to 26	2.1 to 5.4	6 to 41
DRA2	4.9 to 10.12 GHz	69.34	21 to 36	2.8 to 5.1	7.2 to 36.5
DRA3	4.8 to 10.28 GHz	72.67	21 to 46.1	3.1 to 5	7.1 to 33
DRA4	3.54 to 10.89 GHz	101.87	15.5 to 54.2	1.5 to 4.5	8.1 to 25.4

5.2.3 Field Modes of Compact Rack Shaped Two Element Based MIMO DRA

Resonant modes are used in RDRA to depict the radiating phenomena using E and H field patterns. These fields are displayed azimuthally within RDRA. An antenna's radiation characteristics can be predicted using knowledge of modes. These modes are categorized as TE or TM or HE, or HEM [109]. The first-order mode and higher-order modes of HEM_{mnp} are excited by the rack-shaped MIMO DRA stimulated by the QWT-type microstrip feedline [119][120][78]. Figures 5.4 to 5.6 show the simulated E-field configuration inside the rack-shaped DR at various frequencies. The proposed antennas operate in different modes, such as the fundamental and higher-order hybrid modes.

$$f_{HEM_{mnp}} = \frac{v}{2\pi\sqrt{\varepsilon_{reff}}}\sqrt{k_x^2+k_y^2+k_z^2} \tag{5.1}$$

$$\varepsilon_{reff} = \frac{H_{eff}}{\frac{h_{DR}}{\varepsilon_{DR}}+\frac{h_S}{\varepsilon_{sub}}} \tag{5.2}$$

$$H_{eff}=h_{DR}+h_S \tag{5.3}$$

$$k_z = \frac{\mathrm{p}\pi}{h_{\mathrm{DR}}}, \mathrm{k}_x = \frac{\mathrm{m}\pi}{L_{\mathrm{DR}}}, \mathrm{k}_y \tan\left(k_y \frac{W_{\mathrm{DR}}}{2}\right) = \sqrt{(\varepsilon_{\mathrm{eff}}\text{-}1)k_0^2\text{-}\mathrm{k}_y^2} \tag{5.4}$$

$$k_z = \frac{\mathrm{p}\pi}{h_{\mathrm{DR}}}, \mathrm{k}_y = \frac{\mathrm{n}\pi}{W_{\mathrm{DR}}}, \mathrm{k}_x \tan\left(k_x \frac{L_{\mathrm{DR}}}{2}\right) = \sqrt{(\varepsilon_{\mathrm{eff}}\text{-}1)k_0^2\text{-}\mathrm{k}_x^2} \tag{5.5}$$

Where k_0 denotes wavenumber in the free space, k_x, $k_{y,}$ and k_z are wavenumbers.

The resonant frequencies are calculated using Equation (5.1 to 5.5) at 7.3 GHz, 9.3 GHz, and 10.74 GHz. The electric field distribution on top of the DR surface is depicted in Figures 5.4 - 5.6 at different frequencies. Figure 5.4 a-c shows the HEM_{111} mode at 7.3 GHz in xy, xz, and yz planes, respectively. Similarly, Figure 5.5 a-c and Figure 5.6 a-c illustrate the HEM_{211} and HEM_{212} modes at 9.3 and 10.74 GHz, respectively. HEM_{111} mode exists as a fundamental mode as well as a dominant mode, and other modes are higher-order modes of the proposed **Rack Shaped UWB DRAs**.

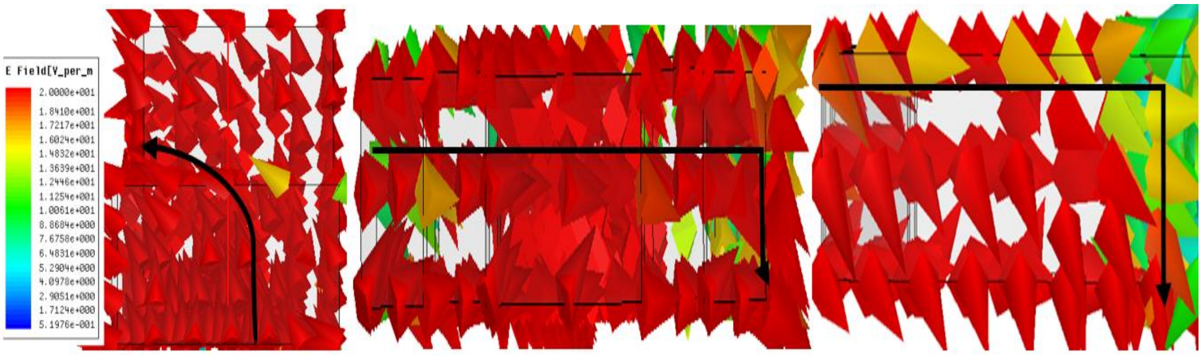

a b c

Figure 5.4 E-field on DR surface: HEM_{111} at 7.3 GHz; a). Front view (x-y), b). Bottom view (x-z), c). Side view (y-z)

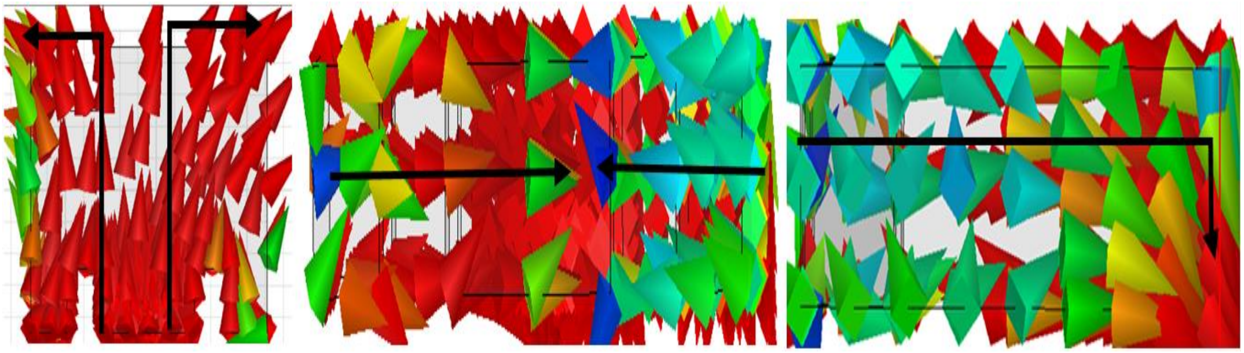

a **b** **c**

Figure 5.5 E-field on DR surface: HEM_{211} at 9.3 GHz; a). Front, b). Bottom view, c). Side view

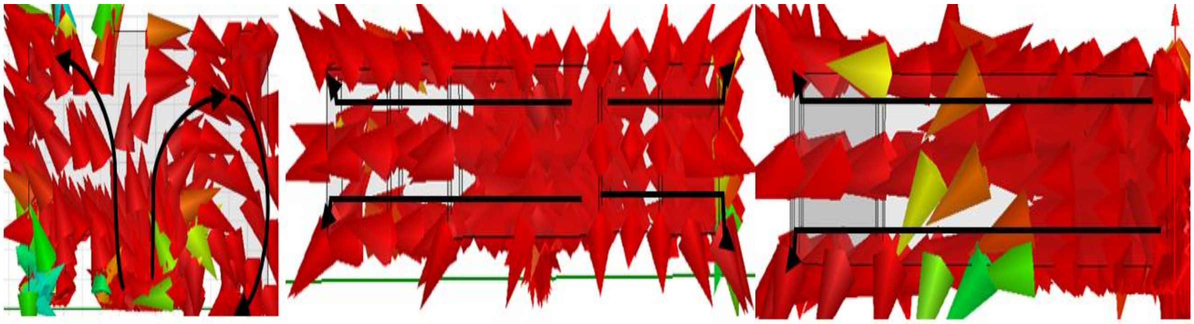

a b c

Figure 5.6: E-field on DR surface; HEM_{212} at 10.74 GHz; a). Front, b). Bottom view, c). Side view

5.2.4 Rack-shaped MIMO DRA Fabrication and Measurement of Results

The proposed rack-shaped MIMO DRA with optimized geometrical parameters is fabricated by printing the feed network on an FR4 substrate with electrical permittivity of 4.4 thickness equal to 0.8 mm and a tanδ of 0.0024 by using the wet etching technique. Two DRs of Rogers sheet (ε_{DR} = 10.2) were cut using manually and fixed on the Fr4 substrate using Araldite. Figure 5.7a shows the assembled antenna as front view with feedline, DRs, and T-shaped MPS. Figure 5.7b shows a back view with the modified ground layer having a stub etched on the bottom side of the substrate with two subminiature connectors (50 ohms) for exciting the DRAs for radiation. The fabricated rack-shaped MIMO DRA was tested for validation of S parameter results using KEYSIGHT (E5063A) vector network analyzer, operating in the frequency range from 9 KHz to 18 GHz for s11, s21, and group delay.

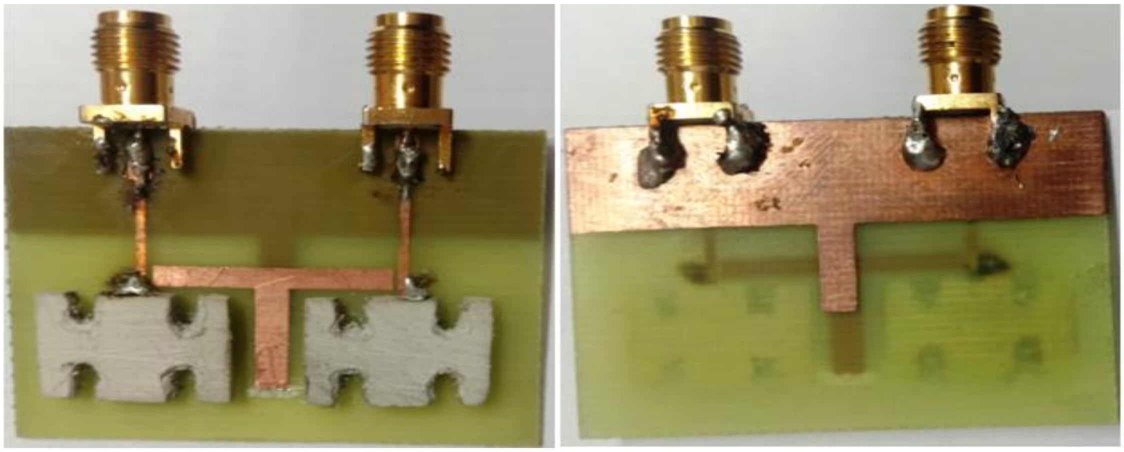

a b

Figure 5.7: Fabricated two radiator element MIMO antenna; a). Front view, b). Back view

Figure 5.8 a-b shows the comparison of simulated and measured S-parameters (S_{11} and S_{21}). Using MPS, the proposed UWB MIMO DRA achieves an impedance bandwidth of 101.87 %. Figure 5.8b illustrates that the MIMO antenna has good isolation and reasonable impedance matching over the entire UWB range of 3.54 to 10.87 GHz, as shown in Figure 5.8a. The transmission coefficient of the proposed MIMO DRA is reported to be less than -15.6 dB within the band, as shown in Figure 5.8b.

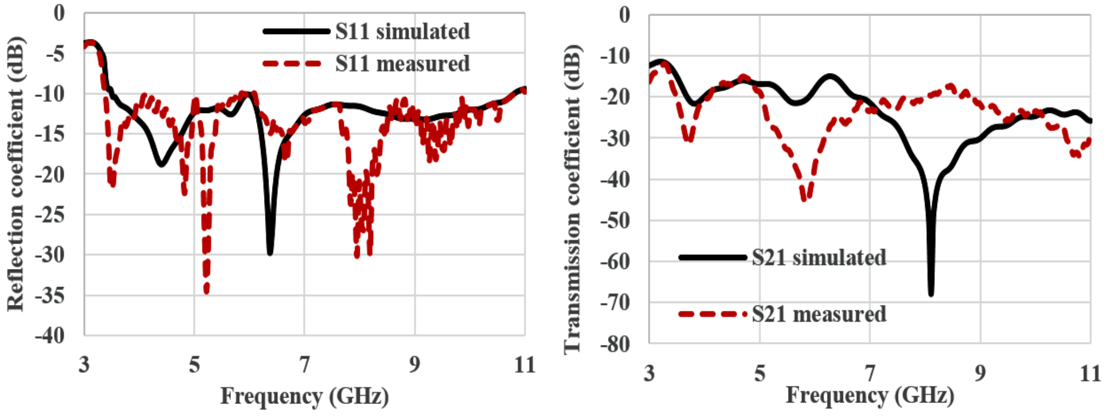

a b

Figure 5.8: Simulated and measured S- parameters; a). S_{11}, b). S_{21}

The performance of antennas in a MIMO configuration is judged by various essential performance parameters such as the envelope correlation coefficient (ECC), diversity gain (DG), total active reflection coefficient (TARC), and channel capacity loss (CCL) [121].

The simulated and measured ECC values are calculated by S-parameters using Equation (5.6), shown in Figure 5.9. ECC describes the correlation between different channels used at the transmitter and receiver side through a medium. In the existing UWB range, ECC values for the proposed MIMO DRA are less than 0.006, which is less than the allowable limit of 0.5. The DG of the MIMO DRA is calculated using Equation (5.7), as indicated by the orange and green colored graphs in Fig. 5.9. The proposed antenna's ECC and DG plots for comparison of simulated and measured results is shown in Figure 5.9.

$$\mathrm{ECC}^{n} = \frac{|S^{*}_{11}\ S_{12}+S^{*}_{21}\ S_{22}|^{2}}{(1-|S_{11}|^{2}-|S_{21}|^{2})\ (1-|S_{22}|^{2}-|S_{12}|^{2})} \tag{5.6}$$

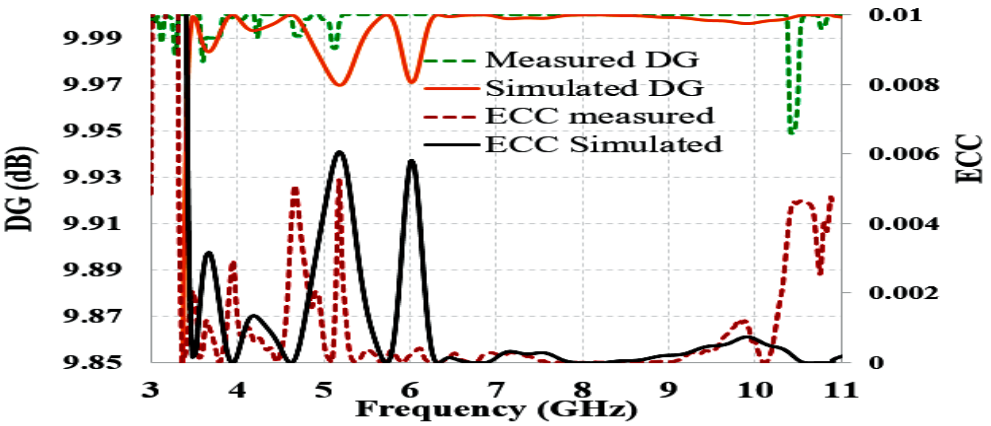

Figure 5.9: Simulated and calculated (measured) DG and ECC for MIMO antenna

$$DG^{n}=10\sqrt{(1-|0.99\ ECC^{n}|^{2})} \tag{5.7}$$

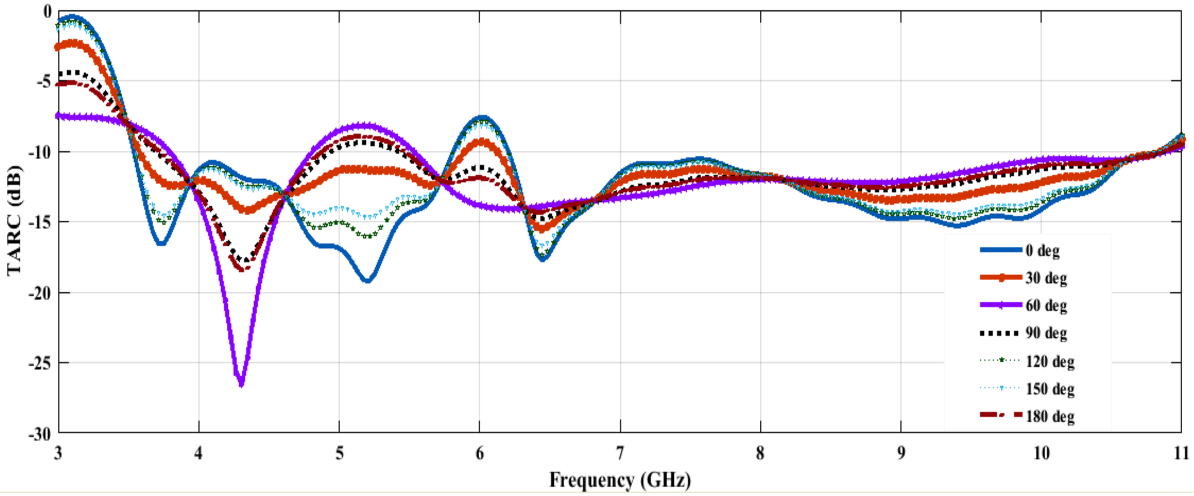

Figure 5.10 TARC diversity of MIMO antenna

Figure 5.10 shows the TARC of the proposed MIMO DRA. The Total Active reflection coefficient of the proposed MIMO DRA is calculated using Equation (5.8). TARC is a frequency-dependent function that also takes into account scan angle and tapering. For determining a multi-port antenna's frequency bandwidth and radiation performance.

$$\Gamma_{a}^{\mathrm{Trans}}=\sqrt{\frac{(|S_{11}+S_{12}e^{j\theta}|^{2}+|S_{21}+S_{22}e^{j\theta}|^{2})}{\sqrt{2}}} \tag{5.8}$$

where $\Gamma_{a}^{\mathrm{Trans}}$= total active reflection Coefficient , θ is the feeding phase of the input signal.

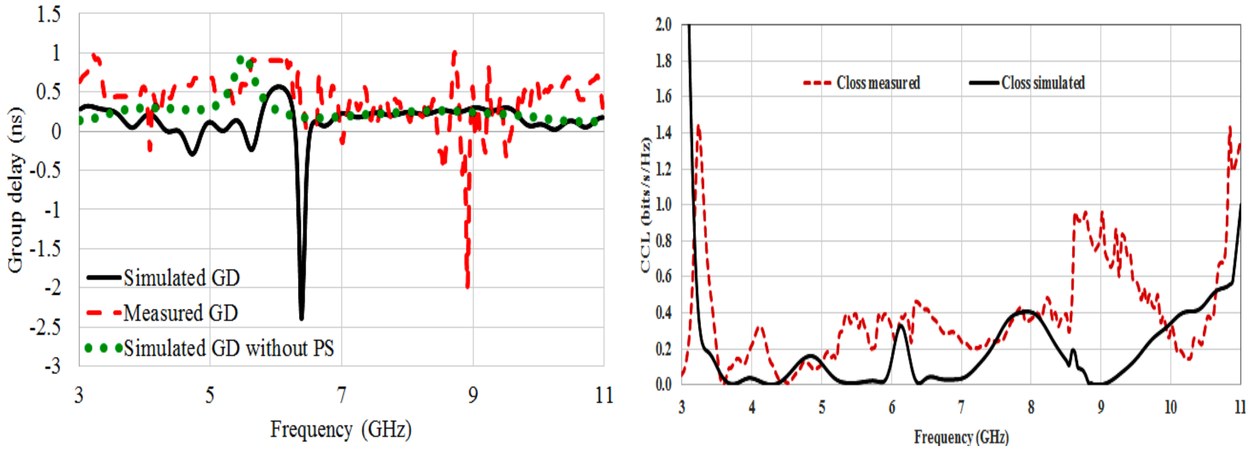

a b

Figure 5.11: Simulated and measured MIMO DRA results; a). Group Delay, b). Channel capacity loss (CCL)

The group delay (GD), as depicted in Figure 5.11a, is an important parameter in the antenna's time-domain analysis. Depending on the length of the path, whatever is most convenient. When the group delay is taken from the S-parameters, the frequency will vary until the network is an accurate measurement of the complete transmission line. The acceptable group delay for a MIMO configuration should be less than 5 nanoseconds (ns) [19]. The proposed DRA shows a GD of -2.45 ns to 1 ns, which means the GD is within the limit.

When analyzing the performance of a MIMO antenna array, the CCL is a crucial parameter. This technique demonstrates that good impedance matching and isolation between two antenna elements results in low CCL values. The allowed upper limit of CCL is 0.4 for a channel where transmission and reception is carried out using a MIMO antenna array. The CCL for the two-radiator element MIMO DRA is determined using Equation (5.9) and is shown in Figure 5.11b. The simulated results cover the frequency range of 3.54 to 10.88 GHz with a CCL of 0.4. The lower value of CCL is reported as high channel capacity and data rate. The remaining UWB range from 8.4 to 9.8 GHz is higher than 0.4, so CCL also gave less channel capacity in this band.

$$\text{CCL}=-\log_2 \det(\beta^n)$$

$$\beta^n = \begin{pmatrix} a_{11} & a_{12} \\ a_{21} & a_{22} \end{pmatrix}$$

$$a_{11}=1-(|S_{11}|^2 + |S_{12}|^2),\ a_{22}=1-(|S_{22}|^2 + |S_{21}|^2),\ a_{12}=-({S^*}_{11}\ S_{12}\ +\ {S^*}_{21}\ S_{12}),\ a_{21}=-({S^*}_{22}\ S_{21}\ +\ {S^*}_{12}\ S_{21}) \quad (5.9)$$

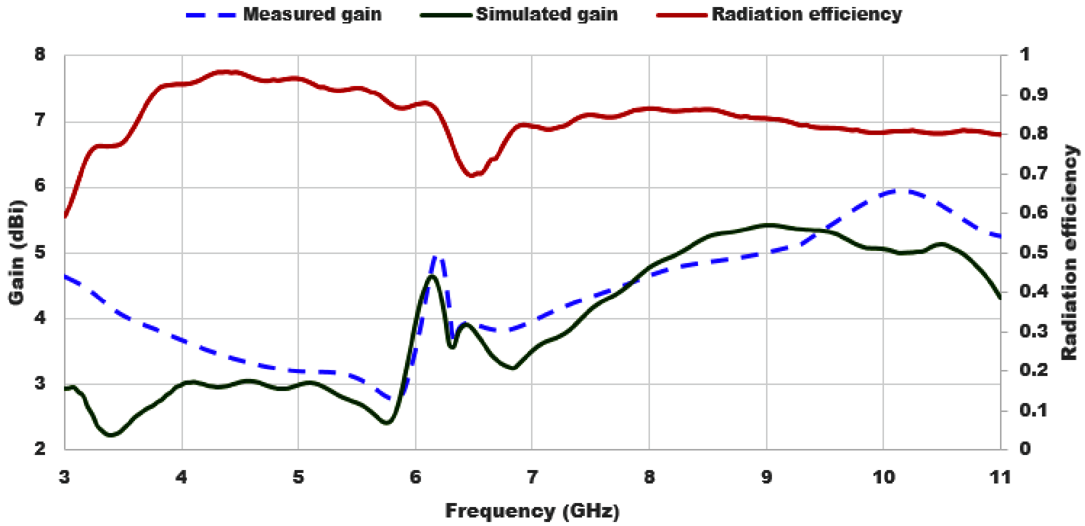

Figure 5.12: Gain and simulated Radiation efficiency concerning frequency

The gain and radiation pattern of the proposed antenna is measured using an anechoic chamber having an operating frequency range from 2 kHz to 18 GHz. This anechoic chamber requires a horn antenna with a gain of 12 dBi as a reference antenna to test the proposed antenna. For the anechoic pattern measurements, proposed radiators of MIMO DRA are set up for measurements by exciting port 1 and terminating port 2, and the process is repeated for port 2 excitation with port 1 termination. Consideration of these better diversity performances is reported. The simulated and measured gain of the antenna is shown in Figure 5.12.

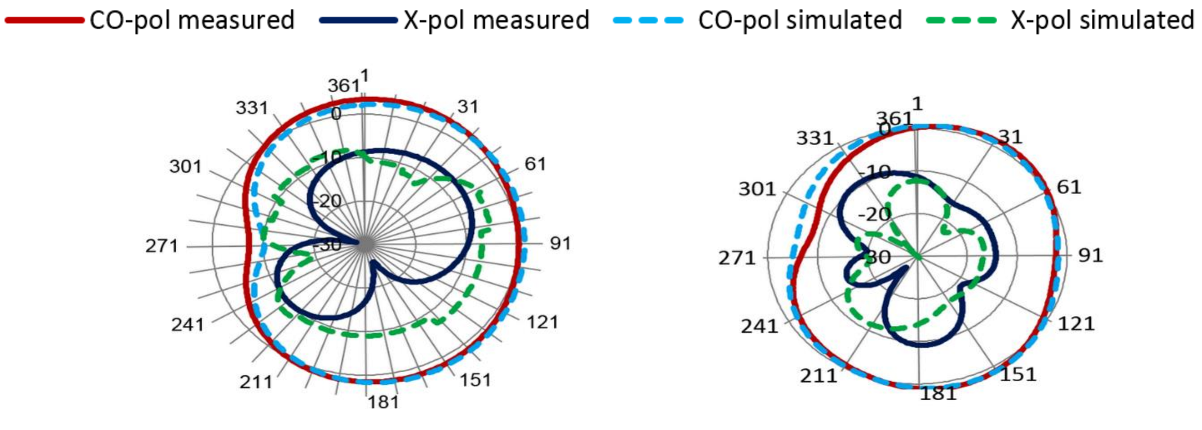

a b

Figure 5.13: Polar radiation pattern at; a). 4.3 GHz, b). 6.3 GHz

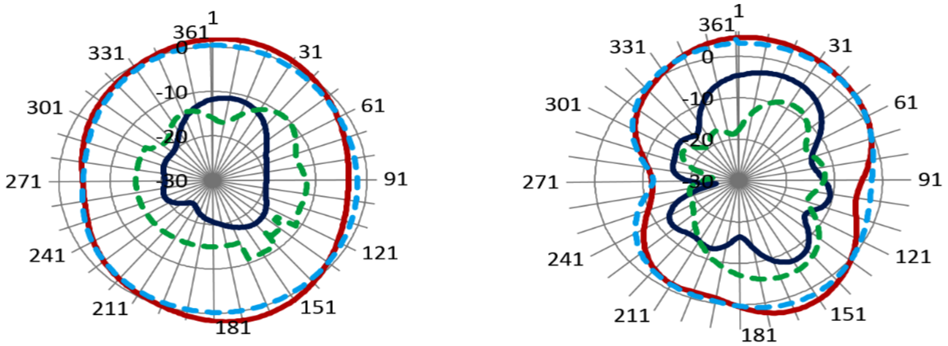

c d

Figure 5.13: Polar radiation pattern at; c). 8.4 GHz, d). 10.2 GHz

A rack-shaped MIMO antenna's omnidirectional radiation characteristics are depicted in Figure 5.13(a-d). The Co and cross-polarization patterns of the proposed MIMO DRA are shown at frequencies of 4.3, 6.3, 8.4, and 10.2 GHz. The DRAs in the proposed MIMO configuration show that the cross-polarization values of the proposed antenna are lower than the co-polarization values at most frequencies, indicating that the proposed antenna radiates effectively.

The next section of this chapter explains the proposed next MIMO DRA geometry with two DRAs as compact cross-shaped parasitic strip-based DRAs in a MIMO configuration for UWB operations.

5.3 Compact Cross-Shaped Parasitic Strip Based MIMO Dielectric Resonator Antenna

This section discusses the second DRA design used to meet the fourth objective of the proposed doctoral research work. A **compact cross-shaped parasitic strip-based MIMO DRA** is designed in a 2 x 2 MIMO configuration with improved isolation and impedance bandwidth within UWB operation as compared to the **Compact Rack Shaped Two Element Based MIMO** design presented in the previous section of this chapter. The proposed DRA in MIMO configuration has two rectangular-shaped radiator elements of Rogers RT 6010 (permittivity = 10.2) with a cross-shaped metallic parasitic strip (MPS) pasted on top of the DRs, and a stub-based partial ground plane with a scissor-shaped DGS, with an inverted T-shaped MPS, make up the proposed MIMO antenna structure.

5.3.1 Proposed DRA Geometry and Design in a MIMO Configuration

The proposed MIMO DRA consists of two DRs having electrical permittivity (ε_{DR} = 10.2) of Rogers RT 6010 used as the radiator elements, shown in Figure 5.14 a & c - d. The optimized dimensions of the rectangular DRs are 15mm × 9mm × 5mm; these are excited by a QWT microstrip feedline ($l_{fd} \times w_{fd}$, $l_{fd2} \times w_{fd2}$). An inverted T-shaped MPS is placed between the two radiators to improve the isolation between the antennas while radiation. DR and feedline are printed on the top of the substrate (FR4) with the dimension of 37.6 mm × 29 mm × 0.8 mm, and a partial ground plane (37.6 mm × 9 mm) with a stub and scissor-shaped DGS slot is printed on the bottom side of the FR4 substrate. The electrical permittivity of FR4 substrate is 4.4 with $\tan\delta$ of 0.0024. A ground stub ($l_{st} \times w_{st}$) is added for improving the isolation and impedance matching. A T-shaped MPS (M_1, M_2, M_3, M_4), ground stub, and scissor-shaped slot are used to improve the impedance bandwidth for the UWB range, shown in Figure 5.14 b. Cross-shaped MPS of copper (P_{s1}, P_{s2}) is designed and fixed on the top of DR layers to improve the impedance bandwidth of MIMO DRA. All optimized parametric values of all DRA parts are mentioned in Table 5.4.

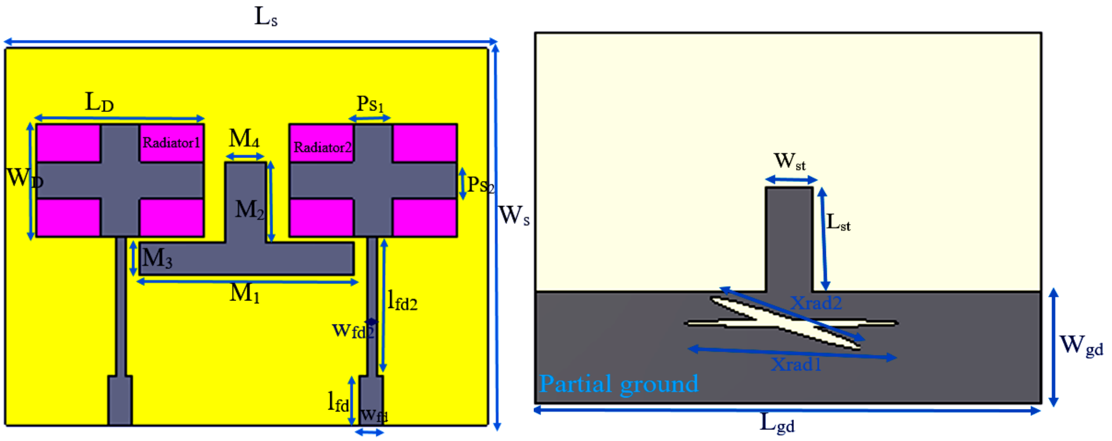

a **b**

Figure 5.14: Cross-shaped MPS-based MIMO DRA; a. Top view, b. back view

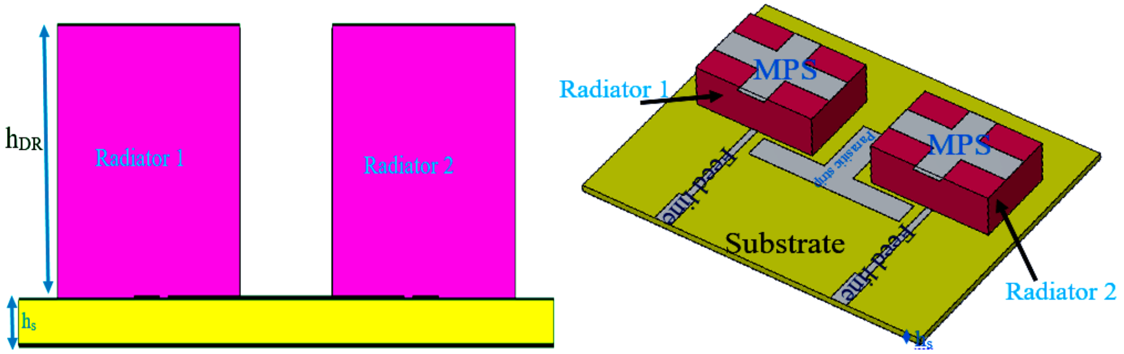

c **d**

Figure 5.14: Cross-shaped MPS-based MIMO DRA; c. Side view, d. perspective view

Table 5.3 Optimized parameters of Cross-shaped MPS based MIMO antenna

Parameter	Values (mm)	Parameter	Values (mm)	Parameter	Values (mm)	Parameter	Values (mm)
L_D	15	w_{st}	3.5	Yrad1	2	Ps1	3
W_D	9	l_{fd}	4	Yrad2	2	Ps2	3
L_s	37.6	w_{fd}	1.9	M_1	16.8	P_{SL}	15
W_s	29	l_{fd2}	11	M_2	6.5	P_{SW}	9.5
L_{gd}	37.6	w_{fd2}	0.8	M_3	2.5	h_s	0.8
W_{gd}	9	Xrad1	5	M_4	3.2		
l_{st}	9.2	Xrad2	2	h_{DR}	5		

5.3.2 Design Procedure of the proposed DRA and its operation

The proposed DRA is designed and simulated using CST MWS V.16 software with mesh settings of 10 cells per lambda and open boundary conditions using the time domain solver. The proposed antenna was designed and fabricated on an FR4 ($\varepsilon_s = 4.4$, h= 0.8 mm, and tan $\delta = 0.025$, $\sigma = 0.3$ W/K/m) substrate. The DRA design process starts with the selection of a Rogers RT 6010 sheet as the dielectric resonator, which is then mounted on FR4 substrate for the MIMO antenna structure. Two rectangular sheets of dimensions 15 × 9 × 5 mm^3 of commercially available Rogers RT 6010 (tan $\delta = 0.00023$, thermal conductivity = 0.78 w/k/m) are used as radiators in the proposed MIMO DRA configuration. The design steps that were followed for the final MIMO DRA design are mentioned below:

Evolution steps of the Proposed DRA in MIMO Configuration: The five main evolution steps of the proposed Cross-shaped MPS-based MIMO DRA (DRA1 to DRA5) are shown in Figure 5.15. The grey and light green color represents the metal part of the proposed antenna that is placed on the FR4 substrate. DRA1 geometry shows a rectangular DR with partial ground, and it excites a wideband of operation.

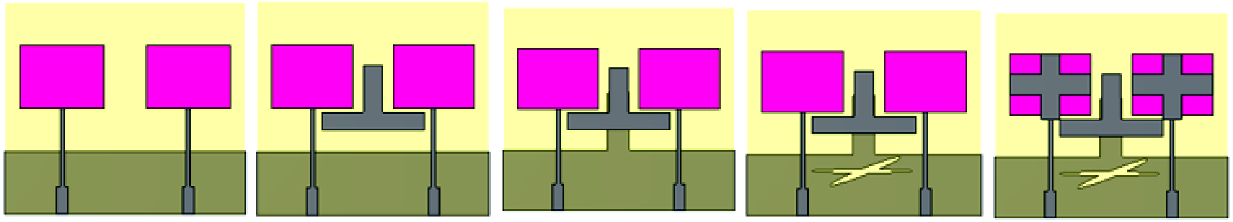

DRA1 DRA2 DRA3 DRA4 DRA5

Figure 5.15: Steps performance of six antennas

- **DRA1:** Mention the design equation used for the calculation of rectangular DRA parameters. And the dimensions of DRAs also. The simulated S-parameters, gain, and group delay response for the DRA1 structure is shown in Figure 5.15. These DRs are fed with a P-type transformer type feedline that offers an input impedance of 50 ohms to the proposed antenna. The DRA1 covers a frequency range from 5 to 10.2 GHz with an isolation of 13.2 dB between the two DRs, during radiation. The Peak gain reported for this geometry can be seen in Figure 5.5c as 6.19 dBi at 9.3 GHz. Figure 4.6d shows that the group delay of DRA1 is reported of -1 to 1 ns within the prespecified limit.
- **DRA2:** The DRA2 geometry, shown in Figure 5.15, is aimed to enhance performance over the DRA1. The DRA2, which is created by adding a MPS with dimensions of M_1 to M_4 on the same plane as the DRs, provides a wideband of operation from 4.9 to 10.38 GHz but has poor isolation between antennas during radiation. The gain and group delay for this geometry are the values listed in Table 5.5, as shown in Figure 5.16 c–d. The DRA3 geometry is proposed as the next evolution step for the final geometry.
- **DRA3**: The DRA3 geometry, shown in Figure 5.15, is aimed to enhance performance within the UWB range as compared to the DRA2 geometry. It is employed by adding a ground stub of dimensions ($l_{st} \times w_{st}$) in the partial ground, and this ground stub is easily coupled with MPS to improve the performance of the antenna. DRA3 reports a UWB operation from 3.56 to 10.63 GHz with an isolation of 15.6 dB. Table 5.5 shows the S_{11}, isolation, gain, and group delay for DRA3 geometry.
- **DRA4**: The DRA4 geometry, shown in Figure 5.15, is aimed to enhance performance over the DRA3. The DRA4 is created by modifying the ground layer of the DRA3 to a scissor-shaped DGS from the partial ground plane and reported impedance bandwidth of 102.3% with isolation of 17.8 dB between DRAs. Figure 5.16 depicts the antenna performance results, with the respective values listed in Table 5.5.
- **DRA5**: The DRA5 geometry, shown in Figure 5.15, is designed to enhance performance over the DRA4. The DRA5 uses a cross-shaped MPS on top of the DR's Surface to improve the isolation between the DRAs to a level of around 20 dB with a 10 dB impedance bandwidth of 104.6%. Figure 5.16c shows the GD with an acceptable limit (≤5 ns), and Figure 5.16d shows the gain of all five DRA geometries. All intermediate antenna results are presented in Table 5.5. It has been observed that DRA5 shows the optimized results in

terms of impedance bandwidth, gain, and isolation properties between DRs during radiation.

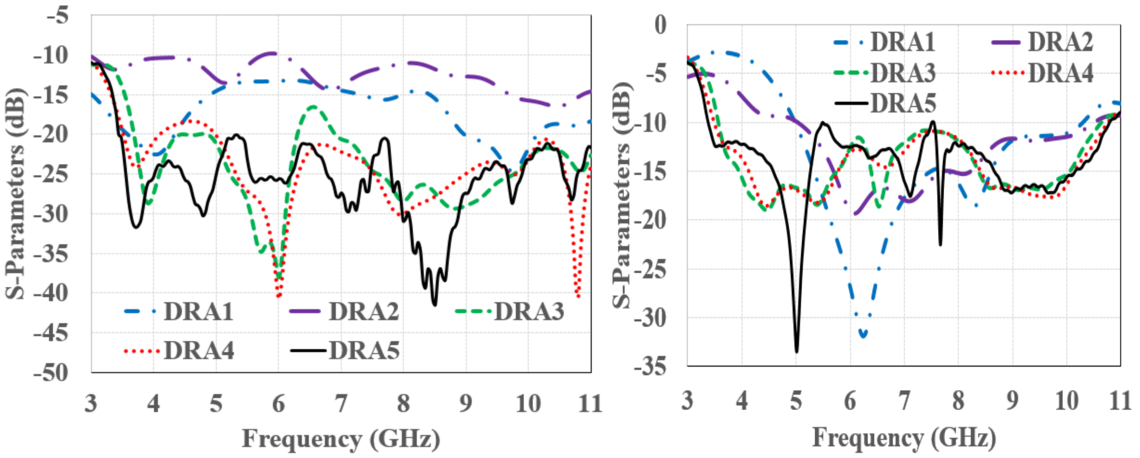

a b

Figure 5.16: Cross-shaped MPS-based MIMO antenna step results; a. S_{11}, b. S_{21}

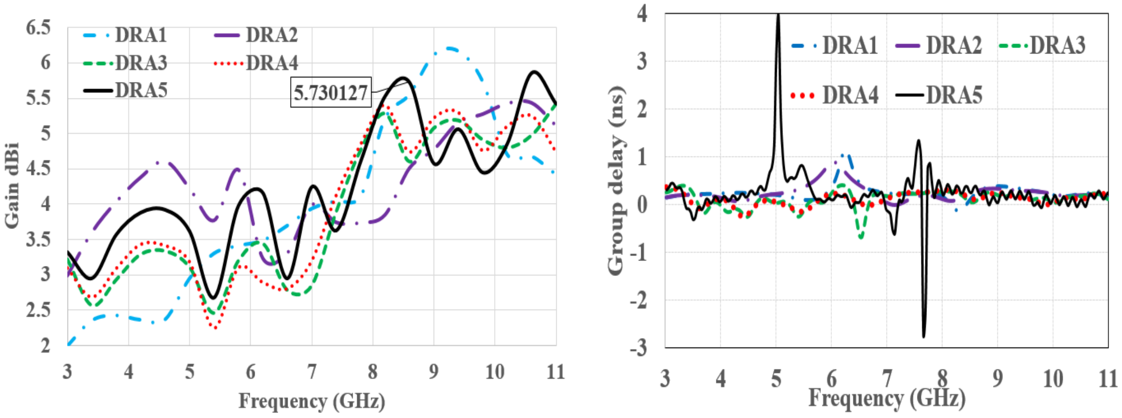

c d

Figure 5.16 Cross-shaped MPS-based MIMO antenna step results; c. Gain, d. Group delay

Table 5.4: Performance comparison of all intermediate DRA 1- DRA5 geometries of Cross-shaped MPS based MIMO DRA

Antenna	**Frequency in GHz**	**Impedance bandwidth %**	**≥Isolation (dB)**	**Gain range (dB)**	**Group delay (ns)**
DRA1	5 to 10.2	68.4	13.2	3 to 6.1	1.1 to -0.2
DRA2	4.9 to 10.38	71.7	9.9	3 to 5.4	0.85 to 0
DRA3	3.56 to 10.63	99.7	15.4	2.4 to 5.2	0.28 to 0.84
DRA4	3.48 to 10.75	102.3	17.8	2.2 to 5.3	0.15 to -0.37

DRA5	3.3 to 10.88	104.6	20	2.7 to 5.7	4 to -2.8

5.3.3 Validation of DRA Modes of Operation

The DRA radiators are excited by the QWT feedline and show the fundamental and higher-order modes. Observing the modes by E-field distribution is shown in Figure 5.18. The proposed antenna operates first and second-order modes at 4.4 GHz, 8.3 GHz, and 10.8 GHz.

$$f_{HE_{mnp}} = \frac{v}{2\pi\sqrt{\varepsilon_{eff}}}\sqrt{k_x^2+k_y^2+k_z^2} \tag{5.10}$$

$$\varepsilon_{eff} = \frac{H_{eff}}{\frac{h_{DR}}{\varepsilon_{DR}}+\frac{h_S}{\varepsilon_s}} \tag{5.11}$$

$$H_{eff} = h_{DR} + h_S \tag{5.12}$$

$$k_x = \frac{m\pi}{L_D}, k_y = \frac{n\pi}{W_D}, k_z \tan(k_z \frac{h_{DR}}{2}) = \sqrt{(\varepsilon_{eff}-1)k_0^2 - k_z^2} \tag{5.13}$$

Where k_0 denotes free space wavenumber, k_x, k_y, and k_z are wavenumbers with respect to x, y, z directions.

Equations (5.10 to 5.13) are used for calculating the fundamental DRA mode of operation at 4.4 GHz. The electric field distribution on DR is shown in Figure 5.17. Figure 5.17 a-c show the generation of $HE_{11\delta}$ mode at 4.4 GHz along the front, right, and top views of DRA in the fundamental mode of operation. Similarly, Figures 5.17 d-f and 5.17 g-i show the generation of $HE_{21\delta}$ and $HE_{12\delta}$ modes at frequencies of 8.3 and 10.8 GHz, respectively. $HE_{11\delta}$ mode exists as a fundamental mode, and other higher-order modes have been generated that help in widening the impedance bandwidth of the proposed MIMO DRA [122] [123].

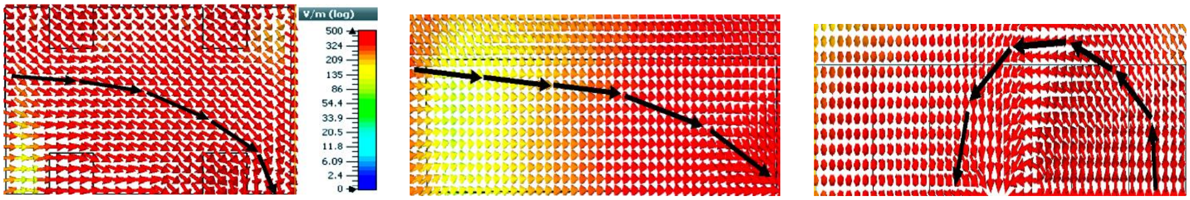

a. Front b. Right c. Top

Figure 5.17 a-c: E-field distribution on DR surface at 4.4 GHz

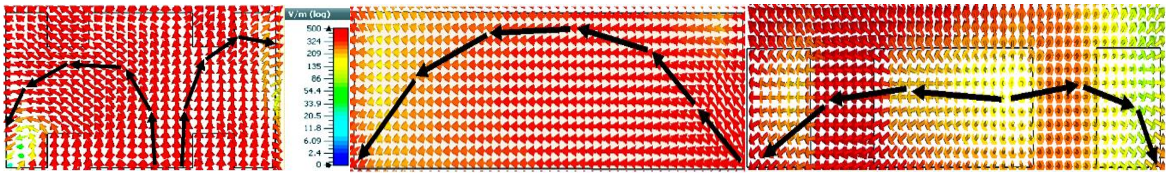

d. Front e. Right f. Top

Figure 5.17 d-f: E-field distribution on DR surface at 8.3 GHz

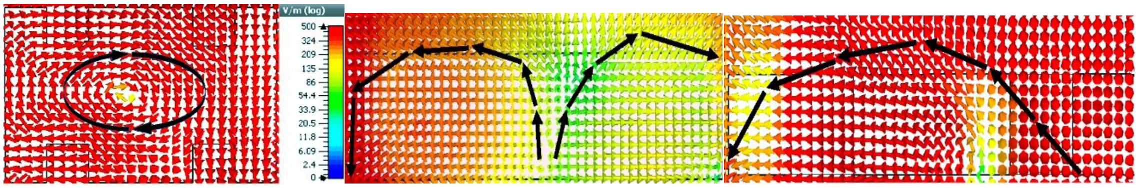

g. Front h. Right i. Top

Figure 5.17 g-i: E-field distribution on DR surface at 10.8 GHz

5.3.4 Fabrication of the proposed Cross-Shaped Parasitic Strip Based MIMO DRA and Validation of Simulated Results

Figure 5.18 a-b shows the front and back view of the proposed MIMO DRA after Fabrication. The metallic parts are etched on the FR4 substrate (electrical permittivity of 4.4) surface using a wet etching process.

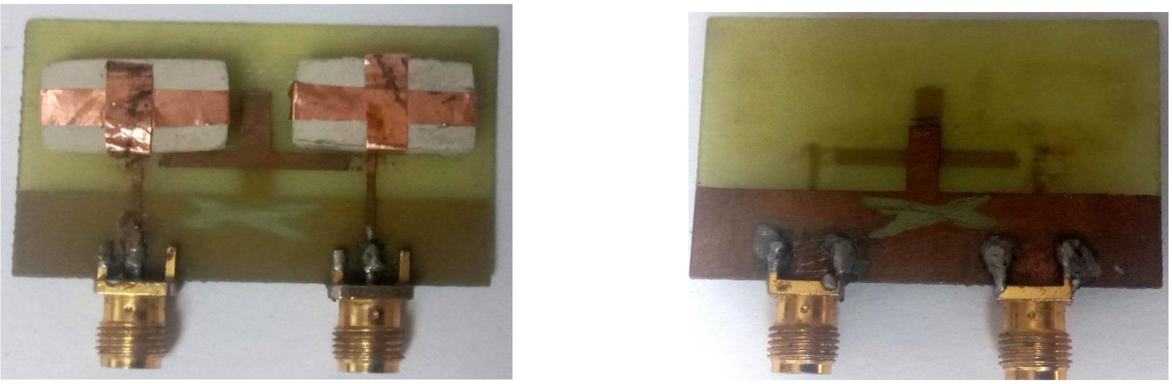

a b

Figure 5.18: Fabricated two radiator element MIMO antenna; a). Front view, b). Back view

The Rogers RT 6010 with a height of 5mm is cut using manually from hex blades or other tools. The dimensions of DRs are placed on the FR4 substrate. The bottom layer of FR4 has a partial ground with scissor-shaped DGS and a stub. Feedline and inverted T-shaped MPS were etched on the top of the substrate. The cross-shaped metallic strip is deposited on the two DRs.

The fabricated UWB MIMO DRA is tested using VNA to compare the simulated and measured S-parameters (S_{11} and S_{21}) and shown in Figure 5.19 a–b. Figure 5.19b reports high isolation (greater than 20 dB) between the two DRAs in the MIMO configuration. The stub and cross-shaped MPS allow the proposed DRAs to cover a frequency band from 3.3 to 10.8 GHz (simulated) and 3.4 to 10.8 GHz (measured), as in Figure 5.19a.

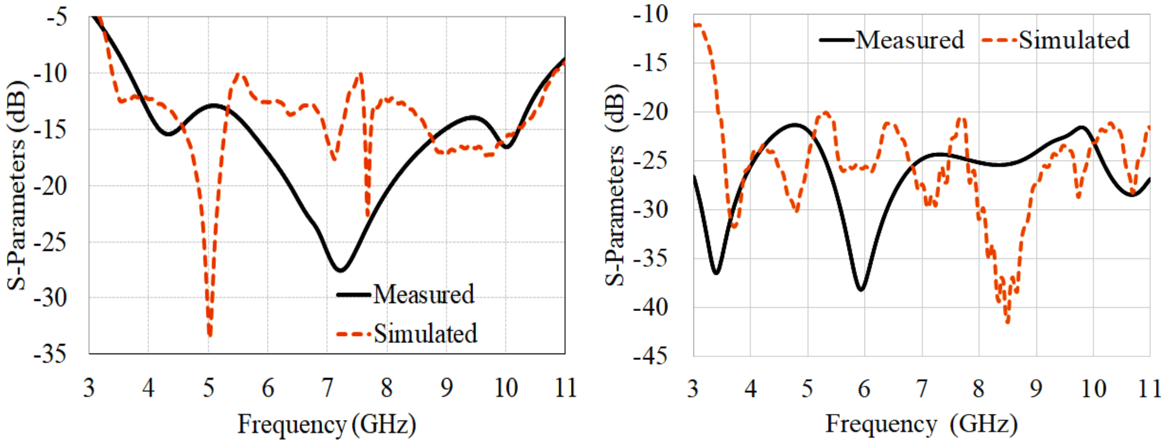

a b

Figure 5.19: Simulated and measured; a). S_{11}, b). S_{21}

Various performance parameters like the ECC, DG, and CCL are used to evaluate the MIMO DRA performance. The simulated and calculated (using measured S-parameters) ECC curve using Equation (5.6) is shown in Figure 5.20. ECC for the proposed MIMO DRA is ≤ 0.006 in the exciting UWB range of operation (the acceptable limit of ECC is ≤ 0.5). The antenna's DG is calculated using (5.7) and gives the best result related to MIMO parameters.

$$ECC^{n} = \frac{\left| \oiint_{\Omega} [\vec{E}_1(\theta,\phi) \cdot \vec{E}_2^{*}(\theta,\phi)] d\Omega \right|^2}{\oiint_{\Omega} |\vec{E}_1(\theta,\phi)|^2 d\Omega \,.\, \oiint_{\Omega} |\vec{E}_2(\theta,\phi)|^2 d\Omega} \tag{5.14}$$

Where, $\vec{E}_1(\theta,\phi)$ and $\vec{E}_2^{*}(\theta,\phi)$ are the far field E filed strength of antennas for the radiator1 and radiaor2.

The DG of the proposed MIMO DRA is calculated using equation 5.7. A measured and simulated DG of the antenna was reported with good agreement. This antenna also reported a high diversity gain (DG) of 9.99 dB, as shown in Figure 5.20.

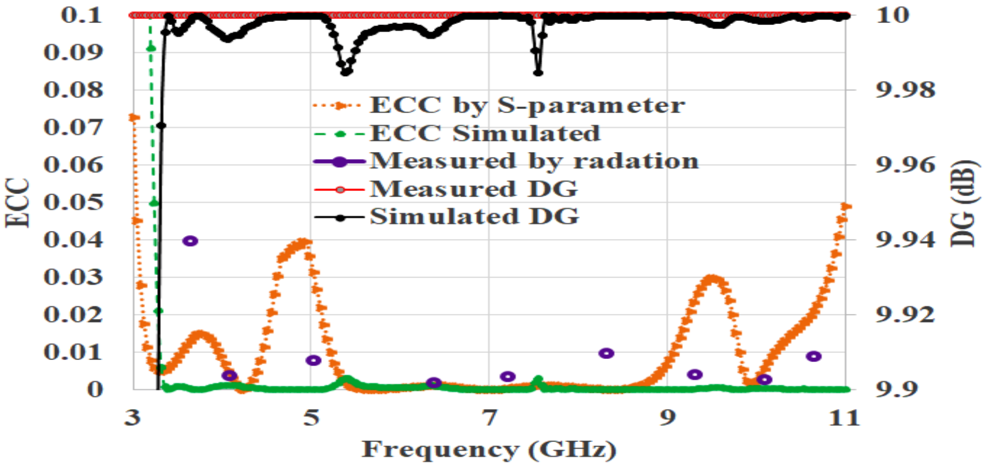

Figure 5.20 Cross-shaped MPS based MIMO antenna: Simulated and calculated (measured) DG and ECC

The CCL evaluates the performance of the MIMO UWB DRA. It is the acceptable limit of data loss over a given communication channel. For two radiator element MIMO antenna, CCL is calculated by Equation (5.9). Figure 5.22a shows that the simulated results cover a frequency range from 3.3 to 10.8 GHz for a CCL less than 0.4. However, the measured curve shows a covered CCL band from 3.5 to 10.7 GHz, with CCL less than 0.4, as in Figure 5.21a. The proposed MIMO DRA reports a high channel capacity and high data rate. Figure 5.21b shows gain and radiation efficiency. The measured and simulated peak gain is 6 dBi, and the peak simulated radiation efficiency is 96.6%.

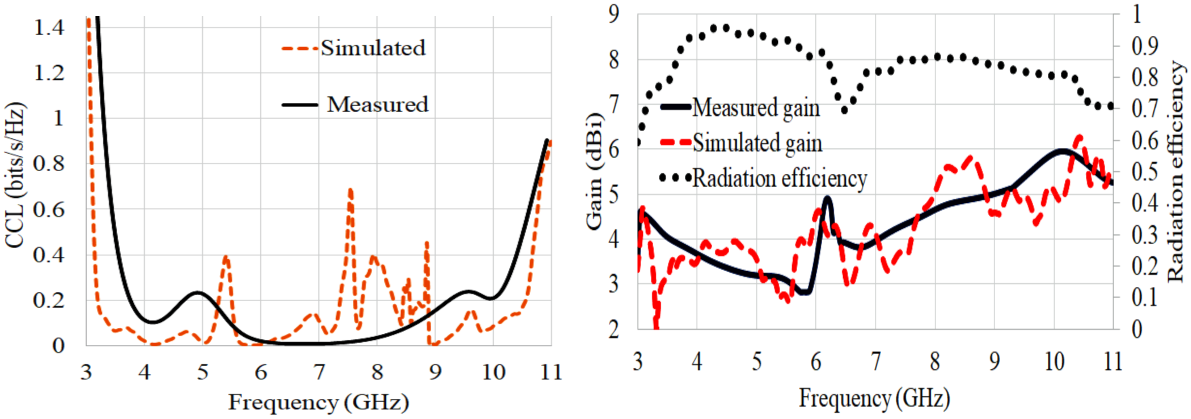

a b

Figure 5.21: Simulated and measured; a). Channel capacity loss, b).Gain and Radiation efficiency

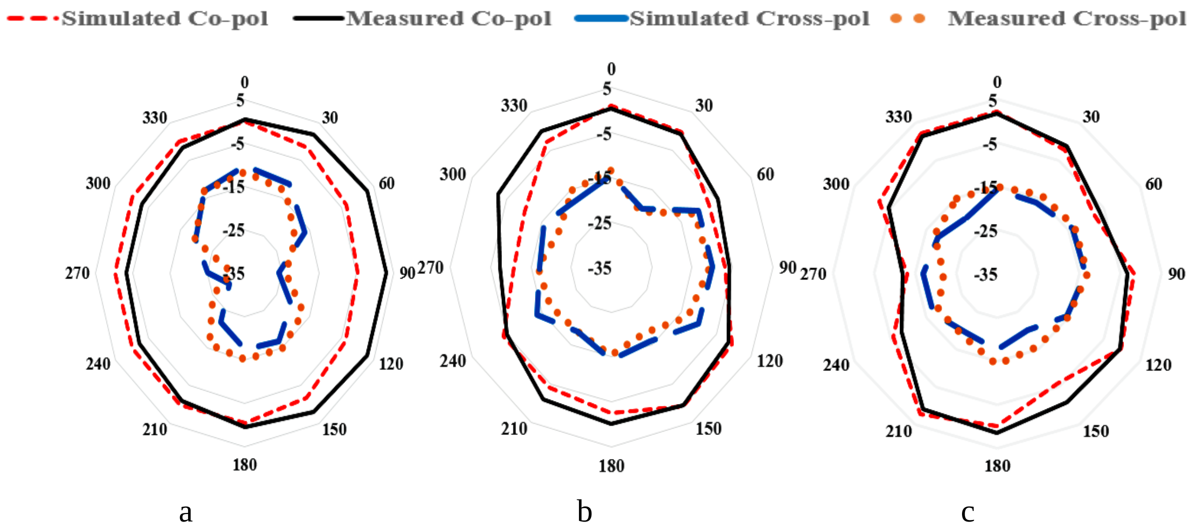

Figure 5.22: Co and cross radiation pattern at; a). 4.4 GHz, b). 8.3 GHz, c). 10.8 GHz

The radiation characteristics of Cross-shaped MPS-based MIMO DRA are shown in Figure 5.22. The co and cross-polarization of the proposed MIMO DRA are reported at 4.4, 8.3, and 10.8 GHz. At most of the frequencies, it can be observed that the cross-polarization values are less than the co-polarization values, and the antenna radiates efficiently.

5.4 Conclusion

This chapter presents the research work done to achieve the fourth objective of the proposed doctoral research work. Two DRAs are designed, optimized, fabricated, and tested in a MIMO configuration. The first design of a rack-shaped DR antenna with a MIMO configuration excited by a QWT-type feedline has been presented for UWB applications. The proposed antenna has two rack-shaped radiator elements, and an inverted T-shaped MPS. Further, it also includes a partial ground plane with a stub for better impedance matching and improved UWB characteristics. This proposed antenna achieves a wide impedance bandwidth of 101.87% (3.52 GHz to 10.89 GHz) with good isolation (over 15.6 dB) between the two DRs. The desired MIMO parameters of the MIMO DRA were reported as an ECC ≤ 0.0059, high diversity gain ≥ 9.94dB, and good transmission coefficient ≤ -15.6 dB.

In the second design, cross-shaped MPS-based MIMO DRA was excited by a QWT-type feedline for UWB operations. The proposed antenna has two rectangular DR elements having a partial ground with the stub, an inverted T-shaped MPS between the DRS, and two cross-shaped MPS on top of the DRs. These techniques improve the impedance bandwidth with high isolation (≥20dB).

Further, it also includes a partial ground plane with DGS (scissor-shaped slot) for improved impedance bandwidth. It achieves UWB range from 3.3 to 10.8 GHz (104.8 %) for high data rate applications. With a low ECC, high diversity gain, and a transmission coefficient of -20 dB, the antenna's MIMO properties make it a strong choice for high data rate UWB applications.

CHAPTER 6

CONCLUSION AND FUTURE SCOPE

6.1 Conclusions

This chapter summarizes the results of the research carried out in the thorough simulation, fabrication and experimental testing of the parameters and characteristics of dielectric resonator antennas (DRAs). Devices that integrate numerous communication standards into a single condensed lightweight system are also in high demand, mainly for breakthroughs in signal processing and improvements in the wireless communications industry. For a variety of wireless applications, UWB antennas are needed. As a result, new communication systems with small size, wideband, and UWB operation have attracted wide attention for multimode wireless communication applications. Demand for better wireless devices that can handle multiple systems, technologies and services drives the research described in this thesis.

At microwave, millimeter, and higher frequencies, DRAs perform as efficient radiators reducing surface wave losses and metal losses, which have the advantageous characteristics of being lightweight, low profile, less complex, and easy to fabricate. DRAs can be developed into a compact size and easily converted into various shapes. For the application of UWB operation, extensive research is going on, which mainly focuses on enhancing the electrical and mechanical features of DRAs and designing them with good bandwidth and gain. Considering the gains achieved by combining such antennas, research was undertaken to develop a constructive design that would allow DRA to be performed with UWB operations. Some flaws in the performance of DRAs must be addressed in order to be used effectively in communication systems. The size of the DRA is too large for some applications that require compaction.

In first chapter, the UWB DRAs, their criteria, the motivation and goal of the study effort are all discussed. Then a literature review research on UWB DRA covering the frequency range of 3.1 to 10.6 GHz, which the FCC classified as unlicensed spectrum was discussed in chapter 2. In order to find better ways of developing working antennas in UWB operation, various articles were referred to, several thesis, including several websites, helped to determine the objectives of doctoral research work.

The literature review shows the significance of this study as well as the uniqueness of the present work. The literature study also showed research gaps in existing DRAs for UWB operations, this is the primary motivation of the thesis. The problem description, research objectives, and the complete approach required to carry out the procedures are discussed. Some new design techniques for the production of DRAs with UWB operations have been acknowledged as the main objectives of the thesis. The material utilized in the design and research methods for the deployed radiator element of various antenna characteristics, along with its simulation, fabrication, and experimental verification are all detailed.

DRAs configurations that meet the antenna design criteria are simulated, fabricated and tested in this doctoral research work to achieve the best impedance matching, widen impedance bandwidth, good gain, and compact antenna size for UWB operations. The following flow chart is a summary of the doctoral research work:

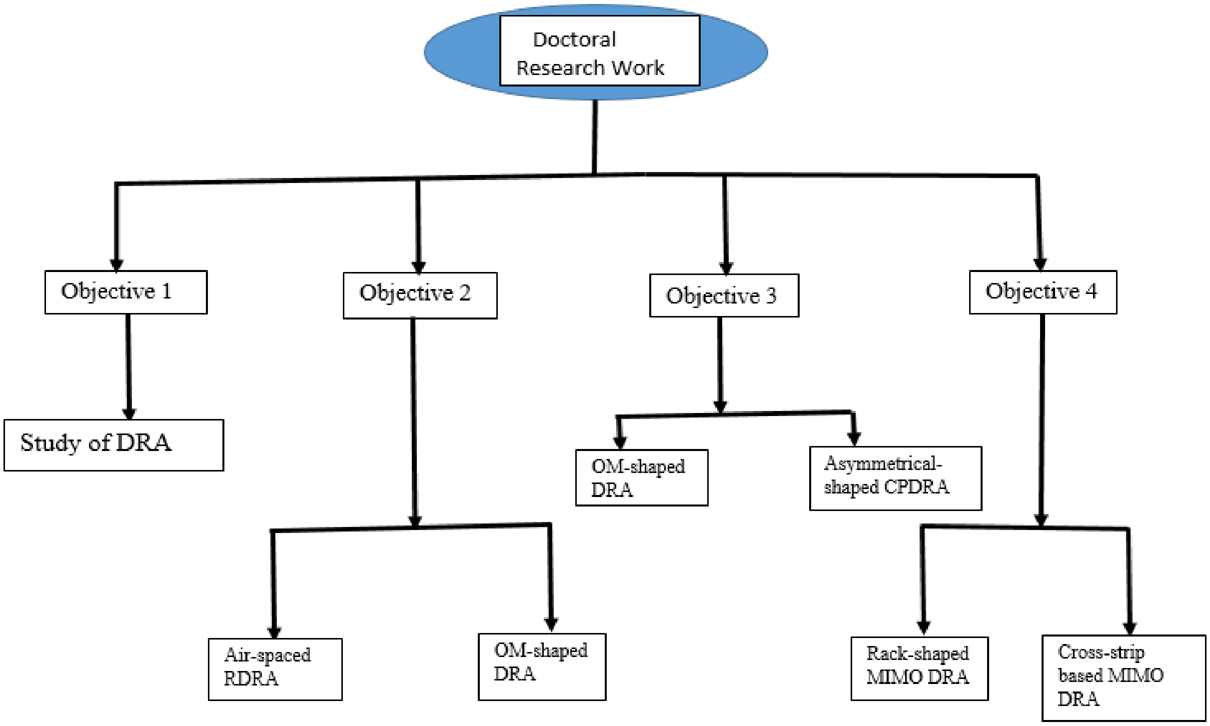

Figure 6.1: Flow Chart of Research Objectives

In chapter 3, an air-spaced UWB DRA is excited by a QWT feedline, which covers frequencies from 3.1 to 10.4 GHz. The proposed DRA consists of DR with an electric permittivity of 9.8, a QWT feedline, and a modified ground plane. The ground is suitably modified to enhance the impedance bandwidth with good impedance matching. In order to improve the performance of DRA, cylindrical DR is cut from solid rectangular shape DR. This approach has the ability to increase DRA's gain. Table 6.1 compares the simulated and measured values.

Table 6.1: Comparison simulated and measured results of Air-spaced DRA

Design	Frequency Band (GHz)	Impedance Bandwidth	Gain	Modes
Air-spaced RDRA	3.28 - 10.4 GHz Simulated	104.09%	7.2 dB	$\mathrm{TE}_{11\delta}$, $\mathrm{TE}_{22\delta}$ TE_{231} $\mathrm{TE}_{33\delta}$
	3.2 - 10.21 GHz Measured	103.86%	7 dB	

Chapter 4 has two designs and in the first design, the proposed OM-shaped DRA is fed using a P-type microstrip feedline with a metallic conformal strip offering an input impedance of 50 ohms for UWB characteristics (3.1 to 11.3 GHz) with elliptical polarization (6 to 11.1GHz). The total size of the DRA is 50 × 40 × 4.87 mm^3. The antenna shows a measured ($S_{11} \leq -10$ dB) impedance bandwidth from 3.88 to 9.05 GHz and 10 to 11.5 GHz and a gain of 7.68 dB. The UWB performance is obtained from the proposed DRA by merging higher-order modes, $\mathrm{TE}_{211,}$ and $\mathrm{TE}_{221,}$ of the antenna's operation at 7.2 and 10GHz and using a defected ground structure. The proposed DRA shows the generation of orthogonal modes of TE_{221}^{x}, $\mathrm{TE}_{221}^{y,}$ and TE_{211}^{x} and TE_{211}^{y} on the DRA surface at 6.5, 7.2, 8.35, and 10GHz, respectively. Since the magnitude of the E field component at the two orthogonal modes is different, the DRA shows an elliptically polarized behaviour for a frequency band from 6 to 11.1 GHz. The simulated and measured results of OM-shaped DRA are shown in Table 6.2.

In the second design, a compact asymmetric structured DR is designed, simulated, and fabricated for CP UWB operations. The antenna used two DR blocks with asymmetric height excited by the QWT feedline. An F-shaped metallic strip is added in the ground plane to obtain simulated AR bandwidth of 63.8% and measured AR bandwidth of 43.7% in the frequency range from 6.4 to 12.4 GHz for circularly polarized DRA. These attractive performances make the present design suitable for CP UWB systems. The simulated and measured results of asymmetric structured DRA are shown in Table 6.2.

Table 6.2: Comparison simulated and measured results of OM-shaped and Stacked Asymmetric-shaped DRA

Design	Frequency Band (GHz)	Impedance Bandwidth	Gain	Axial Ratio Bandwidth	Modes
OM-shaped DRA	3.14 to 11.4 GHz Simulated	8.26 GHz and 112%	7.68dB	5.1 GHz (6 to 11.1 GHz)	TE_{111}, TE_{211}, and TE_{221}
	3.8 to 9.05 GHz and 10 to 11.5 GHz Measured		7.6 dB		
Asymmetric-shaped DRA	6.4 to 12.4 GHz Simulated	6 GHz and 63.8%	6.01 dBi	6 GHz (6.4 to 12.4 GHz), 63.8%	$TE_{\delta 11}$ and $TE_{\delta 13}$
	5.9 to 11.8 GHz Measured	66.7%	5.6 dBi	5.8 to 6.1 GHz (2.52 %) and 6.9 to 10.9 GHz (43.7 %)	

Chapter 5 has two designs to cover the fourth objective of doctoral research work. In the first design, a UWB MIMO rack-shaped DRA excited by a transformer-type microstrip feedline has been proposed for UWB applications. It achieves the wider impedance bandwidth of (3.52 GHz to 10.89 GHz) 101.87 %, 3.52 to 4.0 GHz covering partial S, whole C, and X bands with high data rate applications. The proposed antenna has two rack-shaped radiator elements, an inverted T-shaped parasitic strip, along improving impedance bandwidth. Further, it also includes a partial ground plane with a stub for better impedance matching and improved isolation for UWB operations. The desired MIMO parameters of the antenna with low ECC ≤ 0.0059, high diversity gain ≥ 9.94dB, and transmission coefficient ≤ -15.6 dB make it a strong candidate for UWB applications. The simulated and measured results of Rack-shaped DRA are shown in Table 6.3.

A UWB cross-shaped MPS-based MIMO DRA is excited by a transformer-type microstrip feedline for UWB applications in the second design. The proposed antenna has two DR elements, a ground stub, an inverted T-shaped MPS, two cross-shaped MPS, along with improved impedance bandwidth and isolation. Further, it also includes a partial ground plane with DGS (scissor-shaped slot) for better impedance matching and improved impedance bandwidth. MIMO parameters of the antenna have been presented low ECC ≤ 0.0059, high diversity gain ≥ 9.98dB, and transmission coefficient ≤ -20dB, which make it a strong candidate for UWB applications with a high data rate. The simulated and measured results of cross-shaped MPS-based MIMO DRA are shown in Table 6.3.

Table 6.3: Comparison simulated and measured results of Rack-shaped and Cross-strip based MIMO Rectangular DRA

Design	Frequency Band (GHz)	Impedance Bandwidth	Isolation (dB)	Modes
Rack-shaped DRA	3.5 to 10.89 GHz Simulated	7.37 GHz, 101.87%	≥ 15.6 dB	HEM_{111}, HEM_{211}, HEM_{212}
	3.5 to 10.8 GHz Measured	101 %	≥ 15.9 dB	
Cross-strip based MIMO Rectangular DRA	3.3 to 10.88 GHz Simulated	7.51 GHz, and 104.6 %	≥ 20 dB	$HE_{11\delta}$, $HE_{21\delta}$, and $HE_{12\delta}$
	3.5 to 10.8 GHz Measured	101 %	≥ 21.2 dB	

This thesis work describes the objectives of doctoral research work to design, simulate, and fabricate the high gain DRA, EP/CP DRA, and MIMO DRA for UWB operations. Subsequently, some ideas are suggested for future work to achieve UWB DRA with compact size and platform easy operation for various applications in wireless communications.

6.2 Future Scope

Although in this research work, an extensive study has been done to design, simulate, and fabricate DRA for UWB operations. Various case studies have been included in the research work to understand better the operation of dielectric resonator antennas having various sizes, such as cylindrical, rectangular, and typical structures. Still, some topics have not been covered in the research work and can be explored in the future.

- With numerous DRA geometries such as spherical, rectangular, hemispherical, triangular, hexagonal, and many more geometries for ultra-wideband, wideband, and narrowband operations, there is tremendous scope in this research area.
- In this research, DRAs have been used to generate circularly/elliptically polarized EM waves utilizing metallic strips and a feeding mechanism based on the DRA structure (single or multiple). Other approaches for generating circularly polarized waves include dual feeding the DRA with two feed lines, the specific geometry of DRA, and edge feeding DRAs with truncated corners.
- In this thesis, the DRAs were designed with good gain, high efficiency, good isolation, low ECC, and they can be also improved further using various enhancement approaches.
- The use of electromagnetic metamaterials, metasurfaces [124] and reflectors for enhancing the performance of the dielectric resonator antenna characteristics. Further, chiral metamaterials can be used in DRAs to achieve circular polarization in the UWB range. These UWB DRAs can be used for 5G and IoT applications.

REFERENCES

[1] P. Kumar and Sumit, “Review Paper on Development of Mobile Wireless Technology,” *J. Phys. Conf. Ser.*, vol. 1979, no. 1, 2021, doi: 10.1088/1742-6596/1979/1/012024.

[2] E. Ezhilarasan and M. Dinakaran, “A Review on Mobile Technologies: 3G, 4G and 5G,” *Proc. - 2017 2nd Int. Conf. Recent Trends Challenges Comput. Model. ICRTCCM 2017*, pp. 369–373, 2017, doi: 10.1109/ICRTCCM.2017.90.

[3] K. Siwiak and D. McKeown, “Appendix A: Excerpts from the FCC First Report and Order,” *Ultra-Wideband Radio Technol. (eds K. Siwiak D. McKeown)*, 2004, doi: https://doi.org/10.1002/0470859334.app1.

[4] ITU-R, *Recommendation ITU-R SM.1755-0: Characteristics of ultra-wideband technology*, no. 2006. 2006.

[5] R. S. Kshetrimayum, “An introduction to UWB communication systems,” *IEEE Potentials*, vol. 28, no. 2, pp. 9–13, 2009, doi: 10.1109/MPOT.2009.931847.

[6] C. A. Balanis, *Antenna Theory Analysis and Design*. John wiley & sons, 2005.

[7] D. M. Pozar, *Microwave Engineering*. John wiley & sons., 1998.

[8] J. D. Kraus, R. J. Marhefka, and A. S. Khan, *Antennas and wave propagation*. Tata McGraw-Hill Education, 2006.

[9] H. G. Schantz, “A brief history of UWB antennas,” *2003 IEEE Conf. Ultra Wideband Syst. Technol. UWBST 2003 - Conf. Proc.*, no. April, pp. 209–213, 2003, doi: 10.1109/UWBST.2003.1267834.

[10] H. Huang, K. Nieman, P.-Y. Chen, M. Ferrari, Y. Hu, and D. Akinwande, “Properties and applications of electrically small folded ellipsoidal helix antenna,” *IEEE Antennas Wirel. Propag. Lett.*, vol. 11, pp. 678–681, 2012.

[11] D. Guha and C. Kumar, “Microstrip Patch versus Dielectric Resonator Antenna Bearing All Commonly Used Feeds: An experimental study to choose the right element,” *IEEE Antennas Propag. Mag.*, vol. 58, no. 1, pp. 45–55, 2016, doi: 10.1109/MAP.2015.2501231.

[12] S. K. K. Dash and T. Khan, “Recent developments in bandwidth improvement of dielectric resonator antennas,” *Int. J. RF Microw. Comput. Eng.*, vol. 29, no. 6, pp. 1–17,

2019, doi: 10.1002/mmce.21701.

[13] D. Kajfez and P. Guillon, *Dielectric Resonators*. Norwood,1986.

[14] K. Wakino, “Recent development of dielectric resonator materials and filters in japan,” *Integr. Circuits Wirel. Commun.*, no. July 2012, pp. 501–518, 1998, doi: 10.1109/9780470544952.ch7.

[15] J. K. Plourde and C. L. Ren, “Application of Dielectric Resonators in Microwave Components,” *IEEE Trans. Microw. Theory Tech.*, vol. 29, no. 8, pp. 754–770, 1981, doi: 10.1109/TMTT.1981.1130444.

[16] R. K. Mongia and P. Bhartia, “Dielectric resonator antennas—a review and general design relations for resonant frequency and bandwidth,” *Int. J. Microw. Millimeter-Wave Comput. Eng.*, vol. 4, no. 3, pp. 230–247, 1994, doi: 10.1002/mmce.4570040304.

[17] S. Keyrouz and D. Caratelli, “Dielectric Resonator Antennas: Basic Concepts, Design Guidelines, and Recent Developments at Millimeter-Wave Frequencies,” *Int. J. Antennas Propag.*, vol. 2016, 2016, doi: 10.1155/2016/6075680.

[18] R. D. Richtmyer, “Dielectric resonators,” *J. Appl. Phys.*, vol. 10, no. 6, pp. 391–398, 1939, doi: 10.1063/1.1707320.

[19] M. Thumm, W. Kasparek, D. Wagner and A. Wien, "Reflection of {\rm TE}_{0{n}}{\rm TE}_{0{n}} Modes at Open-Ended Oversized Circular Waveguide," in IEEE Transactions on Antennas and Propagation, vol. 61, no. 5, pp. 2449-2456, 2013, doi: 10.1109/TAP.2013.2243098.

[20] G. Sinclair, “The Transmission and Reception of Elliptically Polarized Waves,” *Proc. IRE*, vol. 38, no. 2, pp. 148–151, 1950, doi: 10.1109/JRPROC.1950.230106.

[21] G. Varshney, V. S. Pandey, and R. S. Yaduvanshi, “Axial ratio bandwidth enhancement of a circularly polarized rectangular dielectric resonator antenna,” *Int. J. Microw. Wirel. Technol.*, vol. 10, no. 8, pp. 933–941, 2018, doi: 10.1017/S1759078718000764.

[22] U. Ullah, M. F. Ain, and Z. A. Ahmad, “A review of wideband circularly polarized dielectric resonator antennas,” *China Commun.*, vol. 14, no. 6, pp. 65–79, 2017, doi: 10.1109/CC.2017.7961364.

[23] A. Petosa and A. Ittipiboon, “Dielectric resonator antennas: A historical review and the

current state of the art," *IEEE Antennas Propag. Mag.*, vol. 52, no. 5, pp. 91–116, 2010, doi: 10.1109/MAP.2010.5687510.

[24] G. Bharti, K. R. Jha, G. Singh, and R. Jyoti, "Design of azimuthally periodic wedge-shaped circular ring bandpass frequency selective surface using transmission-line method," *Wirel. Pers. Commun.*, vol. 85, no. 3, pp. 1411–1428, 2015.

[25] S. K. K. Dash, T. Khan, and Y. M. M. Antar, "A state-of-art review on performance improvement of dielectric resonator antennas," *Int. J. RF Microw. Comput. Eng.*, vol. 28, no. 6, 2018, doi: 10.1002/mmce.21270.

[26] M. A.Ittipiboon, R.K.Mongiaz, Y.M.M.Antar, P. Bhartia, & Cuhaci, "An Integrated Rectangular Dielectric Resonator Antenna," *Proc. IEEE Antennas Propag. Soc. Int. Symp.*, vol. 2, pp. 604–607, 1993.

[27] J. Kumar and N. Gupta, "Bandwidth and Gain Enhancement Technique for Gammadion Cross Dielectric Resonator Antenna," *Wirel. Pers. Commun.*, vol. 85, no. 4, pp. 2309–2317, 2015, doi: 10.1007/s11277-015-2906-0.

[28] J. Malik, A. Patnaik, and M. V. Kartikeyan, "Novel printed MIMO antenna with pattern and polarization diversity," *IEEE Antennas Wirel. Propag. Lett.*, vol. 14, pp. 739–742, 2015, doi: 10.1109/LAWP.2014.2377784.

[29] D. K. A. A. KlSHK, B. AHN, "Broadband Stacked Dielectric Resonator Antennas," *Electron. Lett.*, vol. 25, no. 18, pp. 1232–1233, 1989.

[30] T. H. Chang and J. F. Kiang, "Bandwidth broadening of dielectric resonator antenna by merging adjacent bands," *IEEE Trans. Antennas Propag.*, vol. 57, no. 10 PART 2, pp. 3316–3320, 2009, doi: 10.1109/TAP.2009.2029372.

[31] M. Khalily, M. K. A. Rahim, and A. A. Kishk, "Bandwidth enhancement and radiation characteristics improvement of rectangular dielectric resonator antenna," *IEEE Antennas Wirel. Propag. Lett.*, vol. 10, pp. 393–395, 2011, doi: 10.1109/LAWP.2011.2144558.

[32] W. W. Li and K. W. Leung, "Omnidirectional circularly polarized dielectric resonator antenna with top-loaded alford loop for pattern diversity design," *IEEE Trans. Antennas Propag.*, vol. 61, no. 8, pp. 4246–4256, 2013, doi: 10.1109/TAP.2013.2262072.

[33] A. Petosa and S. Thirakoune, "Rectangular dielectric resonator antennas with enhanced gain," *IEEE Trans. Antennas Propag.*, vol. 59, no. 4, pp. 1385–1389, 2011, doi:

10.1109/TAP.2011.2109690.

[34] G. Varshney, R. S. Yaduvanshi, and V. S. Pandey, “Gain and bandwidth controlling of dielectric slab rectangular dielectric resonator antenna,” *12th IEEE Int. Conf. Electron. Energy, Environ. Commun. Comput. Control (E3-C3), INDICON 2015*, vol. 3, pp. 6–9, 2016, doi: 10.1109/INDICON.2015.7443290.

[35] G. Varshney, P. Mittal, V. S. Pandey, R. S. Yaduvanshi, and S. Pundir, “Enhanced bandwidth high gain micro-strip patch feed dielectric resonator antenna,” *Proceeding - IEEE Int. Conf. Comput. Commun. Autom. ICCCA 2016*, no. c, pp. 1479–1483, 2017, doi: 10.1109/CCAA.2016.7813955.

[36] S. Fakhte, H. Oraizi, and M. H. Vadjed Samiei, “A high gain dielectric resonator loaded patch antenna,” *Prog. Electromagn. Res. C*, vol. 30, no. May, pp. 147–158, 2012, doi: 10.2528/PIERC12050813.

[37] S. Fakhte, H. Oraizi, and L. Matekovits, “High gain rectangular dielectric resonator antenna using uniaxial material at fundamental mode,” *IEEE Trans. Antennas Propag.*, vol. 65, no. 1, pp. 342–347, 2017, doi: 10.1109/TAP.2016.2627520.

[38] S. Fakhte, H. Oraizi, L. Matekovits, and G. Dassano, “Cylindrical anisotropic dielectric resonator antenna with improved gain,” *IEEE Trans. Antennas Propag.*, vol. 65, no. 3, pp. 1404–1409, 2017, doi: 10.1109/TAP.2016.2647689.

[39] W. J. Sarjeant and E. Brannen, “On Eigenmodes and Forced Resonance-Modes of Dielectric Sphere,” *Proc. IEEE*, vol. 56, no. 3, pp. 307–308, 1968.

[40] J. Van Bladel, “The Excitation of Dielectric Resonators of Very High Permittivity,” *IEEE Trans. Microw. Theory Tech.*, vol. MTT23, no. 2, pp. 208–217, 1975.

[41] S. A. Long, M. W. McAllister, and L. C. Shen, “The Resonant Cylindrical Dielectric Cavity Antenna,” *IEEE Trans. Antennas Propag.*, vol. 31, no. 3, pp. 406–412, 1983, doi: 10.1109/TAP.1983.1143080.

[42] M. W. McAllister, Long, S.A., “Resonant Hemispherical Dielectric,” *Electron. Lett.*, pp. 657–659, 1979.

[43] A. A. Kishk, H. A. Auda, and B. C. Ahn, “Radiation Characteristics of Cylindrical Dielectric Resonator Antennas.,” *Conf. Proc. - IEEE SOUTHEASTCON*, no. February, pp. 556–560, 1988, doi: 10.1109/secon.1988.194919.

[44] R. K. Mongia, “Half-Split Dielectric Resonator Placed on Metallic Plane for Antenna Applications,” *Electron. Lett.*, vol. 25, no. 7, pp. 462–464, 1989, doi: 10.1049/el:19890318.

[45] R. K. Mongia, Y. M. M. Antar, and M. Cuhaci, “A Half-Split Cylindrical Dielectric Resonator Antenna Using Slot-Coupling,” *IEEE Microw. Guid. Wave Lett.*, vol. 3, no. 2, pp. 38–39, 1993, doi: 10.1109/75.196034.

[46] Y. Kobayashi and S. Tanaka, “Resonant Modes of a Dielectric Rod Resonator Short-Circuited at Both Ends by Parallel Conducting Plates,” *IEEE Trans. Microw. Theory Tech.*, vol. 28, no. 10, pp. 1077–1085, 1980, doi: 10.1109/TMTT.1980.1130228.

[47] M. Tsuji, H. Shigesawa, and K. Takiyama, “Analytical and Experimental Investigations on Several Resonant Modes in Open Dielectric Resonators,” *IEEE Trans. Microw. Theory Tech.*, vol. 32, no. 6, pp. 628–633, 1984, doi: 10.1109/TMTT.1984.1132739.

[48] E. Snitzer, “Cylindrical Dielectric Waveguide Modes*,” *J. Opt. Soc. Am.*, vol. 51, no. 5, p. 491, 1961, doi: 10.1364/josa.51.000491.

[49] M. Lapierre, Y. M. M. Antar, A. Ittipiboon, and A. Petosa, “Ultra Wideband Monopole/Dielectric Resonator Antenna,” *IEEE Microw. Wirel. COMPONENTS Lett.*, vol. 15, no. 1, pp. 7–11, 2005, doi: 10.1109/LMWC.2004.840952.

[50] Y.-F. Ruan, Y.-X. Guo, and X.-Q. Shi, “DOUBLE ANNULAR-RING DIELECTRIC RESONATOR ANTENNA FOR ULTRAWIDEBAND APPLICATION,” *Microw. Opt. Technol. Lett.*, vol. 49, no. 02, pp. 362–366, 2006, doi: 10.1002/mop.

[51] S. Ghosh and A. Chakrabarty, “Ultrawideband performance of dielectric loaded T-shaped monopole transmit and receive antenna/EMI sensor,” *IEEE Antennas Wirel. Propag. Lett.*, vol. 7, pp. 358–361, 2008, doi: 10.1109/LAWP.2008.921335.

[52] I. Zivkovic, “Dielectric loading for bandwidth enhancement of ultra-wide band wire monopole antenna,” *Prog. Electromagn. Res. C*, vol. 30, no. April, pp. 241–252, 2012, doi: 10.2528/PIERC12041704.

[53] M. Niroo-Jazi and T. A. Denidni, “Experimental investigations of a novel ultrawideband dielectric resonator antenna with rejection band using hybrid techniques,” *IEEE Antennas Wirel. Propag. Lett.*, vol. 11, pp. 492–495, 2012, doi: 10.1109/LAWP.2012.2197590.

[54] D. Guha, B. Gupta, and Y. M. M. Antar, “Hybrid monopole-DRAs using

hemispherical/conical-shaped dielectric ring resonators: Improved ultrawideband designs," *IEEE Trans. Antennas Propag.*, vol. 60, no. 1, pp. 393–398, 2012, doi: 10.1109/TAP.2011.2167948.

[55] M. Abedian, S. K. A. Rahim, and M. Khalily, "Two-segments compact dielectric resonator antenna for UWB application," *IEEE Antennas Wirel. Propag. Lett.*, vol. 11, pp. 1533–1536, 2012, doi: 10.1109/LAWP.2012.2232639.

[56] C. Ozzaim, F. Ustuner, and N. Tarim, "Stacked conical ring dielectric resonator antenna excited by a monopole for improved ultrawide bandwidth," *IEEE Trans. Antennas Propag.*, vol. 61, no. 3, pp. 1435–1438, 2013, doi: 10.1109/TAP.2012.2227442.

[57] S. H. Seyyedhatami and R. A. Sadeghzadeh, "A new simple compact ultra-wideband dielectric resonator antenna with enhanced bandwidth and improved radiation pattern," *Int. J. Microw. Wirel. Technol.*, vol. 8, no. 2, pp. 335–340, 2016, doi: 10.1017/S1759078715000021.

[58] A. A. Al-Azza, N. A. Malalla, F. J. Harackiewicz, and K. Han, "Stacked conical-cylindrical hybrid dielectric resonator antenna for improved ultrawide bandwidth," *Prog. Electromagn. Res. Lett.*, vol. 79, no. September, pp. 79–86, 2018, doi: 10.2528/pierl18081008.

[59] Z. Song *et al.*, "Equilateral Triangular Dielectric Resonator and Metal Patch Hybrid Antenna for UWB Application," *IEEE Access*, vol. 7, pp. 119060–119068, 2019, doi: 10.1109/ACCESS.2019.2936013.

[60] T. A. Denidni and Z. Weng, "Rectangular dielectric resonator antenna for ultrawideband applications," *Electron. Lett.*, vol. 45, no. 24, pp. 1210–1212, 2009, doi: 10.1049/el.2009.2210.

[61] T. A. Denidni, Z. Weng, and M. Niroo-Jazi, "Z-Shaped Dielectric Resonator Antenna for Ultrawideband Applications," *IEEE Trans. Antennas Propag.*, vol. 58, no. 12, pp. 4059–4062, 2010, doi: 10.1109/TAP.2010.2078443.

[62] Y. Wang, N. Wang, T. A. Denidni, Q. Zeng, and G. Wei, "Integrated ultrawideband/narrowband rectangular dielectric resonator antenna for cognitive radio," *IEEE Antennas Wirel. Propag. Lett.*, vol. 13, pp. 694–697, 2014, doi: 10.1109/LAWP.2014.2314480.

[63] M. Aoutoul, O. El-Mrabet, M. Essaaidi, and A. El Moussaoui, “A Compact Rectangular Dielectric Resonator Antenna for UWB Wireless Communication Systems,” *Microw. Opt. Technol. Lett.*, vol. 51, no. 10, pp. 2281–2286, 2009.

[64] Z. Weng, X. Wang, Y. Jiao, and F. Zhang, “CPW-fed dielectric resonator antenna for ultra-wideband applications,” *Microw. Opt. Technol. Lett.*, vol. 52, no. 12, pp. 2709–2712, 2010, doi: https://doi.org/10.1002/mop.25567.

[65] T. A. Denidni and Z. Weng, “Hybrid ultrawideband dielectric resonator antenna and band-notched designs,” *IET Microwaves, Antennas Propag.*, vol. 5, no. 4, pp. 450–458, 2011, doi: 10.1049/iet-map.2009.0425.

[66] Y.-F. Wang, S. Liu, T. A. Denidni, Q.-S. Zeng, and G. Wei, “Integrated Ultra-wideband Plannar Monopole with Cylindrical Dielectric Resonator Antennas,” *Prog. Electromagn. Res.*, vol. 44, no. July, pp. 41–53, 2013, doi: 10.2528/PIERC13070902.

[67] I. Messaoudene, T. A. Denidni, and A. Benghalia, “Low-profile U-shaped DRA for ultra-wideband applications,” *Int. J. Microw. Wirel. Technol.*, vol. 9, no. 3, pp. 621–627, 2016, doi: 10.1017/S1759078716000155.

[68] K. S. Ryu and A. A. Kishk, “Ultrawideband dielectric resonator antenna with broadside patterns mounted on a vertical ground plane Edge,” *IEEE Trans. Antennas Propag.*, vol. 58, no. 4, pp. 1047–1053, 2010, doi: 10.1109/TAP.2010.2041160.

[69] K. S. Ryu and A. A. Kishk, “UWB Dielectric Resonator Antenna Having Consistent Omnidirectional Pattern and Low Cross-Polarization Characteristics,” vol. 59, no. 4, pp. 1403–1408, 2011.

[70] A. Sabouni and A. Kisk, “Single or Multi notch bands applied to Microstrip excited Ultra-Wideband Antennas with Dielectric Resonator Antenna case,” *Microw. Opt. Technol. Lett.*, vol. 55, no. 11, pp. 2562–2568, 2013, doi: https://doi.org/10.1002/mop.27482.

[71] M. Abedian, S. K. A. Rahim, S. Danesh, M. Khalily, and S. M. Noghabaei, “Ultrawideband dielectric resonator antenna with WLAN band rejection at 5.8 GHz,” *IEEE Antennas Wirel. Propag. Lett.*, vol. 12, pp. 1523–1526, 2013, doi: 10.1109/LAWP.2013.2291271.

[72] Y. F. Wang, T. A. Denidni, Q. S. Zeng, and G. Wei, “Band-notched UWB rectangular dielectric resonator antenna,” *Electron. Lett.*, vol. 50, no. 7, pp. 483–484, 2014, doi:

10.1049/el.2014.0188.

[73] M. Abedian, S. K. A. Rahim, S. Danesh, S. Hakimi, L. Y. Cheong, and M. H. Jamaluddin, “Novel design of compact UWB dielectric resonator antenna with dual-band-rejection characteristics for WiMAX/WLAN bands,” *IEEE Antennas Wirel. Propag. Lett.*, vol. 14, pp. 245–248, 2015, doi: 10.1109/LAWP.2014.2360828.

[74] U. A. Dash and S. Sahu, “UWB Dual-Band Notched Conical Dielectric Resonator Antenna with Improved Gain,” *IETE J. Res.*, vol. 66, no. 5, pp. 643–653, 2018, doi: 10.1080/03772063.2018.1515672.

[75] Y. Ge, K. P. Esselle, and T. S. Bird, “Compact dielectric resonator antennas with ultrawide 60%-110% bandwidth,” *IEEE Trans. Antennas Propag.*, vol. 59, no. 9, pp. 3445–3448, 2011, doi: 10.1109/TAP.2011.2161538.

[76] E. Erfani, M. Niroo-Jazi, S. Tatu, and T. Denidni, “A hybrid dielectric resonator antenna for spectrum sensing and ultra-wideband applications,” *Microw. Opt. Technol. Lett.*, vol. 58, no. 11, pp. 2609–2611, 2016, doi: https://doi.org/10.1002/mop.30108.

[77] P. Kshirsagar, S. Gupta, and B. Mukherjee, “A two-segment rectangular dielectric resonator antenna for ultra-wideband application,” *Electromagnetics*, vol. 38, no. 1, pp. 20–33, 2017, doi: 10.1080/02726343.2017.1406682.

[78] D. Guha, D. Ganguly, S. George, C. Kumar, M. Sebastian, and Y. M. M. Antar, “A New Design Approach for a Hybrid Monopole to Achieve Increased Ultrawide Bandwidth [Antenna Designer’s Notebook],” *IEEE Antennas Propag. Mag.*, vol. 59, no. 1, pp. 139–144, 2017, doi: 10.1109/MAP.2016.2629180.

[79] M. S. Iqbal and K. P. Esselle, “Pulse-preserving characteristics and effective isotropically radiated power spectra of a new ultrawideband dielectric resonator antenna,” *IET Microwaves, Antennas Propag.*, vol. 12, no. 7, pp. 1231–1238, 2018, doi: 10.1049/iet-map.2017.0172.

[80] K. Trivedi and D. Pujara, “Design and development of ultrawideband-stacked triangular prism-shaped dielectric resonator antenna,” *Microw. Opt. Technol. Lett.*, vol. 61, no. 5, pp. 1193–1199, 2018, doi: 10.1002/mop.31738.

[81] A. Sharma, G. Das, and R. K. Gangwar, “Composite Antenna for Ultrawide Bandwidth Applications,” *IEEE Antennas Propag. Mag.*, vol. 60, no. june, pp. 57–65, 2018.

[82] C. Zebiri *et al.*, “Antenna for Ultra-Wideband Applications with Non-Uniform Defected Ground Plane and Offset Aperture-Coupled Cylindrical Dielectric Resonators,” *IEEE Access*, vol. 7, pp. 166776–166787, 2019, doi: 10.1109/ACCESS.2019.2949527.

[83] F. Wang, C. Zhang, H. Sun, and Y. Xiao, “Ultra-Wideband Dielectric Resonator Antenna Design Based on Multilayer Form,” *Int. J. Antennas Propag.*, vol. 2019, 2019, doi: 10.1155/2019/4391474.

[84] M. Abioghli, A. Keshtkar, M. Naser-Moghadasi, and B. Ghalamkari, “UWB Rectangular DRA Integrated with Reconfigurable Narrowband Antenna for Cognitive Radio Applications,” *IETE J. Res.*, vol. 67, no. 1, pp. 139–147, 2018, doi: 10.1080/03772063.2018.1530075.

[85] M. Simeoni, R. Cicchetti, and A. Yarovoy, “Plastic-Based Supershaped Dielectric Resonator Antennas for Wide-Band Applications,” vol. 59, no. 12, pp. 4820–4825, 2011.

[86] D. Sankaranarayanan, D. Venkatakiran, and B. Mukherjee, “A novel compact fractal ring based cylindrical dielectric resonator antenna for ultra wideband application,” *Prog. Electromagn. Res. C*, vol. 67, no. June, pp. 71–83, 2016, doi: 10.2528/PIERC16062007.

[87] D. Sankaranarayanan, D. Venkatakiran, and B. Mukherjee, “Compact bi-cone dielectric resonator antenna for ultra-wideband applications–a novel geometry explored,” *Electromagnetics*, vol. 37, no. 7, pp. 471–481, 2017, doi: 10.1080/02726343.2017.1380257.

[88] H. Yang, X. Xi, Y. Zhao, L. Wang, and X. Shi, “Design of compact ultrawideband slot antenna with improved band-edge selectivity,” *IEEE Antennas Wirel. Propag. Lett.*, vol. 17, no. 6, pp. 946–950, 2018, doi: 10.1109/LAWP.2018.2825453.

[89] D. Sankaranarayanan, D. Venkata Kiran, and B. Mukherjee, “Laterally Placed CDRA with Triangular Notches for Ultra Wideband Applications,” *Frequenz*, vol. 72, no. 1–2, pp. 1–6, 2017, doi: 10.1515/freq-2016-0294.

[90] G. Kaur and A. Kaur, “Monostatic radar-based microwave imaging of breast tumor detection using a compact cubical dielectric resonator antenna,” *Microw. Opt. Technol. Lett.*, vol. 63, no. 1, pp. 196–204, 2021, doi: 10.1002/mop.32557.

[91] P. Sharma, A. Vaish, and R. S. Yaduvanshi, “The design of a turtle-shaped dielectric resonator antenna for ultrawide-band applications,” *J. Comput. Electron.*, vol. 18, no. 4,

pp. 1333–1341, 2019, doi: 10.1007/s10825-019-01374-8.

[92] A. Zitouni and N. Boukli-Hacene, “T-shaped compact dielectric resonator antenna for UWB application,” *Adv. Electromagn.*, vol. 8, no. 3, pp. 57–63, 2019, doi: 10.7716/aem.v8i3.1077.

[93] F. Abushakra, A. Al-Zoubi, I. Uluer, and D. Hawatmeh, “Ultra-wideband E-shaped dielectric resonator antenna fed by coaxial probe and trapezoidal conductor,” *Int. J. Electron. Lett.*, vol. 9, no. 2, pp. 246–255, 2021, doi: 10.1080/21681724.2020.1726475.

[94] O. M. Haraz and A. R. Sebak, “A Novel Circularly Polarized Dielectric Resonator Antenna for UWB Applications,” in *IEEE Antennas and Propagation Society International Symposium*, 2010, no. 1, pp. 1–4, doi: doi: 10.1109/APS.2010.5562143.

[95] P. Chakraborty, U. Banerjee, A. Saha, and A. Karmakar, “A compact Ultra Wideband dielectric resonator antenna with dual-band circular polarization characteristics,” *Int. J. RF Microw. Comput. Eng.*, vol. 31, no. 4, pp. 1–10, 2021, doi: 10.1002/mmce.22577.

[96] M. Abedian, S. K. A. Rahim, C. Fumeaux, S. Danesh, Y. C. Lo, and M. H. Jamaluddin, “Compact ultrawideband MIMO dielectric resonator antennas with WLAN band rejection,” *IET Microwaves, Antennas Propag.*, vol. 11, no. 11, pp. 1524–1529, 2017, doi: 10.1049/iet-map.2016.0299.

[97] M. M. Sani, R. Chowdhury, and R. K. Chaudhary, “An Ultra-Wideband Rectangular Dielectric Resonator Antenna with MIMO Configuration,” *IEEE Access*, vol. 8, pp. 139658–139669, 2020, doi: 10.1109/ACCESS.2020.3012793.

[98] S. Sharma, C. C. Tripathi, and R. Rishi, “Impedance matching techniques for microstrip patch antenna,” *Indian J. Sci. Technol.*, vol. 10, no. 28, pp. 1–16, 2017, doi: 10.17485/ijst/2017/v10i28/97642.

[99] S. Mohanty and B. Mohapatra, “Microstrip Inset Fed Rectangular Dielectric Resonator Antenna for Near Field Communication,” *Turkish J. Comput. Math. Educ.*, vol. 12, no. 6, pp. 3809–3818, 2021.

[100] V. Sheeba, P. Abdulla, B. A. Mary, P. M. Jasmine, and K. K. Ansha, “Dual-Band Waveguide Fed Hollow Cylindrical Dielectric Resonator Antenna,” *Prog. Electromagn. Res. C*, vol. 117, pp. 145–157, 2021, doi: 10.2528/PIERC21103005.

[101] A. K. Roy and S. Basu, “Broadband, high gain, narrow width rectangular dielectric

resonator antenna with air gap," *J. Electron. Sci. Technol.*, vol. 17, no. 1, pp. 90–96, 2019, doi: https://doi.org/10.11989/JEST.1674-862X.70728079.

[102] M. K. Khandelwal, B. K. Kanaujia, and S. Kumar, "Defected ground structure: fundamentals, analysis, and applications in modern wireless trends," *Int. J. Antennas Propag.*, vol. 2017, 2017, doi: https://doi.org/10.1155/2017/2018527.

[103] P. M. Mpele, F. M. Mbango, D. B. O. Konditi, and F. Ndagijimana, "A tri-band and miniaturized planar antenna based on countersink and defected ground structure techniques," *Int. J. RF Microw. Comput. Eng.*, vol. 31, no. 5, p. e22617, 2021, doi: 10.1002/mmce.22617.

[104] I. Nadeem, M. Alibakhshikenari, F. Babaeian, A. A. Althuwayb, B. S. Virdee, L. Azpilicueta, S. Khan, I. Huynen, F. Falcone, and T. A. Denidni, "A comprehensive survey on" Circular Polarized Antennas" for existing and emerging wireless communication technologies," *J. Phys. D. Appl. Phys.*, 2021, doi: https://doi.org/10.1088/1361-6463/ac2c36.

[105] U. Ullah, M. F. Ain, and Z. A. Ahmad, "A review of wideband circularly polarized dielectric resonator antennas," *China Commun.*, vol. 14, no. 6, pp. 65–79, 2017, doi: 10.1109/CC.2017.7961364.

[106] K. M. Prasanna and S. K. Behera, "A hexagonal MIMO antenna system with defected ground structure to enhance bandwidth and isolation," 2013.

[107] P. R. Prajapati, A. Patnaik, and M. V. Kartikeyan, "Improved DGS parameter extraction method for the polarization purity of circularly polarized microstrip antenna," *Int. J. RF Microw. Comput. Eng.*, vol. 26, no. 9, pp. 773–783, 2016, doi: 10.1002/mmce.21029.

[108] K. M. Luk, "Dielectric resonator antennas," *Res. Stud. Pr.*, 2003.

[109] R. S. Yaduvanshi and H. Parthasarathy, "Rectangular dielectric resonator antennas," *doi*, vol. 10, pp. 978–981, 2016.

[110] M. Chauhan, A. K. Pandey, and B. Mukherjee, "A novel cylindrical dielectric resonator antenna based on Fibonacci series approach," *Microw. Opt. Technol. Lett.*, no. February, pp. 1–7, 2019, doi: 10.1002/mop.31887.

[111] B. Mukherjee, P. Patel, and J. Mukherjee, "A review of the recent advances in dielectric resonator antennas," *J. Electromagn. Waves Appl.*, vol. 34, no. 9, pp. 1095–1158, 2020.

[112] G. VARSHNEY, "Gain and Bandwidth Enhancement of a Singly Fed Circularly Polarized Dielectric Resonator Antenna," *IET Microwaves, Antennas Propag.*, 2020, doi: 10.1049/iet-map.2019.0932.

[113] T.-W. Kim and S.-O. Park, "Analysis of Stacked Dielectric Resonator Antenna," in *2018 International Symposium on Antennas and Propagation (ISAP)*, 2018, pp. 1–2.

[114] S. Gotra, G. Varshney, R. S. Yaduvanshi, and V. S. Pandey, "Dual-band circular polarisation generation technique with the miniaturisation of a rectangular dielectric resonator antenna," *IET Microwaves, Antennas Propag.*, vol. 13, no. 10, pp. 1742–1748, 2019, doi: 10.1049/iet-map.2019.0030.

[115] R. Kumar, G. Varshney, R. S. Yaduvanshi, D. Kumar, and V. S. Pandey, "Dual-Band Dielectric Resonator Antenna with Multi- Frequency Circular Polarization," *IET Microwaves, Antennas Propag.*, vol. 14, no. 5, pp. 435–439, 2020, doi: https://doi.org/10.1049/iet-map.2019.0480.

[116] Y. Torabi, A. Bahri, and A. R. Sharifi, "A Novel Metamaterial MIMO Antenna with Improved Isolation and Compact Size Based on LSRR Resonator," *IETE J. Res.*, vol. 62, no. 1, pp. 106–112, 2016, doi: 10.1080/03772063.2015.1085335.

[117] G. Das, A. Sharma, and R. K. Gangwar, "Dielectric resonator-based two-element MIMO antenna system with dual band characteristics," *IET Microwaves, Antennas Propag.*, vol. 12, no. 5, 2018, doi: 10.1049/iet-map.2017.0744.

[118] T.-W. Kim, R. S. Aziz, and S.-O. Park, "Design of patch loaded with metallic posts inside dielectric resonator antenna," *IET Microwaves, Antennas Propag.*, vol. 11, no. 10, pp. 1483–1487, 2017.

[119] M. Mrnka and Z. Raida, "Enhanced-Gain Dielectric Resonator Antenna Based on the Combination of Higher-Order Modes," *IEEE Antennas Wirel. Propag. Lett.*, vol. 15, 2016, doi: 10.1109/LAWP.2015.2470099.

[120] A. Sharma, P. Ranjan, and R. K. Gangwar, "Multiband cylindrical dielectric resonator antenna for WLAN/WiMAX application," *Electron. Lett.*, vol. 53, no. 3, 2017, doi: 10.1049/el.2016.3548.

[121] F. Wang, Z. Duan, S. Li, Z. Wang, and Y. Gong, "Compact UWB MIMO antenna with metamaterial-inspired isolator," *Prog. Electromagn. Res. C*, vol. 84, no. March, pp. 61–

74, 2018.

[122] A. Sharma and R. K. Gangwar, “Triple-band dual-polarized hybrid cylindrical dielectric resonator antenna with hybrid modes excitation,” *Prog. Electromagn. Res. C*, vol. 67, no. June, pp. 97–105, 2016, doi: 10.2528/pierc16060904.

[123] R. K. Gangwar, A. Sharma, M. Gupta, and S. Chaudhary, “Hybrid cylindrical dielectric resonator antenna with HE11δ and HE12δ mode excitation for wireless applications,” *Int. J. RF Microw. Comput. Eng.*, vol. 26, no. 9, pp. 812–818, 2016, doi: 10.1002/mmce.21033.

[124] Y. Wang, P. Landreman, D. Schoen, K. Okabe, Ann Marshall, U. Celano, H.S. Philip Wong, J. Park, and M.L. Brongersma, “Electrical tuning of phase-change antennas and metasurfaces,” *Nat. Nanotechnol.*, vol. 16, no. 6, pp. 667–672, 2021.

[125] I. Ali, M. H. Jamaluddin, A. Gaya, H. A. Rahim, "A dielectric resonator antenna with enhanced gain and bandwidth for 5G applications," *sensors*, vol. 20, no. 3, pp. 1-12, 2020.